POLITECNICO DI MILANO

Scuola di Ingegneria Industriale e dell'Informazione

Corso di Laurea Magistrale in Ingegneria Biomedica

Image-based analysis of tricuspid valve biomechanics: towards a novel approach integrating in vitro 3D-echocardiography and finite element modelling

Relatore: Prof. Emiliano VOTTA
Correlatori: Dott. Omar Antonio PAPPALARDO
               Dott. Matteo SELMI

Tesi di Laurea Magistrale di:
Angela AVERSA   Matr. 837171
Eleonora CAREDDU   Matr. 841988

Anno Accademico 2016/2017

Contents

Abstract

Introduction

In the last decade the tricuspid valve (TV) has acquired a growing importance, as revealed by the number of new clinical techniques developed for the treatment of TV pathologies. In this context, finite element models would be a reliable and effective tool to aid surgical planning and to test new devices, allowing for the evaluation of potential stress-or-strain-mediated remodelling and inflammation induced by the procedure. Nevertheless, patient specific computational models of the TV have not been designed yet, due to the lack of information on anatomical features and tissue mechanical properties of the valve.

In this thesis, we developed a novel approach integrating in vitro imaging and finite element modelling, to analyse the biomechanics of the TV. The input data needed to develop the computational model were derived from the experimental campaigns performed on a mock circulation loop. In particular, a customized protocol was defined to acquire images of the TV from which the geometrical reconstruction of the valve was performed. The computational model of the TV was developed with the aim to provide a reliable geometrical framework and a realistic characterization of the biomechanical response of the valve, based on a novel description of the material properties of the TV leaflets.

Materials and methods

The workflow and the tools used in this project can be divided in the following phases:

- acquisition of echocardiographic images of the TV from the mock circulation loop (MCL), developed by the ForCardioLab (Luigi Sacco Hospital, Milan, Italy);

- experimental campaign performed to collect morphometric parameters and provide an anatomical framework of the geometrical modelling of the TV;

- reconstruction and discretization of the TV 3D geometry derived from the images, using custom software developed in MATLAB (The MathWorks Inc, Natick, MA, United States);

- modelling of leaflets mechanical properties;

- development of a computational model for finite elements analyses, performed through ABAQUS/Explicit 6.10 (Simulia, Providence, Rhode Island, USA).

Data acquisitions from the MCL were performed using real-time 3-dimensional echocardiography (RT3DE) (iE33, Philips) and a TEE probe (CX7-2t). The MCL was previously designed at Department of Electronics, Information and Bioengineering (DEIB) of Politecnico di Milano [34] to simulate physiological and pathological hemodynamic conditions of the cardiopulmonary circulation. The central element was represented by a right swine heart, actuated by a pulsatile pumping system through a cylindrical connector placed on the trans-septal wall. The pulmonary artery was connected to the pulmonary impedance simulator, while the right atrium was connected to the pre-load reservoir.

A protocol for the echocardiographic acquisitions from the MCL was defined, acting both on probe positioning and on echo machine settings. Concerning the first aspect, the acquisitions were performed testing two configurations: i) with the probe at a fixed distance from the heart (Figure 1(a)); ii) with the probe in contact with the epicardium (Figure 1(b)).

(a) (b)
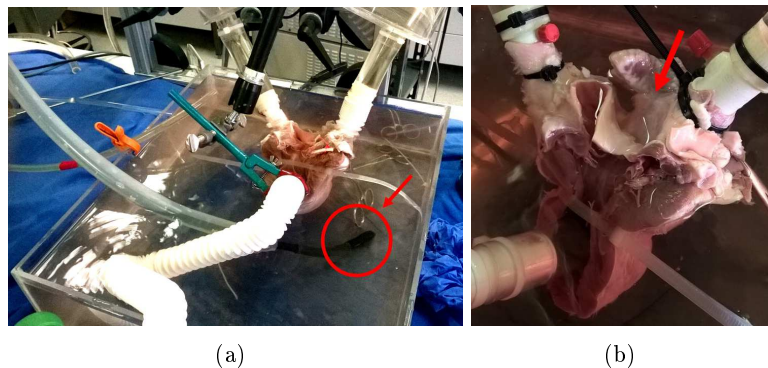
Figure 1: Two experimental configurations tested: (a) probe at a fixed distance from the heart; (b) probe in contact with the epicardium between the pre/after-load connectors.

In most cases, the images acquired with the first modality were characterised by artifacts and shadowing effects due to the presence of the pulmonary and atrial connectors, resulting in a hard and sometimes erroneous identification of the TV annulus and leaflets from the images. For this reason, the best positioning was found placing the probe directly on the epicardium between the two connectors.

Regarding the echo machine settings, the key aspect consisted in identifying the trade-off between temporal and spatial resolution. To improve temporal resolution, the images were acquired with a four-beats 3D method, owing to the fact that, with a stable heart position, no

stitch artifacts are visible when the subvolumes are merged. Altogether, these improvements allows to obtain good quality images to observe both the entire tricuspid valve and the right ventricle. An echocardiographic acquisition campaign was run on four porcine hearts.

Experimental measurements were performed on the four tested hearts to quantitatively describe the morphological features of the tricuspid valve. The valves were excised and the following quantities were estimated: i) annular perimeter; ii) leaflet length; iii) leaflet height, measured from the annulus to the free margin (FM), both at the midpoint of each leaflet and at the commissural position; iv) leaflet thickness. All the measured variables, except for the leaflets thickness, were evaluated also on the 3DE-based TV, to assess the possible effects of the approximations introduced by the reconstruction procedure.

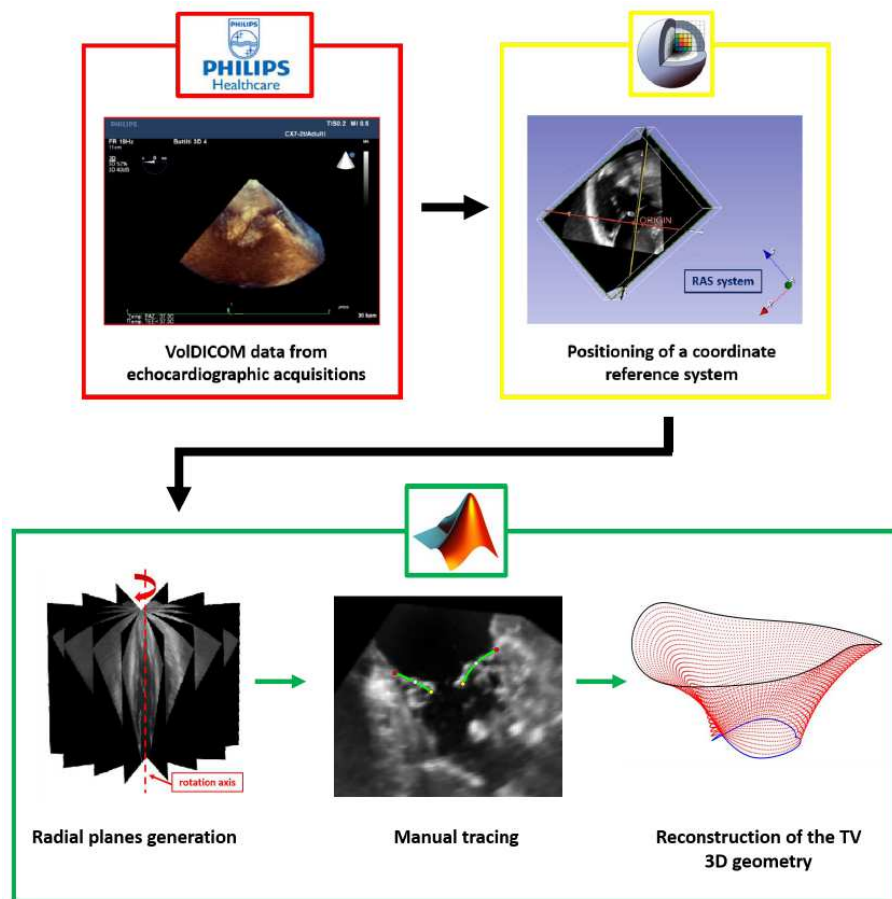The modelling approach defined to process the images can be summarized as depicted in Figure 2.

Figure 2: Workflow of the image processing: the acquired VolDICOM datum was investigated and a coordinate reference system was positioned; 18 radial planes were generated and the TV structures were manually traced, so to automatically perform the 3D reconstruction of the valve.

In order to define the reference frame, the VolDICOM datum was investigated with 3D SLICER 4.6 (Brigham and Women's Hospital, Harvard University, NIH), a free open-source software application for medical image computing, which can be used to explore the volume slice-by-slice. An intrinsic right-hand coordinate system (RAS) was positioned and the three main planes (i.e., two long-axis and one short-axis planes) were displayed. 3D SLICER allowed for the roto-translation of these planes so to position the origin in the TV centre, parallel to the annular plane (Figure 3). This operation was performed at the end-diastole (ED) frame, chosen as the last frame before the TV starts closing, and provided the RAS coordinates of the origin and the normal directions of each plane.
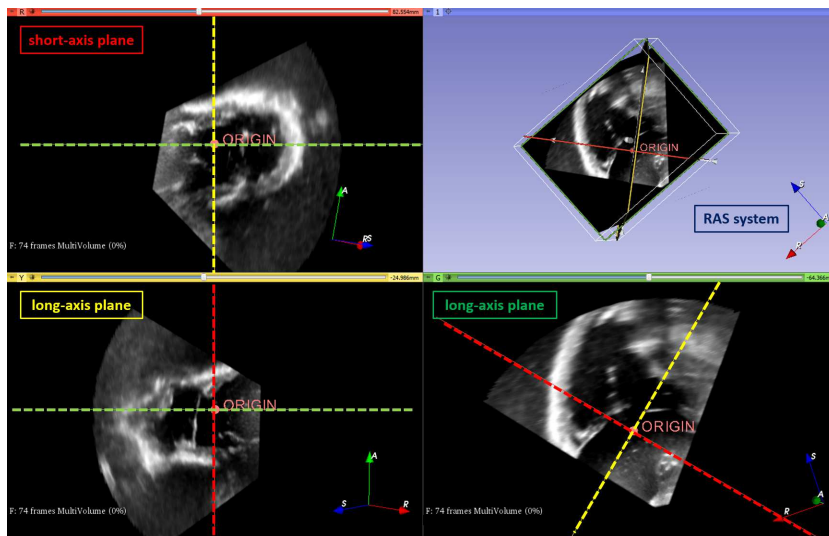
Figure 3: VolDICOM investigation with 3D SLICER: exploring the volume slice-by-slice, a coordinate system origin was positioned in the TV centre. The dashed cross-hairs represent the two planes orthogonal to each view.

The outputs were processed by means of dedicated software, developed in MATLAB, and 18 radial planes were generated by rotating a long-axis plane by 10 degrees relative to the axis passing through the origin previously defined. On each radial plane two points were manually traced both for the annulus and FM; for each leaflet, traced points were automatically interpolated with cubic splines, which were sampled in 63 uniformly distributed points, running from the annulus to FM. A cylindrical reference system was set with the origin in the centre of mass of the points on TV annulus, and the z-axis normal to the least-square plane of the annular points. In this local reference frame, the radial and axial positions of the ith point of every leaflet spline were then approximated through 4th order Fourier functions of the angular position. Every Fourier function was upsampled at n points (in this work 400, with a mean spatial resolution of 0.366 mm), so to reconstruct the TV geometry as a 3D point cloud described by m levels (in this work 63) from the annulus to FM, each with n points uniformly

circumferentially distributed. Sampled points were connected, to discretize leaflets surfaces, into a mapped mesh of 3-node triangular plane-stress shell elements (ABAQUS User's Manual, Chapter 25.6).

To correctly divide the reconstructed valvular profile in three leaflets, namely the septal, anterior and posterior, the position of the three commissures was defined. In particular, we implemented two different strategies to identify them on the annular profile. The first method was based on the assumption that the free edge of the TV was characterized by numerous indentations (clefts), the most prominent ones being located at the three commissures [13]. Hence, the three major indentations were automatically identified on the valve profile evaluating, for each leaflet spline, the length from the annulus to the FM. In this way, three points were positioned on the annulus at the three local minimum lengths (Figure 4).
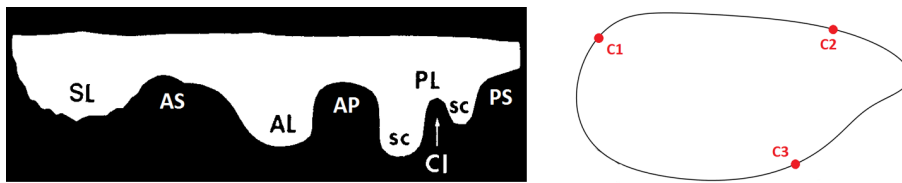
Figure 4: "Analytical" method to find the three commissures. Left: schematic diagram of typical tricuspid valve showing clefts (Cl), commissures (AS, AP, PS), leaflets (SL, AL, PL) and scallops (sc) [13]; right: commissural points along the annulus profile.

The second method was the manual segmentation of the three points on the TV short-axis plane in 3D SLICER. The motion of the TV leaflets during the cardiac cycle was observed to identify the three hinge points of the leaflets on the annulus, corresponding to the commissures. Three markers were then positioned at the systolic peak frame (SP), chosen as the frame in the middle of the systole (Figure 5). The RAS coordinates were exported and processed in MATLAB: the three resulting angular positions were detected on the annular profile.
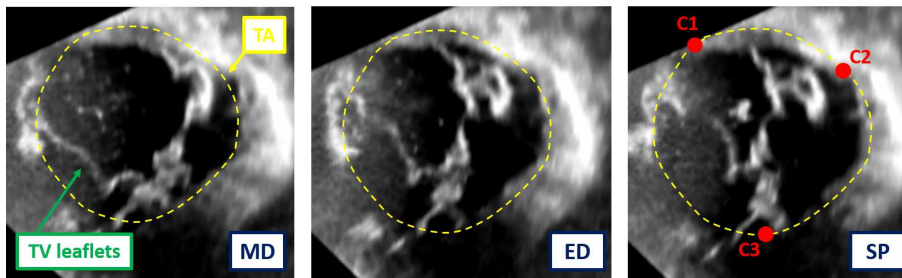
Figure 5: Direct segmentation of the three commissures (C1, C2, C3) on the TV short-axis plane in 3D Slicer. MD: mid-diastole; ED: end-diastole; SP: systolic peak; TA: tricuspid annulus.

Independently from the adopted method, the identification of the commissures provided three points, but their position with respect to the heart is unknown. Therefore, an external anatomical landmark was selected. We chose the inter-ventricular septum as reference area for the following reasons: i) the position of the commissures with respect to the septum is known [14]; ii) the septum was simply detected on the images, due to the presence of the pump connector, inserted in the septal wall.

Concerning the modelling of the sub-valvular apparatus, the detection of the papillary muscles (PMs) and chordae tendinae on the acquired images resulted very difficult. Therefore, the PMs were placed in agreement with the sonomicrometric data reported by Hiro et al [41] on ovine TVs; and chordae tendineae were modelled considering commissural, rough and basal chordae departing from each PM. Since no solid information about chordae tendineae of the TV is available in literature, the corresponding branched structure, the origin from PMs and insertion sites on the leaflets were defined in accordance to *ex vivo* findings provided by Stevanella et al [40] and to the anatomical description presented by Silver et al [12]. In ABAQUS, the PMs were modelled as single nodes, neglecting the presence of multiple heads in the same PM, while the chordae were discretized into truss elements to make their resistance to axial compressive loads negligible.

The closure of the TV was simulated applying a physiologic transvalvular pressure curve, that was measured during the experimental tests on the MCL. Image-based nodal displacements were assigned to the annulus from ED to the SP to replicate the annular motion, while papillary muscles motion was neglected.

The mechanical behaviour of the leaflets was assumed non linear and anisotropic and it was modelled according to the hyperlastic theory through the strain energy function Ψ, proposed by Lee et al. [44]:

$$\Psi = c_0(I_1 - 3) + c_1[(1 - \beta)e^{c_2(I_1-3)^2} + \beta e^{c_3(I_4-3)^2} - 1], \tag{1}$$

where $I_1 = trace(\mathbf{C})$, $I_4 = \mathbf{N} \cdot \mathbf{C} \cdot \mathbf{N}$ are respectively the first and fourth invariants of the Cauchy-Green strain tensor $\mathbf{C}$ and $\mathbf{N}$ is the direction of the fibres in the unloaded configuration, assumed circumferentially oriented, according to the cylindrical reference system previously described. The constitutive parameters of the model are c_0, c_1, c_2, c_3, β and were identified fitting the equibiaxial tensile data acquired by Pham et al. from human TV leaflets [19].

The mechanical response of the chordae tendineae was considered non linear isotropic and was described through a second order polynomial strain energy function available in the ABAQUS

material library. The constitutive parameters were evaluated from the experimental tensile data on human chordae provided by Lim et al [22], supposing lower tension acting on the basal chordae, compared to the rough and commissural ones, as reported in literature [45].

Results

The repeatability of the above described TV modelling procedure was assessed. Two independent observers traced TV substructures on the four echocardiographic data sets and the corresponding 3D geometry was then reconstructed. The interobserver mismatch between the position of the traced points was quantified through a nonparametric Bland-Altman analysis. As regards the variability of the automated reconstruction, the meshes obtained from the tracings of the two operators were compared for each of the four valves and analysed through descriptive statistics and colour maps. These results are depicted for one of the four valves studied (Figure 6). For the same valve, also the comparison between direct and 3DE-based measurements of the TV geometry is reported (Table 1).

Measurements [mm]	Direct	3DE-based
Perimeter	155	154 (-0.6%)
AL length	50	38 (-24.0%)
PL length	47	66 (+40.4%)
SL length	55	49 (-10.9%)
AL height	22	24 (+9.1%)
PL height	17	28 (+64.7%)
SL height	18	20 (+8.8%)
AS-c height	7	27 (+281.4%)
PS-c height	10	23 (+128.4%)
AP-c height	10	27 (+168.7%)

Table 1: Comparison between direct and 3DE-based measurements of the TV geometry. The magnitude of the percentage differences is reported in brackets. Abbreviations: 3DE, three-dimensional echocardiography; AL, anterior leaflet; PL, posterior leaflet; SL, septal leaflet; AS-c, antero-septal commissural; PS-c, postero-septal commissural; AP-c, antero-posterior commissural.

The plots show a different interobserver level of agreement for the manual tracings of the annulus and free-edge. Biases and the amplitudes of the 90% limit of agreement are, respectively, 0.15 mm and 5.86 mm for the annulus, and 2.06 mm and 5.55 mm for the free-edge. The histogram used to analyse the distribution of the mesh mismatch has a single tail, with the largest percentage of occurrences located below 4 mm. The median value of the mismatch is 1.92 mm. The spatial distribution of the distances between the two meshes is displayed in a colour map. As well as for the manual tracing, the highest mismatch is generally at the free margin. Table 1 shows that the 3DE-based measurements of the annular perimeter and leaflets lengths are not notably affected by the approximations introduced with the TV recon-
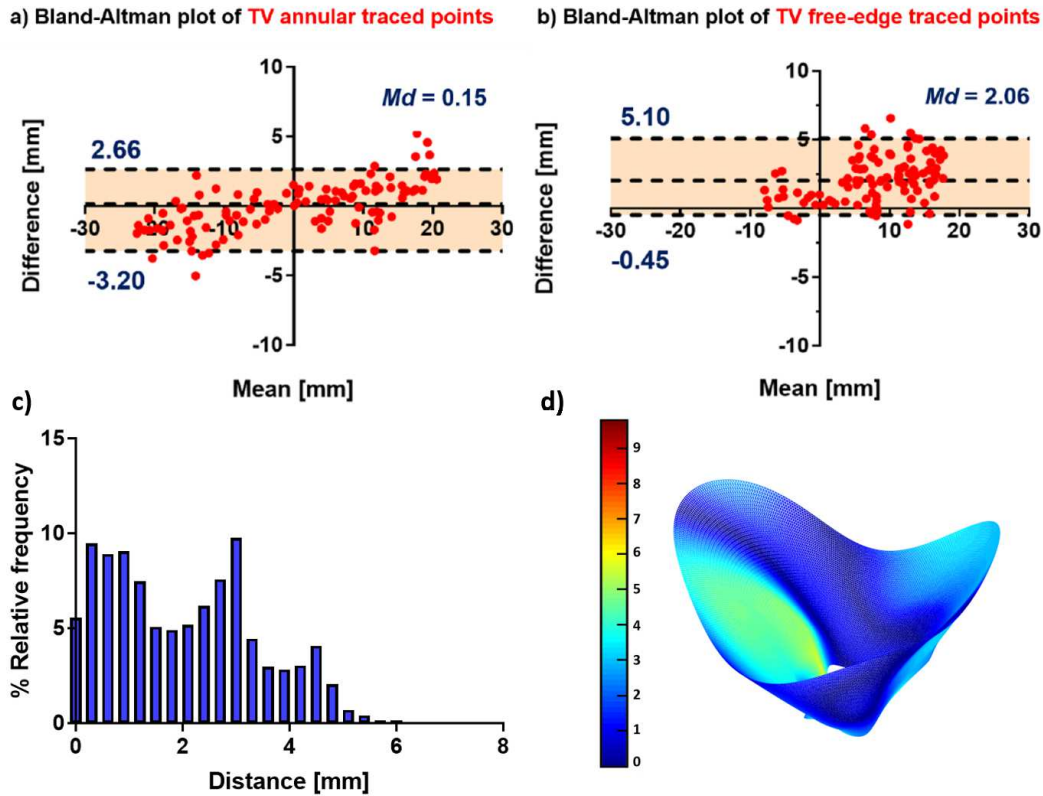
Figure 6: Analysis of the interobserver variability: a-b) Bland-Altman plots comparing the results of manual tracings of TV annulus and free-edge (horizontal dotted lines indicate the limits of agreement; Md = median, is reported as measure of bias); c) histogram of the distribution of the interobserver mesh mismatch (class width=0.3 mm. The occurrences in each class are evaluated as relative frequency percentage); d) colour map showing the spatial distribution of the mesh mismatch (values in the colorbar are reported in mm).

struction process (percentage difference from -0.6% to 40.4%). On the contrary, the leaflets and commissural heights considerably exceed the direct measurements (percentage difference from 8.8% to 281.4%). The overestimation is probably due to the following reasons: i) the VolDICOM datum was sampled in 18 equally spaced radial planes, hence the actual position of the commissures could be between two sampled points; ii) even if the three commissural portions were visible on the radial planes, the reconstructed TV leaflets were derived from approximations with 4th order Fourier functions, that tone down local steep changes in leaflet height. However, all these results are consistent with the fact that free-edge portions of the leaflets are not as clearly visible as the annulus in 3DE images, resulting in a possible erroneous segmentation of this substructure on the image.

The biomechanical behaviour of the four analysed valves was simulated from ED to SP. The results, exemplified for one valve (Figure 7), show a non complete coaptation of the leaflets.

The analyses of leaflets motion throughout transient closure, of the strain distribution over the leaflets and of leaflet stresses suggested that the incomplete coaptation of the leaflets is likely due to an excessive tethering effect exerted by the chordae tendineae, owing to the shape of the leaflets free margin next to chordal insertions. Moreover, because of the relative position of papillary muscles and chordal insertions, in some cases the leaflet is pulled not only donwards and radially outwards, but also circumferentially, thus hampering the effectiveness of leaflet motion in terms of orifice occlusion. An example of this behaviour is depicted, for one of the four valves, in Figure 7.
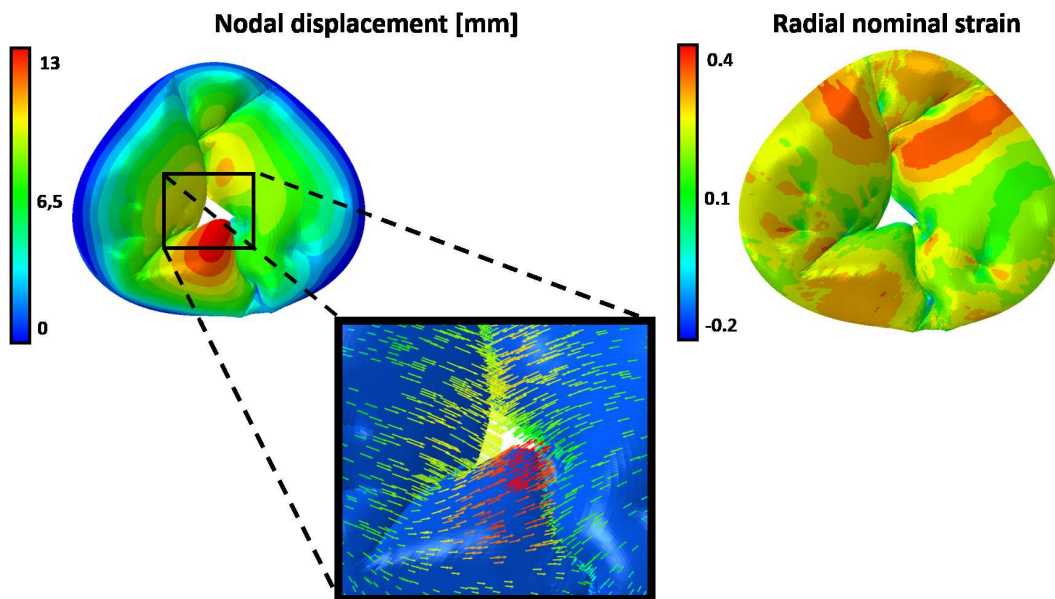
Figure 7: Nodal displacements distribution and directions of the resultant displacemt, indicated with arrows (left); radial nominal strain distribution at SP, showing high values in correspondence of the chordal insertions (right).

Conclusions

In this thesis a novel method was proposed for the study of the TV biomechanics, integrating experimental and computational approaches. The experimental campaign performed on the MCL allowed for the realistic and globally accurate geometrical reconstruction of the valve and provides the input data to define the first imaged-based complete FEM, implementing mechanical properties of the TV. The obtained preliminary model presents some limitations both related to the computational process, namely the segmentation of the leaflets, and to the lack of morphological and mechanical information on the TV. Nevertheless, this work has to be considered a first step towards reliable and accurate modelling of TV biomechanics.

Sommario

Introduzione

Nell'ultimo decennio la valvola tricuspide (VT) ha acquisito un'importanza clinica crescente, come rivelato dal numero di nuove procedure sviluppate per il trattamento di patologie a carico della valvola stessa. In questo contesto, i modelli ad elementi finiti sarebbero uno strumento affidabile ed efficace al fine della pianificazione chirurgica e il testing di nuovi dispositivi, consentendo la valutazione di potenziali sforzi e deformazioni dovuti al rimodellamento indotto dalla procedura. Ciò nonostante, modelli computazionali paziente-specifici della VT non sono stati ancora sviluppati, a causa della mancanza di informazioni riguardanti le caratteristiche anatomiche e le proprietà meccaniche della valvola.

Nel presente progetto di tesi, abbiamo sviluppato un nuovo approccio integrando ecocardiografia in vitro e modellizzazione agli elementi finiti, per analizzare la biomeccanica della VT. I dati in ingresso al modello computazionale sono stati ricavati da una campagna sperimentale effettuata su un simulatore di circolazione sanguigna. In particolare, è stato definito un protocollo di acquisizione delle immagini, dalle quali è stata ricostruita la geometria della valvola. Il modello computazionale è stato implementato con l'obiettivo di fornire una caratterizzazione realistica della geometria e della risposta biomeccanica della VT, basata su una nuova descrizione delle proprietà dei lembi valvolari.

Materiali e metodi

Il flusso di lavoro del presente progetto può essere suddiviso nelle seguenti fasi:

- acquisizione di immagini ecocardiografiche da simulatore della circolazione, sviluppato dal ForCardioLab (Ospedale Luigi Sacco, Milano, Italia);

- campagna sperimentale effettuata per ottenere parametri morfometrici e fornire al modello un data-set di misure anatomiche e parametri morfometrici;

- ricostruzione della geometria 3D della VT a partire da immagini, utilizzando un tool sviluppato in MATLAB (The MathWorks Inc, Natick, MA, USA);

- modellizzazione delle proprietà meccaniche del materiale dei lembi;

- sviluppo di un modello computazionale per analisi ad elementi finiti, effettuata tramite ABAQUS/Explicit 6.10 (Simulia, Providence, Rhode Island, USA).

L'acquisizione delle immagini dal simulatore è stata effettuata utilizzando l'ecocardiografia real-time 3D (RT3DE) (iE33, Philips) con una sonda TE (CX7-2t). Il set-up è stato precedentemente sviluppato al Dipartimento di Elettronica, Informazione e Bioingegneria (DEIB) del Politecnico di Milano [34] per simulare la circolazione polmonare in condizioni fisiologiche e patologiche. L'elemento centrale è costituito dal un cuore destro porcino, attivato da un sistema di pompaggio pulsatile attraverso un connettore cilindrico posto nella parete del setto interventricolare. L'arteria polmonare è connessa al simulatore di impedenza polmonare, mentre l'atrio destro è collegato alla riserva di pre-carico.

E' stato definito un protocollo sperimentale per le acquisizioni di immagini dal simulatore, agendo sia sul posizionamento della sonda che sulle impostazioni dell'ecografo. Riguardo al primo aspetto, le acquisizioni sono stato eseguite testando due diverse configurazioni: i) con la sonda posizionata non in contatto con il cuore (Figure 8(a)); ii) con la sonda in contatto con l'epicardio (Figure 8(b)).

(a)   (b)
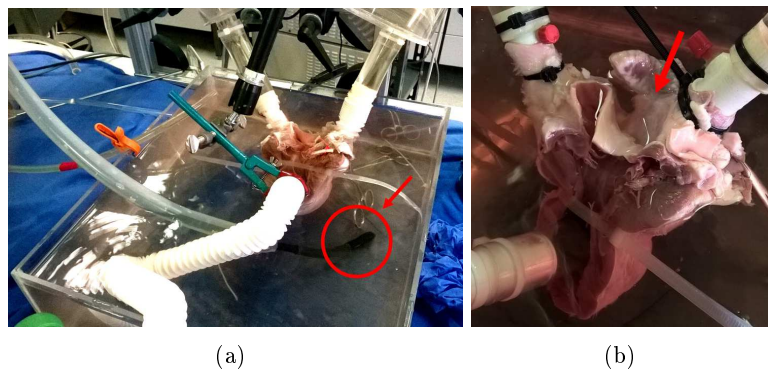
Figure 8: Configurazioni di acquisizione testate: (a) sonda non in contatto con il cuore; (b) sonda in contatto con l'epicardio posizionata fra i connettore di pre- e postcarico.

Nella maggior parte dei casi, le immagini acquisite con la prima modalità erano caratterizzate da artefatti ed effetti ombra dovuti alla presenza dei connettori polmonari e atriali, che comportano una complessa e talvolta erronea identificazione dell'annulus e dei lembi dalle immagini. Per questo motivo la soluzione migliore è stata posizionare la sonda direttamente sull'epicardio tra i due connettori.

Per quanto riguarda le impostazioni dell'ecografo, l'aspetto critico riguarda l'identificazione di un compromesso tra risoluzione temporale e spaziale. Per migliorare la risoluzione tem-

porale, le immagini sono state acquisite con un metodo 3D a quattro battiti, in quanto, con una posizione stabile del cuore, non sono visibili artefatti dovuti alla unione dei sottovolumi. Complessivamente, questi miglioramenti permettono di ottenere immagini di buona qualità che consentono di visualizzare sia l'intera VT che il ventricolo destro. La campagna di acquisizione è stata eseguita su quattro cuori porcini.

Le misure sperimentali sono state eseguite sui quattro cuori testati per descrivere in modo quantitativo morfologia della valvola tricuspide. Le valvole sono state excise e sono state valutate le seguenti quantità: i) perimetro annulare; ii) lunghezza del lembo; iii) altezza del lembo, misurata dall'annullus al margine libero (ML), sia al centro di ciascun lembo che in corrispondenza delle commissure; iv) spessore del lembo. Tutte le variabili misurate, ad eccezione dello spessore, sono state valutate anche sulla valvola ricostruita da imaging per valutare i possibili effetti delle approssimazioni introdotte dalla procedura di ricostruzione.

L'approccio di modellazione definito per elaborare le immagini può essere riassunto come descritto in Figure 9.

Per definire il sistema di riferimento, il volume VolDICOM è stato studiato con 3D SLICER 4.6 (Brigham and Women's Hospital, Harvard University, NIH), un software open source per l'elaborazione delle immagini mediche, che può essere utilizzato per la navigazione del volume. È stato posizionato un sistema di coordinate intrinseco (RAS) e sono stati visualizzati i tre piani principali (cioè due assi longitudinali e uno in asse corto). Con 3D SLICER è stato possibile roto-traslare questi piani, in modo da posizionare il sistema di riferimento con l'origine nel centro della valvola, parallelo al piano annulare (Figure 10). Questa operazione è stata eseguita per il frame di fine diastole (FD), scelto come ultimo frame prima della chiusura valvolare e ha fornito in output le coordinate RAS dell'origine e le direzioni normali di ciascun piano.

Gli output sono stati elaborati mediante un software dedicato sviluppato in MATLAB e 18 piani radiali sono stati generati ruotando un piano in asse lungo di 10 gradi rispetto ad un asse passante per l'origine precedentemente definita. Su ogni piano radiale sono stati tracciati manualmente due punti per l'annulus e e ML; per ciascun lembo, i punti segmentati sono stati automaticamente interpolati con spline cubiche, che sono state campionate in 63 punti distribuiti uniformemente, dall'annulus a ML. Si è considerato un sistema di riferimento cilindrico con l'origine nel centro di massa dei punti annulari e l'asse z normale al piano ai minimi quadrati dei punti dell'annulus. In questo sistema di riferimento locale, le posizioni radiali e assiali del punto *textit i* di ogni spline del lembo sono stati approssimati con una funzione di Fourier del quarto ordine, in funzione della posizione angolare. Ogni funzione di Fourier è stata campionata in *textit n* punti (in questo lavoro 400, con una risoluzione spaziale
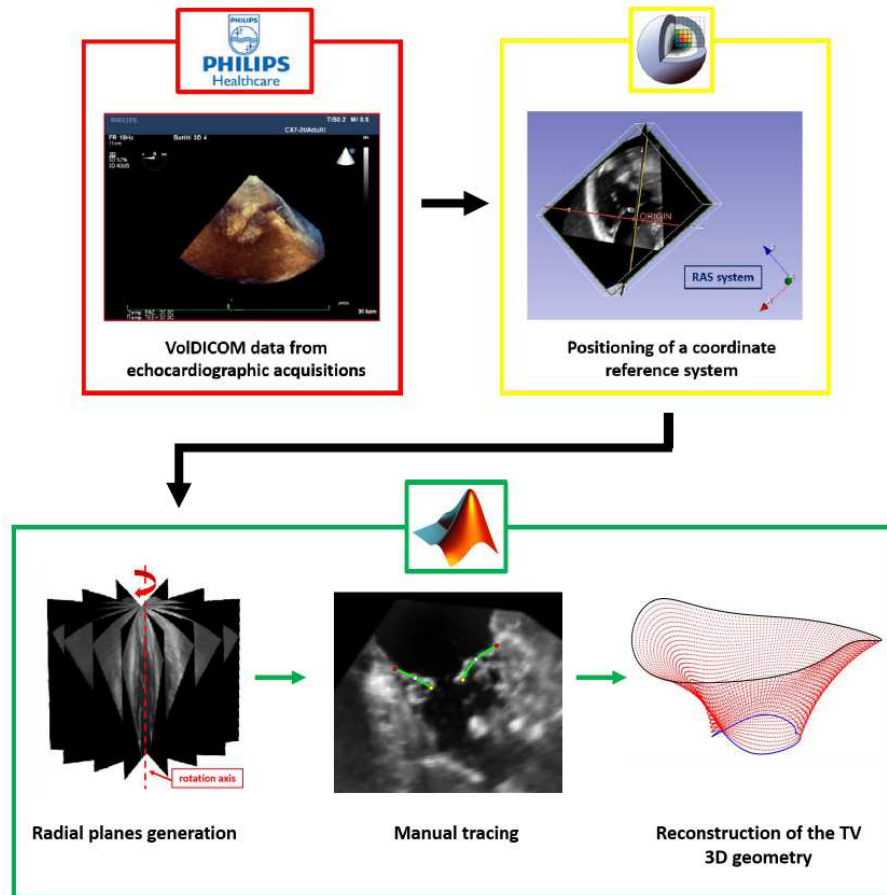
Figure 9: Schema del processo di elaborazione delle immagini: il volume acquisito (VolDICOM) è stato navigato per posizionare il sistema di riferimento; 18 piani radiali sono stati generati, sui quali è avvenuta la segmentazione delle strutture valvolari. Al termine di questa fase, la valvola viene automaticamente ricostruita in 3D.

media di 0,366 mm), per ricostruire la geometria della valvola come una nuvola di punti 3D descritta da *textit m* livelli (in questo lavoro 63) da annulus a ML, ognuno con *textit n* punti distribuiti uniformemente in direzione circonferenziale. Per discretizzare le superficie dei lembi, i punti campionati sono stati connessicon una mesh mappata di elementi triangolari a tre nodi S3R (ABAQUS Manuale d'uso, Capitolo 25.6). Per dividere correttamente il profilo valvolare ricostruito nei tre lembi è stato necessario definire la posizione delle tre commissure. In particolare, abbiamo implementato due diverse strategie per identificarle sul profilo annulare. Il primo metodo si basa sull'ipotesi che il margine libero della valvola presenta una serie di indentazioni, le più prominenti situate in corrispondenza delle tre commissure [13]. Quindi, le tre indentazioni principali sono state identificate automaticamente sul profilo della valvola valutando, per ogni spline del lembo, la lunghezza dall'annulus al ML. In questo modo, tre punti sono stati posizionati sull'annulus alle tre lunghezze minime locali (Figure 11).
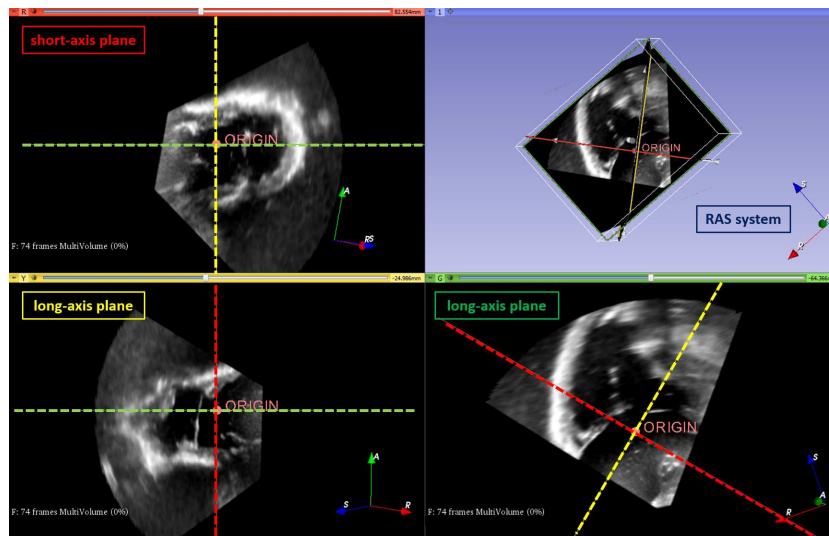
Figure 10: Navigazione del volume VolDICOM con 3D SLICER, al fine di posizionare il sistema di riferimento nel centro della valvola. Le linee tratteggiate rappresentano i due piani perpendicolari ad ogni vista.
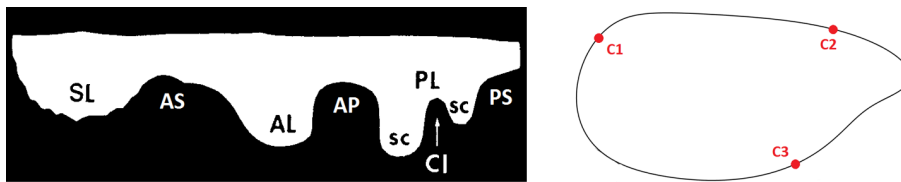

Figure 11: Metodo "analitico" di ricerca delle tre commissure. Sinistra: schema del tipico profilo valvolare, in cui sono visibili le indentazioni (Cl) e le commissure (AS, AP, PS), [13]; destra: punti commissurali posizionati lungo il profilo annulare.

Il secondo metodo consiste nella segmentazione manuale delle tre commissure in 3D SLICER nel piano in asse corto della valvola. Il movimento dei lembi durante il ciclo cardiaco è stato osservato per identificare i tre punti di cerniera dei lembi sull'annulus, corrispondenti alle commissure. Tre markers sono stati poi posizionati nel frame di picco sistolico (PS), scelto come frame a metà della sistole (Figure 12). Le coordinate RAS delle commissure segmentate sono state esportate ed elaborate in MATLAB ed è stata cercata la loro posizione angolare sul progilo ricostruito dell'annulus.

Indipendentemente dal metodo adottato, l'identificazione delle commissure ha fornito tre punti, ma la loro posizione rispetto al cuore non è nota a priori. Pertanto, è stato selezionato un punto di riferimento anatomico esterno. In particolare, abbiamo scelto il setto inter-ventricolare come riferimento per i seguenti motivi: i) la posizione delle commissure rispetto al setto è nota [14]; ii) il setto è facilmente identificabile dalle immagini acquisite per la pre-

Figure 12: Segmentazione diretta delle commissure (C1, C2, C3) in 3D Slicer sul piano in asse corto della valvola. MD: metà diastole; ED: fine diastole; SP: picco sistolico; TA: annulus valvolare.

senza del connettore della pompa, inserito nella parete settale.

Per quanto riguarda la modellizzazione dell'apparato sub-valvolare, l'individuazione dei muscoli papillari (MP) e delle corde tendinee sulle immagini acquisite è risultata molto complessa. Pertanto, i MP sono stati posizionato in accordo con i dati sonomicrometrici riportati da Hiro et al [41] sulle valvole ovine. Le corde tendinee sono state modellizzate in corde commissurali, rough e basali, che originano da ciascuno dei MP. Poiché in letteratura sono presenti scarse informazioni sulle corde tendinne della VT, in questa tesi il pattern delle corde, la corrispondente struttura ramificata e i siti di inserzione sui lembi sono stati definiti in accordo con i risultati textit ex vivo forniti da Stevanella et al [40] e con la descrizione anatomica presentata da Silver [12]. In ABAQUS, i MP sono stati modellizzati come singoli nodi, trascurando la presenza di teste multiple nello stesso PM, mentre le corde sono state discretizzate in elementi truss a due nodi per ottimizzare la loro resistenza ai carichi assiali di compressione.

La chiusura della VT è stata simulata applicando una curva di pressione transvalvolare fisiologica, misurata durante le prove sperimentali sul banco prova. Gli spostamenti nodali ricavati da imaging sono stati assegnati all'annulus da FD a PS per simulare il movimento annulare, mentre il movimento dei muscoli papillari è stato trascurato.

Il comportamento meccanico dei lembi è stato assunto anisotropico non lineare ed è stato modellizzato secondo il comportamento iperlastico attraverso la densità di energia di deformazione Psi, proposta da Lee et al. [44]:

$$\Psi = c_0(I_1 - 3) + c_1[(1 - \beta)e^{c_2(I_1-3)^2} + \beta e^{c_3(I_4-3)^2} - 1], \tag{2}$$

Dove $I_1 = traccia(\ mathbfC)$, $I_4 = \ mathbfN\ cdot\ mathbfC\ cdot\ mathbfN$ sono rispettivamente il primo e il quarto invariante del tensore di deformazione di Cauchy-Green textbf C e textbf N è la direzione delle fibre nella configurazione scarica, assunta circonferenziale,

secondo il sistema di riferimento cilindrico precedentemente descritto. I parametri costitutivi del modello sono c_0, c_1, c_2, c_3, *beta* e sono stati identificati dal fitting dei dati di trazione equibiassiale acquisiti da Pham et al. su campioni umani di lembi [19].

La risposta meccanica delle corde tendinee è stata considerata isotropica non lineare ed è stata descritta con una densità di energia di deformazione di forma polinomiale di secondo ordine, disponibile nella biblioteca del materiale di ABAQUS. I parametri costitutivi sono stati valutati partendo dai dati sperimentali di trazione su corde umane forniti da Lim et al. [22], supponendo che le corde basali siano soggette ad una tensione minore rispetto alle commissurali e alle rough, come riportato in letteratura [45].

Risultati

La ripetibilità della suddetta procedura di modellazione della VT è stata valutata. Due operatori hanno indipendentemente tracciato le strutture valvolari sulle quattro immagini acquisite e la corrispondente geometria 3D è stata ricostruita. La variabilità inter-osservatore tra le posizioni dei punti segmentati è stata quantificata tramite una rappresentazione non parametrica di Bland-Altman. La variabilità della ricostruzione automatica è stata analizzata confrontando le mesh ottenute dai due operatori per ognuna delle quattro valvole, e studiata tramite la statistica descrittiva e le mappe colorimetriche. I risultati sono illustrati per una delle quattro valvole (Figure 13). Per la stessa valvola, è stato riportato il risultato del confronto tra le misure dirette e quelle derivanti da immagini (Table 2).

Misure [mm]	Dirette	Da immagini
Perimetro	155	154 (-0.6%)
Lunghezza LA	50	38 (-24.0%)
Lunghezza LP	47	66 (+40.4%)
Lunghezza LS	55	49 (-10.9%)
Altezza LA	22	24 (+9.1%)
Altezza LP	17	28 (+64.7%)
Altezza LS	18	20 (+8.8%)
Altezza c-AS	7	27 (+281.4%)
Altezza c-PS	10	23 (+128.4%)
Altezza c-AP	10	27 (+168.7%)

Table 2: Confronto tra le misure dirette e ricavate da immagini della geometria della VT. Tra parentesi è riportata l'ampiezza delle differenze percentuali. Abbreviazioni: LA, lembo anteriore; LP, lembo posteiore; LS, lembo settale; c-AS, commissura antero-settale; c-PS, commissura postero-settale; c-AP, commissura antero-posteriore.

I grafici mostrano una diversa variabilità interosservatore per i tracciamenti di annulus e ML. Le mediane e le ampiezze dell'intervallo di confidenza non parametrico sono, rispettivamente, 0.15 mm e 5.86 mm per l'annulus, 2.06 mm e 5.55 mm per il ML. L'istogramma, utilizzato per
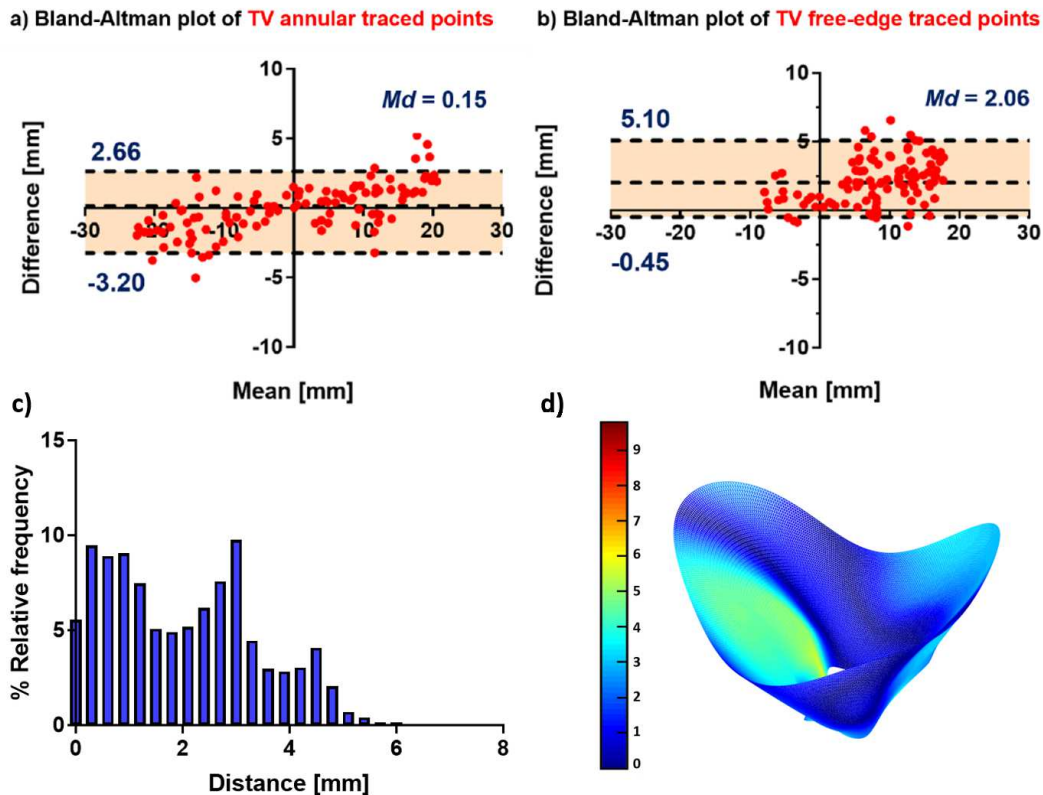
Figure 13: Analisi della variabilità inter-osservatore: a-b) Rappresentazione di Bland-Altman del confronto tra le segmentazioni di annulus e ML (le linee orizzontali indicano l'intervallo di confidenza non parametrico; Md = mediana, è riportata come misura della differenza media); c) istogramma della distribuzione delle distanze inter-osseravatore tra le mesh (ampiezza della classe=0.3mm. La densità di frequenza è riportata come percentuale); d) mappa colorimetrica della distribuzione spaziale delle distanze tra le mesh dei due operatori (i valori sono riportati in mm).

rappresentare la distribuzione delle distanze tra le due mesh, ha una sola coda, con la maggiore densità di frequenza sotto i 4 mm. Il valor medio delle distanze è 1.92 mm. La distribuzione spaziale delle distanze è mostrata nella mappa colorimetrica: i valori più elevati si hanno in corrispondenza del ML della valvola. Dalla Table 2 emerge che le misure di perimetro annulare e lunghezza dei lembi non sono notevolmente influenzate dalle approssimazioni introdotte dal processo di ricostruzione (differenze percentuali da -0.6% a 40.4%). Al contrario, le altezze dei lembi e commissurali eccedono considerevolmente le misure dirette (differenze percentuali da 8.8% a 281.4%). La sovrastima potrebbe essere dovuta alle seguenti motivazioni: i) il volume è stato campionato in 18 piani radiali equispaziati, quindi la posizione effettiva delle tre commissure potrebbe non essere tra due punti campionati; ii) seppure le zone commissurali fossero visibili sui piani radiali, la geometria è stata ricostruita tramite approssimazioni con funzioni di Fourier del 4th ordine, che trascurano le variazioni locali nella lunghezza del lembo

in direzione annulus-ML. Tutti i risultati mostrati, sono concordi con la criticità dovuta alla non chiara visibilità del ML nelle immagini ecocardiografiche, che risulta in una non corretta segmentazione di tale sottostruttura valvolare.

Il comportamento biomeccanico delle quattro valvole analizzate è stato simulato da FD a PS. I risultati, esemplificati per una sola valvola (Figure 14), mostrano una incompleta coaptazione dei lembi. L'analisi del movimento dei lembi durante la chiusura, della distribuzione delle deformazioni e degli sforzi, suggeriscono che la mancata coaptazione dei lembi sia probabilmente dovuta ad un eccessivo effetto di *tethering*, causato dall'azione delle corde tendinee, data la forma del margine libero dei lembi. Inoltre, per la posizione relativa di MP e inserzioni cordali, in alcuni casi il lembo si muove, non solo verso il centro dell'orifizio valvolare, ma anche circonferenzialmente, ostacolando la chiusura della valvola. Un esempio di questo comportamento è riportato in Figure 14, per una delle quattro valvole analizzate.
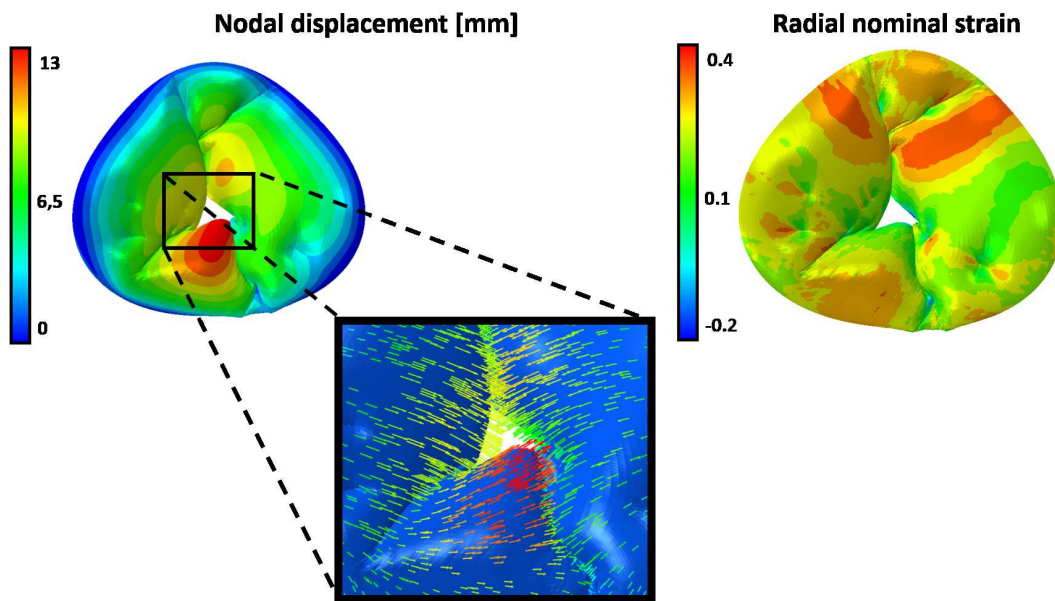

Figure 14: Mappa colorimetrica dello spostamento nodale, riportato in mm, e delle direzioni dei vettori risultanti (a sinistra); campo delle deformazioni radiali nominali a PS (a destra).

Conclusioni

Nel presente lavoro di tesi è stato proposto un nuovo metodo per lo studio della biomeccanica della VT, integrando approccio sperimentale e computazionale. La campagna sperimentale effettuata sul simulatore della circolazione polmonare ha permesso di ottenere una ricostruzione realistica della geometria della valvola, ponendo le basi per la definizione del primo modello agli elementi finiti completo, derivante da immagini e implementato con le proprietà mecca-

niche della VT. Il modello preliminare ottenuto, seppure presenti delle limitazioni dovute al processo di elaborazione della geometria dalle immagini, alla scarsità di informazioni riguardo la morfologia e le proprietà meccaniche della VT, può essere considerato un primo tentativo verso una modellizzazione accurata della biomeccanica della valvola tricuspide.

Chapter 1

Anatomy and physiology

1.1 The heart

The heart is a muscular organ, located in the thoracic cavity, medial to the lungs and posterior to the sternum. It is divided into four chambers: left and right atria; left and right ventricles. The two sides are separated by an internal fibrous and muscular wall of tissue, called the septum (Figure 1.1).
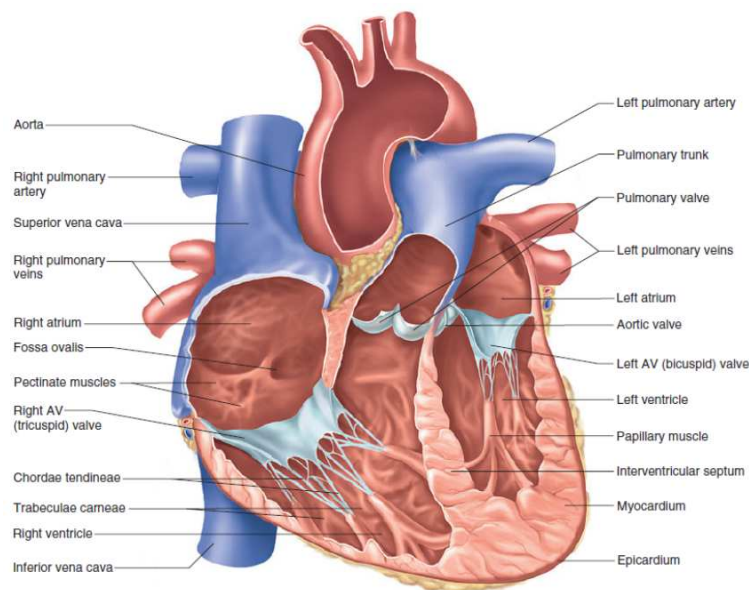

Figure 1.1: A schematic illustration of the human heart [1]

A double-membraned sac, named the pericardium, covers and protects the heart. The outer wall of the heart chambers consists of three tissue layers: as depicted in Figure 1.2, a relatively thick myocardium is sandwiched between an inner endocardium, that silhouettes the chamber, and an outer epicardium, that covers the wall.
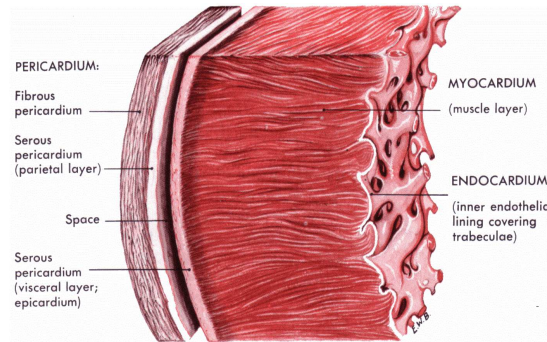
Figure 1.2: Section of the heart wall [2]

Functionally, the heart can be represented as a pulsatile pump providing the body with oxygen and nutrients. To prevent blood from flowing backwards, a system of one-way valves is embedded in the heart [2]. Two types of valves are present:

- the atrioventricular (AV) valves are located between the atria and ventricles. The AV valve on the right side is called the tricuspid valve; the one on the left side is named the mitral valve or the bicuspid valve;

- the semilunar (SL) valves are located between the ventricles and the arteries that carry blood away from the heart. The SL valve on the right side is the pulmonary valve; the SL valve on the left side is the aortic valve.

Although the heart valves are placed in different parts of the heart, they all lie on the same almost planar structure, the so called valvular plane (Figure 1.3).
The opening and closing of the valves are driven by a pressure difference over them and define the phases of the cardiac cycle. A single cycle of cardiac activity can be divided into two basic phases: diastole and systole (Figure 1.4). Diastole represents the period of time when the ventricles are relaxed and passively filled; systole represents instead the time during which the left and right ventricles contract and eject blood into the aorta and pulmonary artery, respectively. Each beat of the heart involves five major stages [4]:

- diastole : the SL valves close, the AV valves open, and the whole heart is relaxed;

- atrial systole: the atrium contracts and blood flows from atrium to the ventricle;

- isovolumic contraction: the ventricles start contracting, all the valves are closed, and there is no change in volume of the ventricular cavities;

- ventricular ejection: the ventricles are contracting and emptying, and the SL valves are open;

- isovolumic relaxation: pressure decreases, the ventricles begin to relax, and the SL valves close.
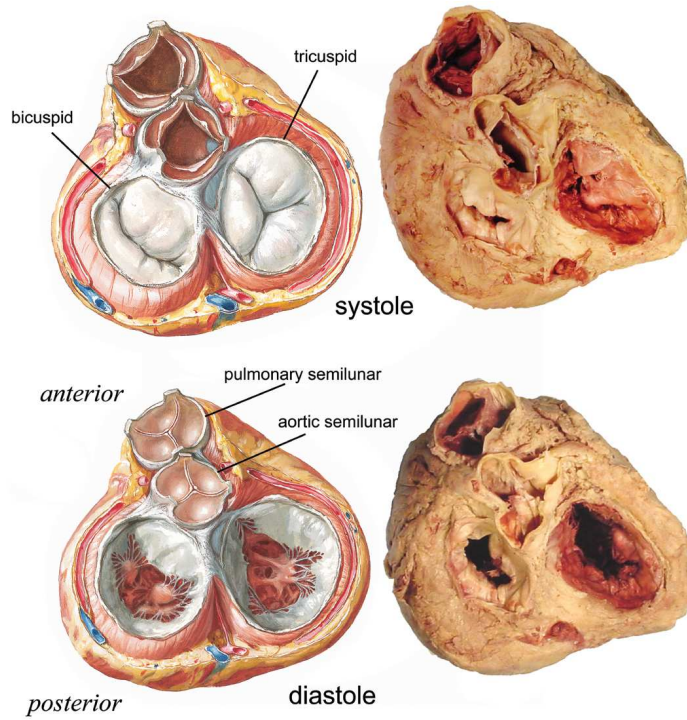

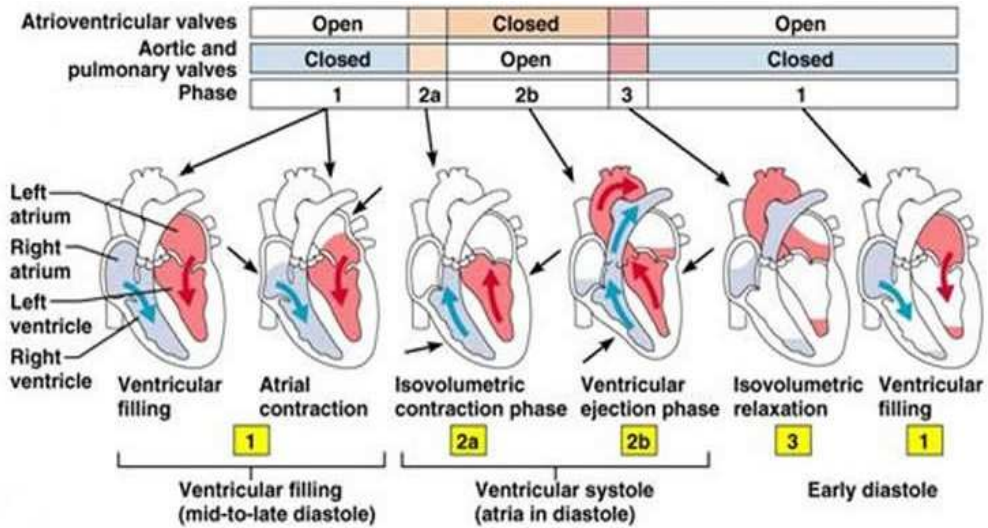Figure 1.3: Representation of the valvular plane [3]

Figure 1.4: Cardiac cycle phases

1.2   The tricuspid valve

The tricuspid valve (TV) allows blood for flowing from the right atrium to the right ventricle (RV). Therefore, it is closed in systole and open in diastole. The TV is the biggest among the cardiac valves, with a orifice area of 7-9 cm^2 in healthy subjects [5]. The complex architecture of TV comprises the annulus, the leaflets, the chordae tendineae and the papillary muscles (Figure 1.5). Each of these structures is described in the following sections.
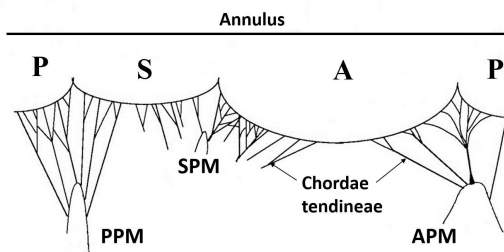
Figure 1.5: A sketch of TV architecture, adapted from [6]. A=anterior leaflet, P=posterior leaflet, S=septal leaflet, APM=anterior papillary muscle, PPM=posterior papillary muscle, SPM=septal papillary muscle.

1.2.1   The valve annulus

The tricuspid valve annulus (TA) is the line of insertion of the leaflets on the cardiac wall (Figure 1.6).

Figure 1.6: Atrial aspect of the adult human heart, adapted from [7]. PT=pulmonary trunk, AV=aortic valve, MV=mitral valve, TV=tricuspid valve (the dashed line sketches the TA).

This fibrous structure does not appear as a ring, showing rather an elliptical shape. According to a recent study [8], the mean dimensions of the human tricuspid 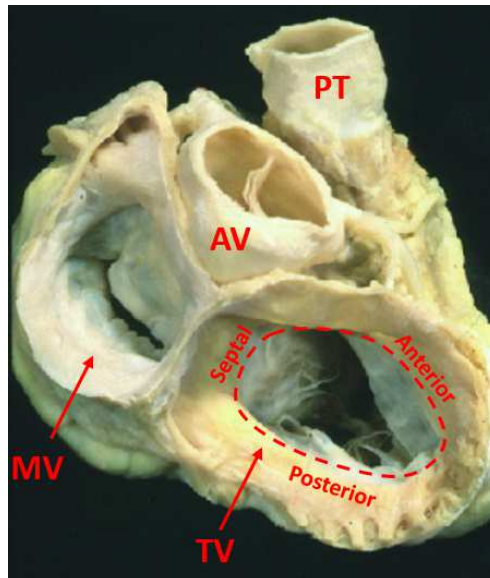annulus are 35 mm for the minor axis and 37.5 mm for the major one. The TA is far from being planar. It has a 3-dimensional structure resembling a saddle, although Fukuda and colleagues [9] found, from echocardiographic measurements, that the TA presents some differences with respect to the well-known saddle-shaped mitral annulus.

As depicted in Figure 1.7(a), the poseroseptal (PS) and anterolateral (AL) segments of the annulus are close to ventricular apex, while the anteroseptal (AS) and posterolateral (PL) segments are close to the atrium. In particular, the highest point is located in the AS segment, the lowest in the PS one (Figure 1.7(b)).

(a)   (b)
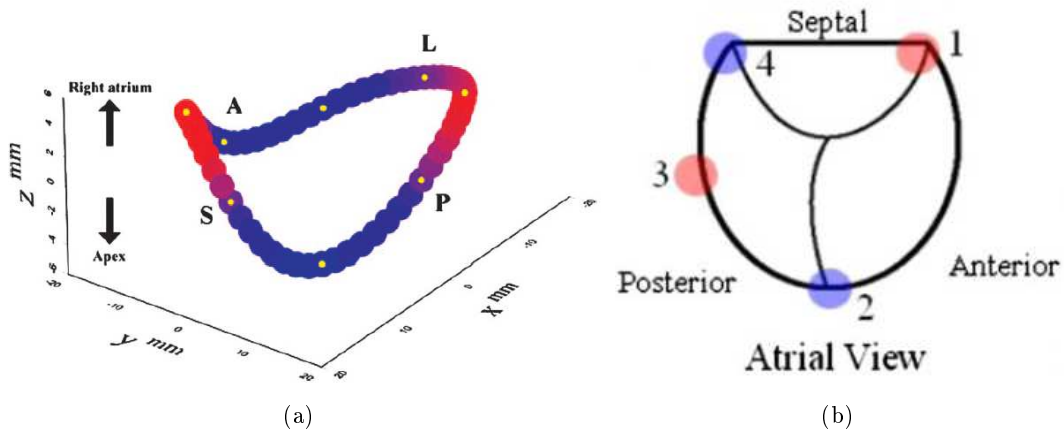
Figure 1.7: (a) 3D reconstruction of TA, showing the saddle shape [9]. The red points are located toward the atrium, the blue ones toward the apex; (b) sketch of TV annulus, showing highest (red) and lowest (blue) points of the profile [10].

Dynamic changes characterize the annulus during the cardiac cycle. The TA area increases from mid-systole to early diastole and again in late diastole, while decreasing in mid-diastole and at the beginning of systole [9] (Figure 1.8). Along the longitudinal direction, the TA moves towards the ventricular apex in systole and towards the atrium in diastole [11]. The TA longitudinal displacement is lower in the antero-septal region with respect to the posterior region, due to the presence of the septum [8], as shown in Figure 1.9.

1.2.2   The leaflets

The TV leaflets appear as fibrous cusps attached to the annulus. In diastole the cusps open, descending into the right ventricle and allowing for ventricular filling, while they are closed in systole to prevent from backward flow in the atrium. The TV has normally three leaflets of different shape and size [12], which exhibit great variability among subjects (Figure 1.10(a)).
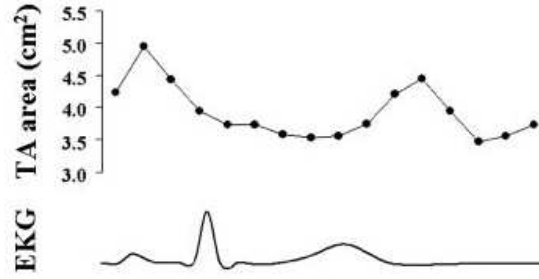
Figure 1.8: Dynamic changes in TA area during a cardiac cycle in a healthy subject [9].
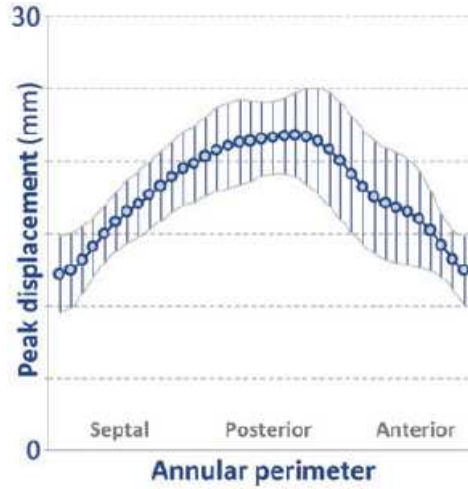

Figure 1.9: Longitudinal peak displacement of TA along the perimeter [8].

The anterior leaflet is the largest and has a semi-circular or quadrangular shape, while the septal one has a semi-oval shape. The posterior leaflet may be easily identified by the presence of several indentations (up to four), named clefts [13], which provide its typical scalloped appearance, shown in Figure 1.10(b).

In Table 1.1 the mean thickness for each leaflet is reported, as measured experimentally by Heyden [15] on porcine TV samples.

	Anterior	Posterior	Septal
Thickness [mm]	0.69±0.45	0.55±0.28	0.63±0.23

Table 1.1: Mean thickness (± standard deviation) measured for each TV leaflet [15])

The junctions of adjacent leaflets to the annulus are called commissures: these are named anteroposterior (AP), posteroseptal (PS) and anteroseptal (AS). Actually, TV commissures appear more like indentations than true junction points [5] and, unlike the mitral valve, their position with respect to TV annulus is not yet known from literature.
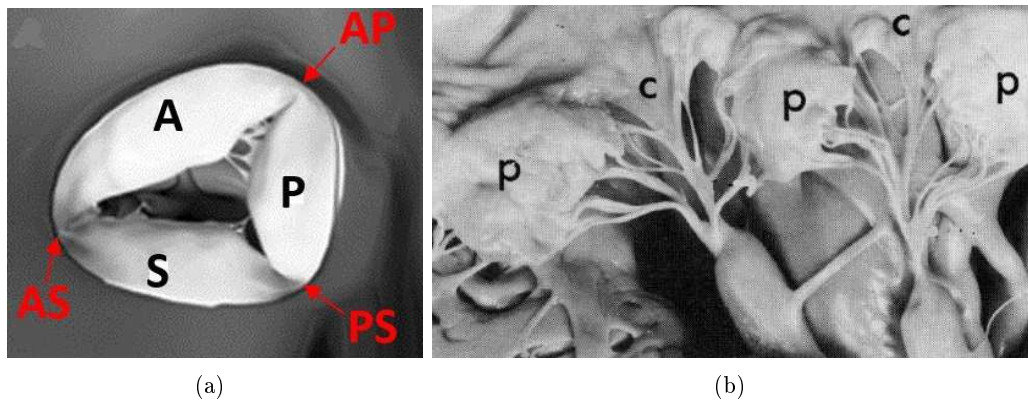
(a) (b)

Figure 1.10: (a) Reconstruction of the TV, showing the three leaflets and commissures, adapted from [14]. A=anterior, P=posterior, S=septal. ; (b) View of the posterior TV leaflet (p), divided by several clefts (c) [12].

Each leaflet is divided in three regions characterized by different thickness and lealflet texture (Figure 1.11). The rough zone extends from the free margin of the cusp to the line of closure, thus being identified with the coaptation region. This area is rough and thick due to the insertion of the chordae tendineae. The basal zone extends from the annulus down to 2-3 mm. The clear zone is comprised between the rough and the basal ones, it is thin, smooth and translucent.
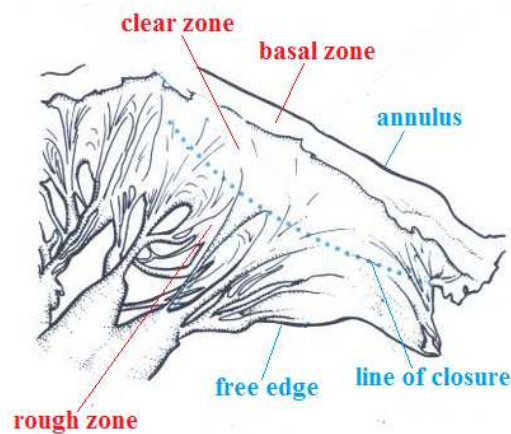
Figure 1.11: Sketch of a TV leaflet, showing the rough, clear and basal zone, adapted from [16].

Concerning microstructure, the TV leaflets are multi-layer structures, characterized by an endocardial surface and a fibrous skeleton [17] [18]. The former is composed of endothelial cells arranged close together or in a roof tile fashion, thus providing structural integrity under maximum stretch. The latter is made up of two layers: the lamina fibrosa and the lamina spongiosa (Figure 1.12). The lamina fibrosa is a dense layer rich in collagen, while the lamina spongiosa appears as a loose connective tissue, composed of collagen, elastin, and glycosaminoglycans

(GAGs). These fibers are arranged with a peculiar pattern in each leaflet and are known to orient themselves in the direction of the principal stresses during the cardiac cycle, thus allowing the leaflets to bear the applied loads [17].

Figure 1.12: Histology of TV leaflets, showing a higher concentration of collagen at fibrosa compared to spongiosa, adapted from [17].

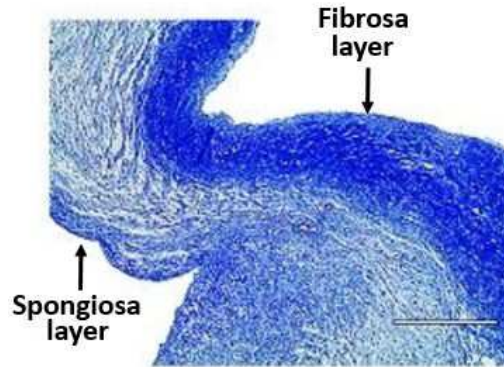The resulting stress-strain response is nonlinear, anistropic and differs among the leaflets, as displayed in Figure 1.13, showing experimental data from biaxial tests performed on porcine TVs by Heyden et al. [15] (a) and on human TVs by Pham et al [19] (b). In both cases, the samples were loaded along fibre and cross-fibre directions and preconditioned with repeated load cycles before testing, so to obtain repeatable measurements. The significant difference in the state of stress of the two works is related to the preconditioning imposed in the two studies. In particular, Heyden et al. applied a force of 2 N over a sample cross section of 5 mm^2, resulting in a tissue prestress of 0.4 MPa: this high level of preconditioning leads to a maximum stress of 0.3 MPa, compared to 0.07 MPa obtained by Pham et al.

1.2.3 Chordae tendineae and papillary muscles

Chordae tendineae and papillary muscles constitute the subvalvular apparatus of the tricuspid valve. Their synergic action supports the coaptation of the leaflets during systole, avoiding the prolapse of the cusps into the atrium due to the increased ventricular pressure.

As described in several studies on right ventricle morphology, papillary muscles and tendinous cords are extremely variable in number, shape, and location [20]. Nevertheless, the general and most common characteristics of these structures can be summarized.

Papillary muscles (PM) arise from the ventricular wall with a number varying from two up to five. Most commonly, the right ventricle is provided with three papillary muscles, which are anterior, posterior, and septal (Figure 1.14) and are approximately positioned below the commissures.

(a)

(b)
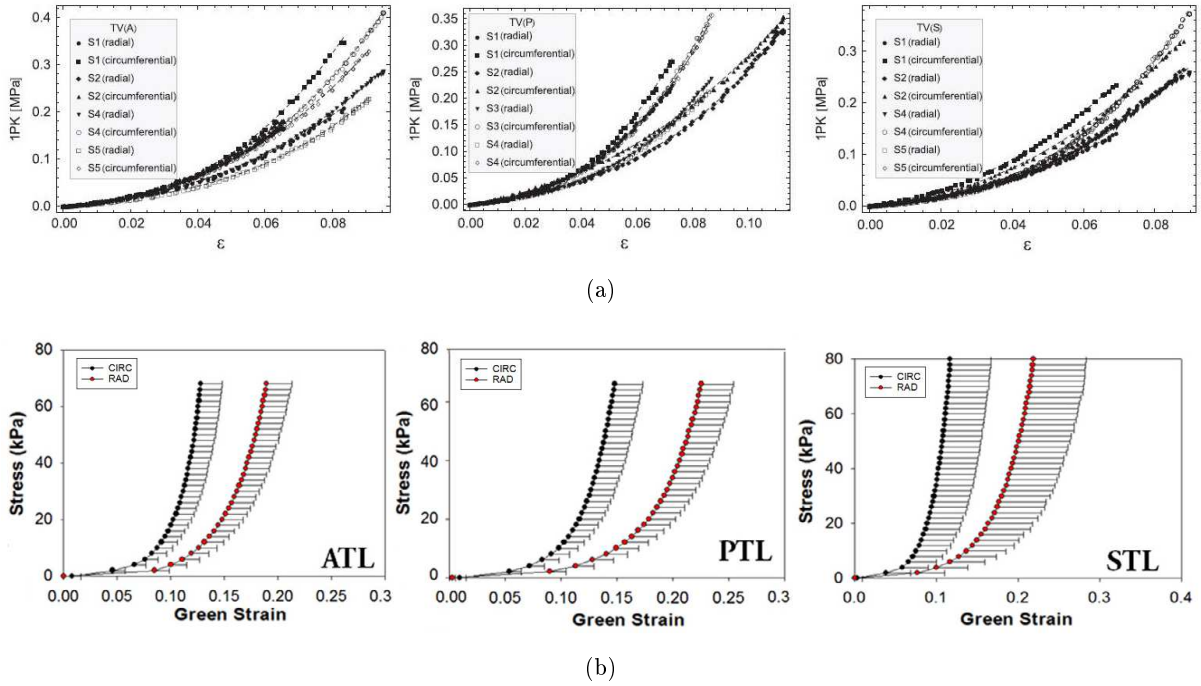
Figure 1.13: (a) Stress-strain response in radial and circumferential directions for anterior (A), posterior (P) and septal (S) leaflets, evaluated on porcine samples [15] (a) and on human samples [19] (b).
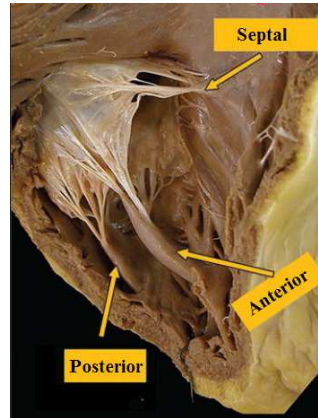
Figure 1.14: View of the three papillary muscles, adapted from [21].

The anterior PM is the largest and most prominent one and it is characterized by a single or double head, while the other two ones may have a number of heads ranging from one to four [20]. In particular, the posterior papillary muscle is small as compared to the others and it is missing in 20% of the healthy subjects [5].

The chordae tendineae arise from the tip of the papillary muscles, even if they could also originate directly from the septal or posterior ventricular wall. These structures are fibrous cords that split in several branches soon after their origin and insert onto the ventricular side

of the leaflets. The chordae have a cross-sectional area ranging from 0.11 to 0.24 mm^2 and are characterized by a great variability both in length and number: on average, the tricuspid valve shows 25 cords, with the highest number inserting into the septal leaflet. TV chordae tendineae are commonly classified in three groups, according to the site of the insertion onto the leaflet [12], as represented in Figure 1.15.
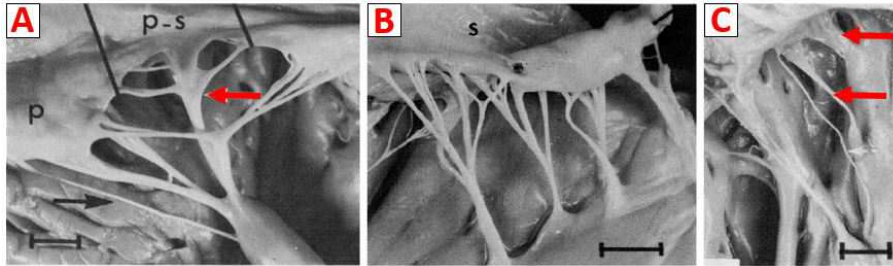
Figure 1.15: Images of the three groups of TV chordae tendineae, adapted from [12]. (A) Free edge chordae (red arrow) attached to postero-septal (ps) commissure. (B) Rough zone chordae inserting onto the septal leaflet (s). (C) Basal chordae (red arrows) attached to septal leaflet.

The free edge chordae insert at the free margin of the cusp, branching finely in a delta pattern, and are usually located below the commissures. The rough zone chordae insert into the rough zone of the leaflets, dividing in three branches or more. The basal chordae arise from the myocardium to insert approximately at 2 mm from the annulus and are usually without branches. They are characterized by great shape variability: they may be find as round cords or ribbon-like structures, long and thin or short and thick. Concerning morphology, the tricuspid chordae are made of collagen bundles, approximately oriented along the long axis of the chorda, with each bundle composed of a network of collagen fibrils [22]. These fibrils appear to be quite evenly distributed over the cross section, covering about 30% of the cross-sectional area. In Figure 1.16(b), the typical nonlinear stress-strain response of TV chordae is reported, deriving from uniaxial tensile tests.

(a)   (b)

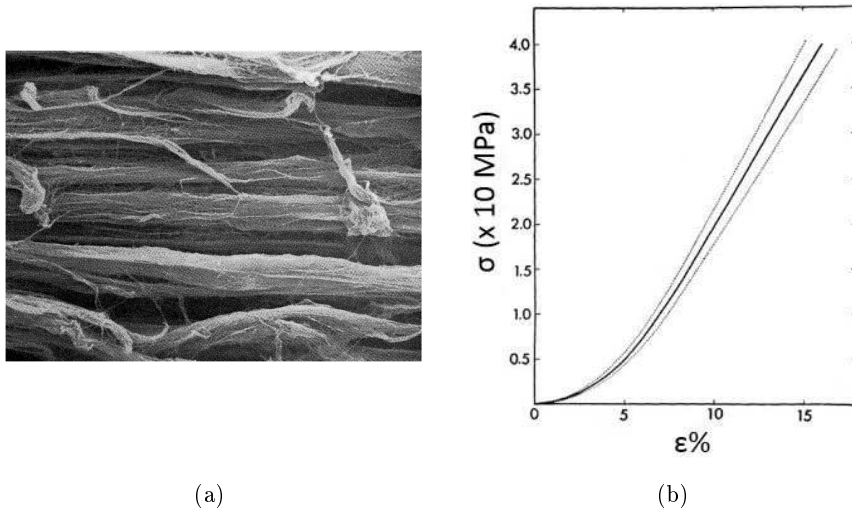Figure 1.16: (a) Scanning electron micrograph of TV chordae tendineae, showing collagen bundles [22].(b) Stress-strain curve derived from unixial tensile test on TV chordae tendineae [22], with the two broken line denoting the standard error.

1.3 Diagnostics and treatments

Diagnostic techniques

Currently, the imaging techniques employed by clinicians to visualize the cardiac valves comprise: echocardiography, both transthoracic (TTE) and transesophageal (TEE), magnetic resonance imaging (MRI), and computed tomography (CT). Echocardiography is referred to the gold standard for diagnosis [23].

Differently from the aortic valve and from the mitral valve, the TV cannot be visualized in a single 2D echocardiographic view. Conversely, 3-dimensional echocardiography (3DE) is a reliable and feasible technique to assess TV morphology and function, with important implications on the surgical decisional planning in case of TV diseases [24]. As exemplified in Figure 1.17, 3DE, with its unique capability of obtaining a short-axis plane of the TV, allows for simultaneous visualization of the three leaflets moving during the cardiac cycle and their attachment in the tricuspid annulus from both the ventricular and the atrial side.

Two different methods for 3DE data acquisition are currently used: real-time or live 3DE imaging and electrocardiographically triggered multiple-beat 3DE imaging. Real-time or live 3DE refers to the acquisition of multiple pyramidal data sets per second in a single heartbeat. Although this methodology overcomes the limitations imposed by rhythm disturbances or respiratory motion, it is limited by poor temporal and spatial resolution. In contrast, multiple-beat 3D echocardiography provides images of higher temporal resolution (i.e. 6 Hz for single-beat acquisitions and 28 Hz for multi-beats mode [25]). This is achieved through
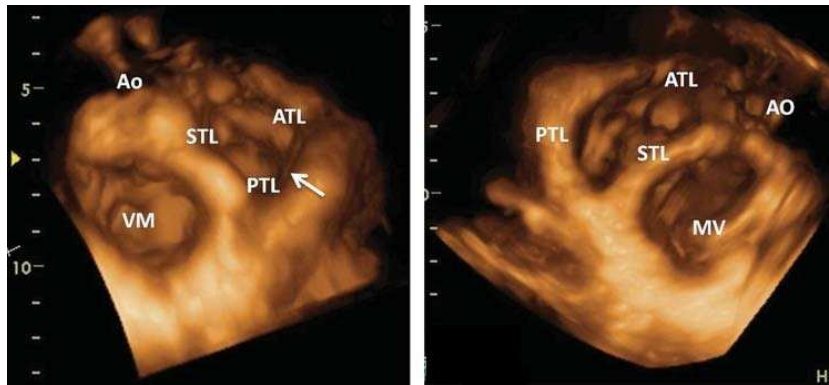
Figure 1.17: Normal TV leaflets visualized by real-time three-dimensional echocardiography from atrial (left panel) and ventricular side (right panel). ATL, anterior tricuspid leaflet; Ao, aorta; MV, mitral valve, PTL, posterior tricuspid leaflet; STL, septal tricuspid leaflet [24].

multiple acquisitions of narrow volumes of data over several heartbeats (ranging from two to seven cardiac cycles) that are subsequently stitched together to create a single volumetric data set [26] (Figure 1.18). The disadvantage of this method is the possibility of stitch artifacts, caused by patient respiratory motion or irregular cardiac rhythm, that are visible when the subvolumes are joined (Figure 1.19).
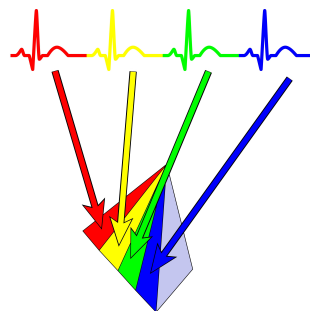
Figure 1.18: Multiple-beat 3D echocardiography, adapted from [26]

Despite its confirmed clinical value, 3D echocardiographic assessment of the TV has some limitations [27]:

- no standard approach to imaging is present;

- the transducer is so large that, in the presence of narrow intercostal spaces in TTE, the acoustic window restricts the penetration of ultrasound beams and the entire displays of structures are affected;

- the imaging depth is not satisfactory: in some phases of cardiac cycle, some structures, as the RV and the sub-valvular apparatus, can only be partly displayed.
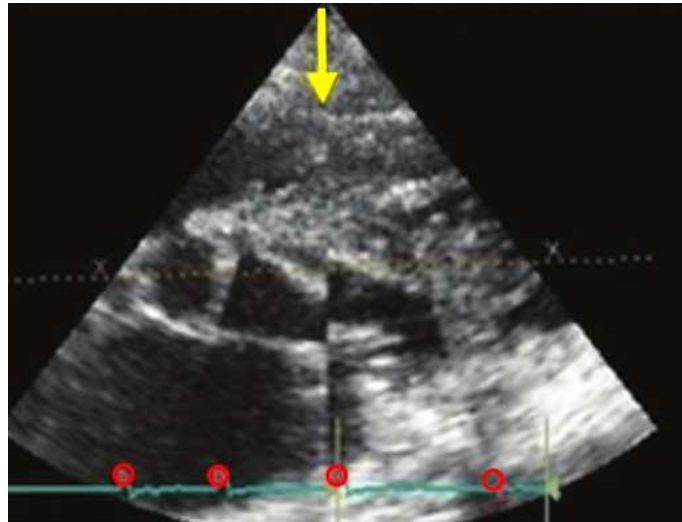
Figure 1.19: Stitching artifact coming from 4-beats 3DE [28]

Tricuspid valve diseases and treatments

Generally, two kinds of pathologies affect tricuspid valve:

- tricuspid regurgitation (TR): the valve is leaky or does not close properly, and blood flows back into the right atrium;

- tricuspid stenosis: the valve leaflets are stiff and do not open widely enough, causing a decreasing in the amount of blood that can flow from the right atrium to the right ventricle.

TR is more common than tricuspid stenosis: currently, moderate-to-severe TR affects ~ 1.6 million patients in the United States [29]. This pathology can be secondary to damage of the TV structures (degenerative TR) or to structural changes in the right heart (annular dilation and ventricular enlargement) that lead to improper TV leaflet coaptation, such as functional tricuspid regurgitation (FTR). Depending on the TR severity, the clinicians can treat it with medical or surgical management. In case of mild TV disease, drugs to control heart failure or to manage an irregular heart rhythm could be prescribed to treat the symptoms. When valve disease is severe, repair or replacement of the valve may be necessary.

The standard surgical treatment of FTR is tricuspid annuloplasty, which involves the implantation of rigid or flexible annular bands to restore the size and the shape of the native annulus and allow the leaflets to open and close completely. Long-term studies have suggested that repair with a prosthetic ring is more durable than suture repair techniques [30]. Nevertheless, the rate of FTR recurrence or reoperations remains high, with in-hospital mortality as high as 25% to 35%, particularly in patients with prior left-sided valve surgery [31] [29].

Thus transcatheter approaches to FTR are raising great interest. Some of the techniques that have been developed for the percutaneous treatment of mitral regurgitation may be adapted to the TV. Different devices, under pre-clinical and clinical evaluation, can be summarized [29].
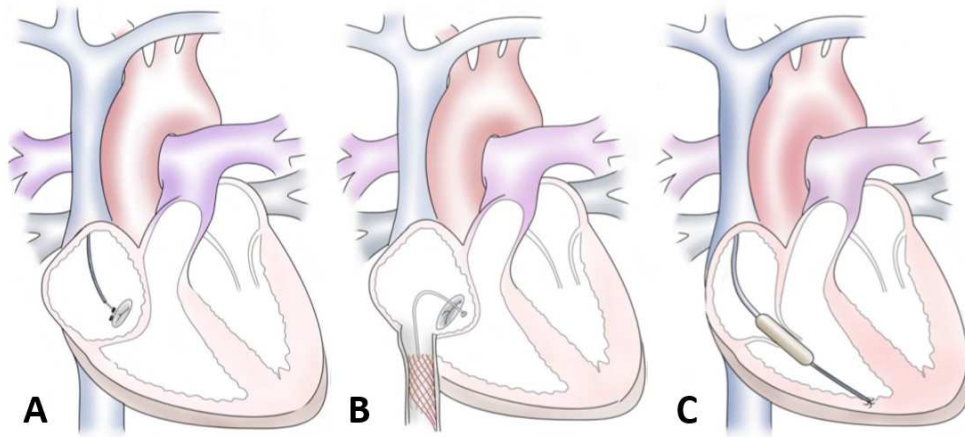

Figure 1.20: TR percutaneous treatments. A: plication of the annulus with the Mitralign device and reduction of its dimension; B: the TriCinch system is tensioned to reshape the annulus and the stent is deployed to maintain the tension applied; C: the FORMA spacer is positioned into the tricuspid orifice and distally anchored to RV. [29]

The Mitralign device (Mitralign, Inc. Tewksbury, USA), has recently been used to convert an incompetent TV into a competent bicuspid valve by plication of both the anterior and posterior tricuspid annulus (TA) [32]. A steerable catheter is advanced in the right ventricle (RV) across the TV and positioned under echocardiographic guidance (Figure 1.20 A).

The TriCinch (4Tech Cardio, Galway, Ireland) is a catheter-based device consisting of a corkscrew anchor, a self-expanding stent, and a Dacron band connecting both. It was designed to perform tricuspid annular cinching, so to reduce anteroseptal annular dimension and improve leaflet coaptation (Figure 1.20 B).

The FORMA Repair System (Edwards Lifescience, Irvine, USA) is a valve spacer, which is positioned into the regurgitant orifice to create a platform for native leaflet coaptation. The device is delivered through transubclavian venous access and is then distally anchored to the RV apex (Figure 1.20 C).

An initial human experience with the Mitraclip device (Abbott Vascular, Santa Clara, California) for treating severe TR via the transjugular or transfemoral vein approach was recently reported in 4 patients. The device was successfully implanted and associated with acute TR reduction in all patients [32]. However, MitraClip therapy has not yet been translated successfully for use in the normal tricuspid position.

Although most patients undergo valve repair, some patients need valve replacement: the surgeon removes the patient's original valve and replaces it with a biologic or a mechanical prosthetic valve.

Chapter 2

State of the art

Patient specific finite element models (FEMs) of cardiac valves are reliable and effective tools for the evaluation of new clinical devices and repair procedures in order to aid surgical planning.

To this aim, several computational models have been developed for the mitral and the aortic valves, which are the most studied up to now, since they are affected very frequently by pathologies requiring surgical intervention. So far, patient specific FEMs for the tricuspid valve (TV) have not been designed, due to the lack of information on anatomical features and tissue mechanical properties of the so called "forgotten valve" [33].

Recently, a great interest has arisen around TV, as revealed by the growing number of percutaneous techniques developed for the treatment of TV pathologies in the last years. To date, mock circulation loops (MCLs) are the only available environment in which these innovative devices and repair procedures can be tested, by studying the hemodynamic effects induced on the valve. However, MCLs cannot provide a pointwise description of the state of stress and deformation generated on the valve, which is important to evaluate potential stress-or-strain-mediated remodelling and inflammation induced by the procedure.

In this context, the development of computational simulations of TV repair procedures would be useful and clinically relevant, providing quantitative information on stress and strain induced on the valve that cannot be obtained experimentally. Therefore, in this thesis we attempt to make a step in that direction, presenting a reliable approach to define a FEM of TV, starting from in vitro data acquired on a MCL.

To provide input data for the definition of a computational model of TV, a MCL should fit the following specifications:

- housing an entire right heart, since the complex structure of the TV interacts with the right ventricle during the cardiac cycle;

- activation through a pumping system allowing to replicate pulsatile conditions and to generate a physiological flow waveform;

- presence of an afterload simulator, representing the impedance of the pulmonary circulation;

- presence of pressure transducers, to record the load acting on the valve in the MCL;

- allowing imaging of the TV structures to define the geometry of the FEM and the dynamics of the valve components.

In literature, the right MCL which best fits the above requirements is the one designed by Castagna and Lentini [34] at Department of Electronics, Information and Bioengineering (DEIB) of Politecnico di Milano (Figure 2.1).

Mock circulation loop for the right heart

The MCL of Politecnico di Milano allows to simulate the pulmonary circulation through the set-up presented in Figure 2.1. The system houses a right porcine heart (a) and is activated by the pumping system (b), which is inserted through a connector in the septal wall of the sample. The afterload simulator (c), representing the pulmonary impedance, is connected to the heart at the level of the pulmonary valve (PV), while the preload (d) is connected to the atrium.
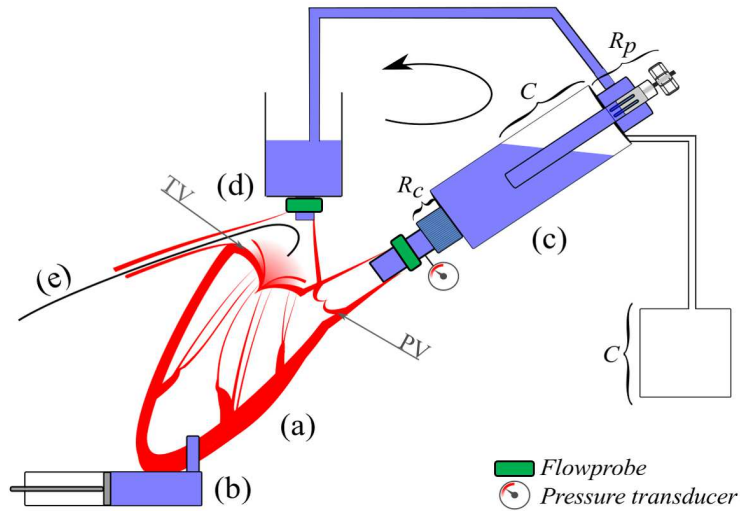

Figure 2.1: MCL sketch, adapted from [35]. TV: tricuspid valve; PV: pulmonary valve; (a): right porcine heart; (b): pumping system; (c): pulmonary impedance system; (d): pre-load; (e): fiberscope; Rc: characteristic resistance; C: compliance chamber (divided in two compartments); Rp: peripheral resistance with adjustment mechanism. The arrow indicates direction of fluid flow.

The pumping system (Figure 2.2) consists of a brushless motor, driven by an electronic controller. The motor moves a ball screw, that transforms the rotational movement of the motor shaft in the translation of a piston, moving inside a cylinder filled with a service fluid. The pump is specifically designed to replicate the cardiac systolic and diastolic flow waves and to reproduce different physiological and pathological conditions, by setting the angular velocity and stroke of the piston, corresponding respectively to the heart frequency and stroke volume.
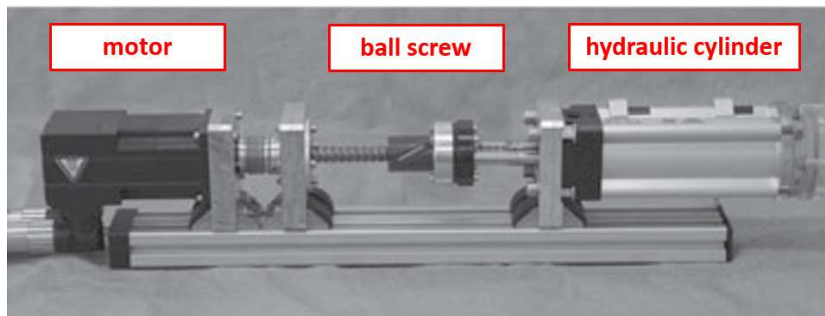
Figure 2.2: Pumping system, comprising a brushless motor, a ball screw and a hydraulic cylinder [34].

The pulmonary impedance simulator is based on the three parameters model shown in Figure 2.3, comprising the characteristic resistance (Rc), the compliance (C) and the peripheral resistance (Rp). The values of the parameters were taken from literature [36].
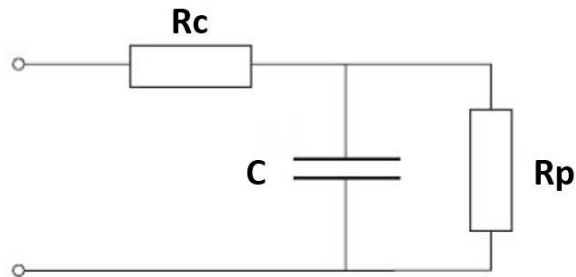
Figure 2.3: Electrical corresponding circuit for pulmonary impedance: Rc characteristic resistance; C compliance; Rp peripheral resistance. [34].

The characteristic resistance is made of a bundle of tubes placed in parallel inside a collector (Figure 2.4(a)). The compliance and the peripheral resistance are shown in Figure 2.4(b): the compliance is obtained by compressing and expanding air within a chamber; the peripheral resistance consists in a partializer inserted in a hollow cylinder provided with four rectangular slits. The sliding of the partializer inside the cylinder, realised turning a screw, reduces the slits area through which the fluid eventually flows, allowing to adjust the value of the peripheral resistance to simulate different working conditions.
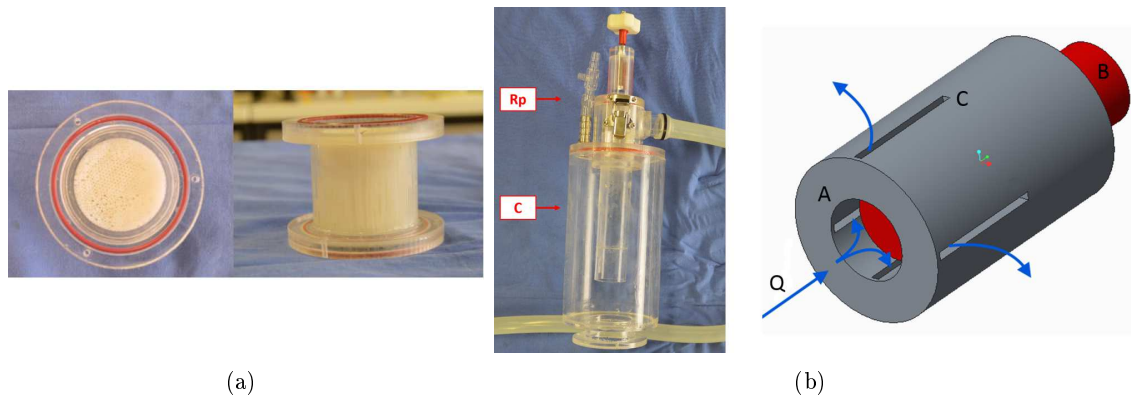
Figure 2.4: Afterload components: (a) two different views of the characteristic resistance. (b) Picture of the compliance C and peripheral resistance Rp (right); sketch of Rp, showing the hollow cylinder (A), the partializer (B) and the slits (C). Arrows show the directions of the fluid flow (Q) [34].

The preload is made through a reservoir, in which the height of the fluid can be adjusted to set different levels of preload. The pulmonary and atrial connectors connect the heart respectively to the afteroad and preload (Figure 2.5). All these components are made of PMMA.
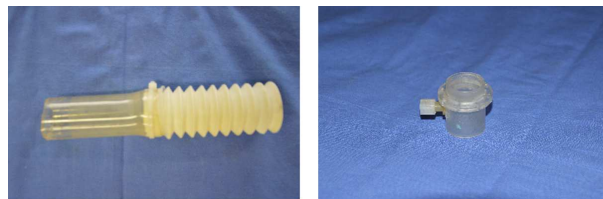
Figure 2.5: Atrial (left) and pulmonary (right) connectors [34].

Flow measurements are performed with ultrasonic flowmeters (HT110R Transonic systems Inc, Ithaca, NY) at the pulmonary and atrial connector. Two accesses have been designed to record the pressure at the pulmonary connector and at the afterload, using piezoresistive transducers (PC140 series, Honeywell Inc, Morristown, NJ). Furthermore, needles inserted in the atrium and in the ventricle allow to record the transvalvular pressure.
The MCL is equipped with a fiberscope, thus allowing for the visual inspection of the TV while performing the experimental campaign.

The MCL presented by Castagna and Lentini is a reliable simulator of the pulmonary circulation and can be easily adjusted to replicate physiological and pathological conditions, in terms of heart frequency, flow rate and pressure acting on the system. Therefore, this set-up is suitable to provide the input data needed to define the FEM of the TV.

Since the MCL was recently designed, no experience of imaging of the TV from this set-up is available. To understand the possible solutions to acquire images from MCLs, we reviewed the scientific literature, finding interesting examples, which are described below.

A left heart simulator for the definition of the mitral valve geometry through micro-computed tomography and echocardiography

This left simulator was specifically developed at the Georgia Institute of Technology by Rabbah et al. to validate a computational model of the mitral valve (MV) and it was optimized to allow for micro-computed tomography (CT) and echocardiographic acquisitions [37].
As depicted in Figure 2.6, the system houses an excised ovine MV, with the annulus sutured to a silicon and acrylic plate and the papillary muscles attached to mechanical holders. The sample is inserted in a cylindrical thin-walled acrylic chamber simulating the left ventricle. The MCL is provided with an atrial chamber and an aortic chamber, in which a 25 mm bi-leaflet mechanical heart valve is mounted, functioning as the aortic valve.
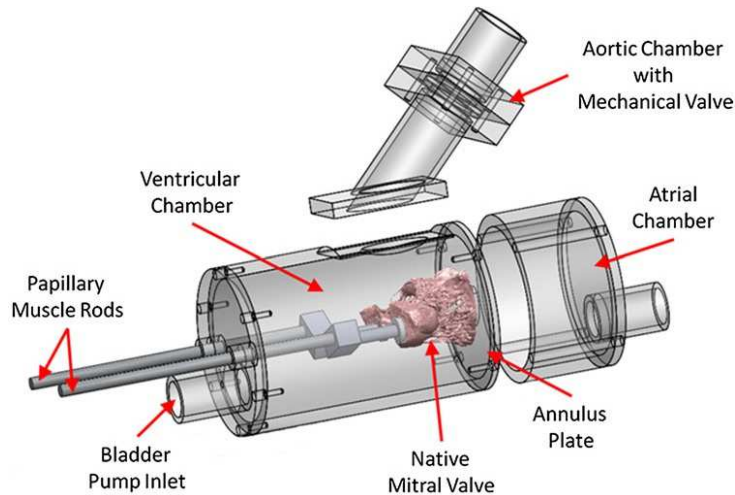
Figure 2.6: Design of the left heart proposed by Rabbah et al. [37].

The choice of using an isolated MV is critical, since the atrioventricular valves have a complex structure interacting with the ventricle. In particular, the annulus plate and the rigid ventricle used in this MCL do not allow to mimic the native annular dynamic and ventricular motion. Besides, this set-up induces arbitrariness in the positioning of the papillary muscles, being isolated from the ventricle on which they insert in vivo.
Imaging of the MV was performed on this MCL, using micro-CT to assess the valve geometry and three-dimensional echocardiography to monitor the valve kinematics.
For the tomographic acquisitions, the aortic and atrial chamber were removed and the ventricular chamber was fixtured to the micro-CT gantry. The MV was scanned in air with the

system at rest, using scanning parameters optimized for low density soft tissues, allowing to provide images with excellent contrast for the geometrical reconstruction. Due to the high spatial resolution (in this work 39 μm voxel), micro-CT is particularly suitable to provide a detailed and accurate description of the intricate branching of the chordae tendineae.

Echocardiographic acquisitions were performed in full volume on the moving MV, using a pediatric probe. With three-dimensional echocradiography it is possible to non-invasively capture the valve dynamics, without interfering with the function of the MCL. The good temporal resolution (in this work 50 Hz) allows for the investigation of the leaflets geometry to define the computational model at any point of the cardiac cycle.

The review of the study conducted by Rabbah et al. is useful to understand the potential and the critical aspects of the two imaging techniques mainly performed on the MCLs.

The CT and even more the micro-CT are characterized by excellent spatial resolution, allowing for a detailed and accurate representation of all the cardiac structures. On the other hand, to perform these acquisitions, the valve has to be inside the CT gantry, thus implying limitations in the design of the MCL. Furthermore, if the whole set up is not properly designed to be inserted into the CT scan, non moving acquisitions of the valve have to be performed, without the possibility to assess the motion of the valve structures.

Three-dimensional echocardiography has a high temporal resolution, enabling the evaluation of the valvular dynamics throughout the whole cardiac cycle. The spatial resolution, even if inferior as compared to the one of CT scans, allows for the assessment of complex structures, resulting in high quality images. The echocardiographic acquisitions can be performed non-invasively, with only the probe interacting with the MCL. Moreover, with a view to develop patient specific FEM from clinical imaging, echocardiography presents a series of advantages compared to CT. The ultrasounds have no harmful effects on the patient with respect to the ionizing radiation used in a tomographic scan and no radiopaque contrast agents are needed to perform echocardiographic acquisitions. Echocardiography is widely available, since it is found in virtually all hospitals, and cost-effective, both in terms of equipment and facility costs.

Considering all the topics above discussed, in this thesis we choose three-dimensional echocardiography to perform acquisitions of the TV from the MCL developed by Castagna and Lentini. From this perspective, we reviewed the study of Leopaldi et al., who acquired echocardiographic images from a set-up really similar to the one used in this thesis.

Valve imaging in passive beating hearts

The MCL proposed by Leopaldi et al. was designed at Dipartimento di Elettronica, Informazione e Bioingegneria (DEIB) of Politecnico di Milano. The set-up replicates the systemic circulation, in order to evaluate the hemodynamic effects of surgical procedures in the left heart in pulsatile conditions.

This system, shown in Figure 2.7, shares common features with the set-up developed by Castagna and Lentini. The MCL houses a left porcine heart, pressurized with a volumetric piston pump, connected to the sample at the ventricle apex. The heart is connected at the level of the aortic valve to the systemic impedance simulator, based on the same three lumped model shown in Figure 2.3, in which the values of the parameters are determined in literature for the systemic circulation. The preload to the heart is given through a reservoir connected to the atrium.
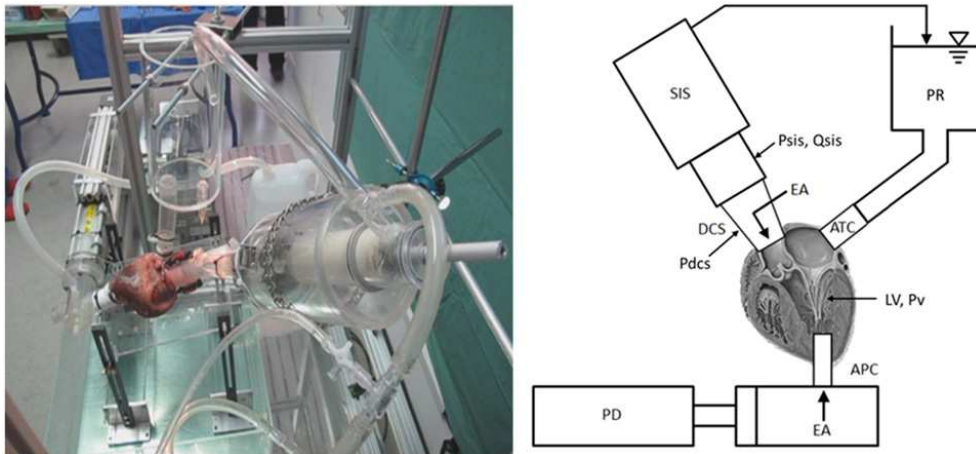
Figure 2.7: Left: picture of the system. Right: schematic of mock loop: pulse duplicator (PD), systemic impedance simulator (SIS), pre-load reservoir (PR), apical connector (APC), atrial connector (ATC), double cone system (DCS), endoscopic accesses (EA) [38].

In this study, echocardiography was performed on both aortic and mitral valves with an ultrasound system (HDI 5000, Philips, Eindhoven, NL) equipped with a 12-3 MHz probe (Philips L12-3). Thanks to the design of the MCL, it was possible to position the probe directly on the pericardium of the sample, allowing for the acquisition of high-quality images of the cardiac structures. Endoscopic acquisitions were also performed, inserting an endoscope lens in the ventricle apex to visualize the mitral valve or in the aorta to visualize the aortic valve.

The simultaneous acquisition of this two imaging modalities (Figure 2.8) ensured a more complete understanding of the cardiac valve dynamics.

Figure 2.8: Left: sequence of endoscopic images showing the opening and closure of the aortic valve (A–D). Center: endoscopic images(E,F) obtained from the apical access, showing the opening and closure of the mitral and aortic valve (MV,AV). The apical access enable the visualization of the chordae tendineae (CT) and the papillary muscles (PM). Right: echocardiographic images of the diastole (G) and of the systole (H) showing the mitral and aortic valves [38].

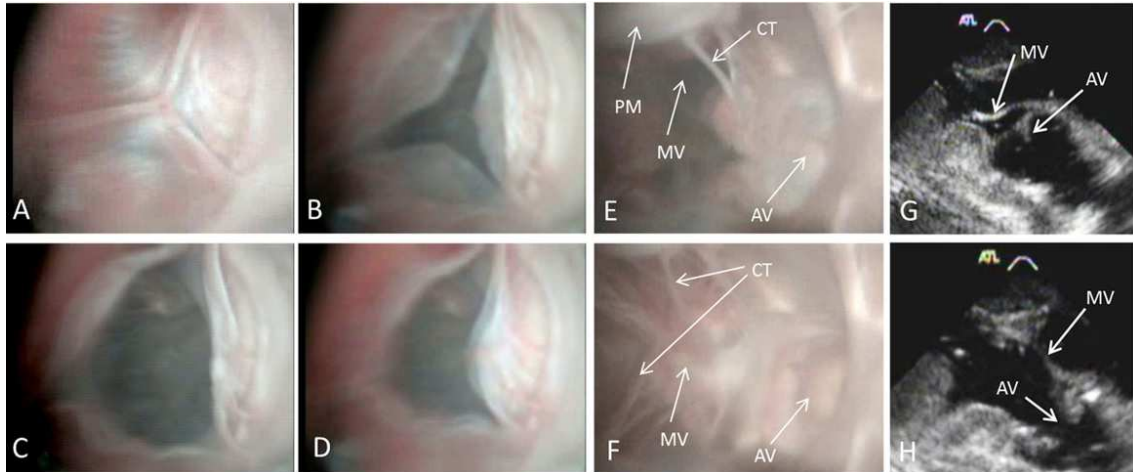The study conducted by Leopaldi et al. demonstrates the potential of the use of echocardiography to acquire images of the cardiac structures from a MCL. The acquisitions are performed without interfering with the functioning of the set-up and provide high-quality images of the valves.

Given the previous considerations, echocardiography results the proper technique to provide images of the TV from which reconstruct the geometry of the valve for the FEM.

To date, no patient-specific FEM of the TV are available in literature. Most of the studies just focus on the reconstruction of the annulus of the valve from echocardiography [39] [9] or from cardiovascular magnetic resonance [8]. The only complete model of TV is the parametric FEM developed by Stevanella et al. in 2010 [40] and certainly represents the reference in the field of the computational model of the TV. Nevertheless, Stevanella et al. created a paradigamtic model, using approximations and simplifying assumptions, which strongly affect the reliability of the model, as discussed in detail in the following section.

Preliminary FEM of the TV

In this study, Stevanella et al. present a FEM of the TV mimicking the physiological behaviour of the valve, to provide quantitative insight into its biomechanical response. The 3D geometry of the model is presented in Figure 2.9 and described below.

No imaging was performed to define the valve geometry, that was reconstructed merging experimental measurements on porcine and human samples with data taken from literature.
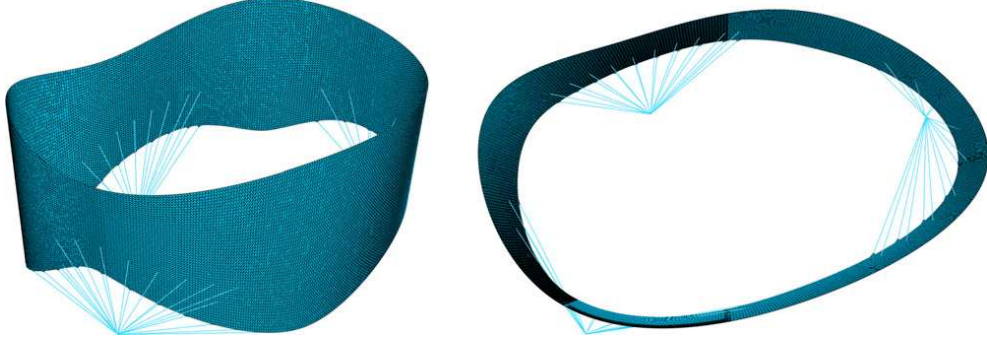
Figure 2.9: 3-D view (left) and atrial view (right) of the unloaded geometrical model of the tricuspid valve [40].

In particular, the annulus was defined from the quantitative data provided by Hiro et al. on ovine TVs [41], interpolating the coordinates of six ultrasonic crystals through a natural cubic spline method. The leaflets were reconstructed based on the annulus-to-free-margin extent of the leaflets as measured experimentally at 12 annular landmarks.

Uniform thickness from experimental observations was assumed for all the leaflets, whose surface was discretized with three-node triangular plane-stress shell elements in ABAQUS/Explicit 6.10 (Simulia, Providence, Rhode Island, USA).

The chordae tendineae were arranged consistently to the experimental observations, considering marginal chordae inserted at the free edge and second order chordae with insertion at two third of the leaflets height. Since ramifications were not taken into account, all the chordae were discretized in 6 tracts to improve the mechanical behaviour under axial compression loads. Each tract was modelled in ABAQUS using two-nodes truss elements with a constant cross-sectional area of 0.171 mm^2.

The papillary muscles (PMs) were placed accordingly with the coordinates of the corresponding three crystals reported in the sonomicrometric study conducted by Hiro et al. and modelled as single nodes, considering negligible the distance between single tips on the same PM. The mechanical behaviour of the leaflets was assumed nonlinear, anisotropic and hyperelastic and was described through the constitutive model originally proposed by May-Newmann for the mitral valve [42], with the following invariant-based strain energy function Ψ:

$$\Psi = c_0[e^{c_1(I_1-3)^2+c_2(\sqrt{I_4}-1)^4} - 1] \tag{2.1}$$

where $I_1 = trace(\mathbf{C})$ and $I_4 = \mathbf{a_0} \cdot \mathbf{C} \cdot \mathbf{a_0} = \lambda^2$, in which $\mathbf{C} = \mathbf{F} \cdot \mathbf{F^T}$ is the right Cauchy-Green tensor, $\mathbf{a_0}$ is the unit vector which defines the preferential direction of the fibres within the material in the undeformed shape and λ is the stretch of the fibres in the $\mathbf{a_0}$ direction. $\mathbf{F}$ is the deformation gradient tensor, defined as $\mathbf{F} = \partial\mathbf{x}/\partial\mathbf{X}$, i.e. the derivative of the current

position with respect to the undeformed position.

Due to the lack of information from literature concerning the stress-strain response of TV tissues, the constitutive parameters of the model were identified by fitting experimental data derived for the MV. Since the microstructure of the TV leaflets is unstudied, a sensitivity analysis was performed to compare the numerical results using three different sets of mechanical properties, corresponding to different fibre arrangements. In particular, the authors assumed high circumferential arrangement of fibres as in the MV anterior leaflets (model A), loose circumferential arrangement as in the MV posterior leaflets (model B) and uniform dispersion of the fibres, implying isotropic response (model C). The values of the parameters for each configuration are presented in Table 2.1.

	Model A	Model B	Model C
c_0 [kPa]	0.399	0.414	0.209
c_1	4.325	4.484	9.046
c_2	1446.5	305.4	0

Table 2.1: Values of the constitutive parameters in the three models [40].

The mechanical behaviour of the chordae tendineae was supposed nonlinear, isotropic and hyperelastic, and it was modelled with a second order polynomial strain energy function, available in ABAQUS/Explicit constitutive models library.

The material constants of the model were identified by fitting the experimental data derived from uniaxial tensile test on TV chordae, reported by Lim et al. [22].

Concerning the boundary conditions, the pressure load applied to the leaflets surface was taken from literature, with a systolic peak value of 23.7 mmHg. The contraction of the annulus was reproduced, defining the displacement of the annular nodes moving from the maximum annular area configuration to the minimum one, in accordance with the time dependency reported by Hiro et al (Figure 2.10). The displacement of the PMs was neglected.

The results of the simulations showed no remarkable differences between the three models concerning both valve kinematics and the stress distribution over the leaflets. As depicted in Figure 2.11, at the systolic peak, the highest stresses were located near the annulus of the anterior leaflet, while the lowest values were found at the commissural regions.

The nominal strains in circumferential direction (parallel to the annulus) showed the same distribution in the three models with different levels of magnitude (Figure 2.12). The annular region was subjected to a mild compression, while the commissural zones experienced the most compressive state.
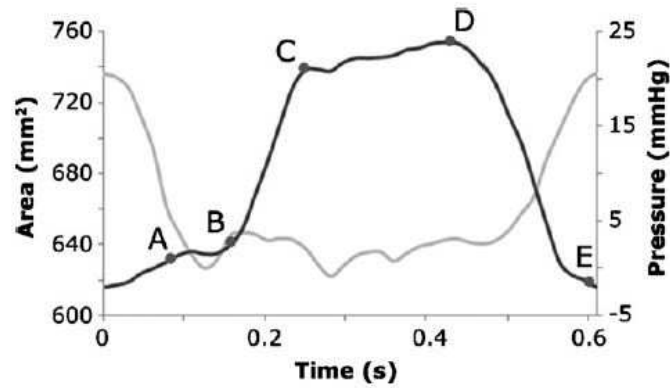
Figure 2.10: Transvalvular pressure (black line) and annular area curves (grey line) versus time. Five time-points (A-E) are highlighted on the curve, with D representing the systolic peak [40].
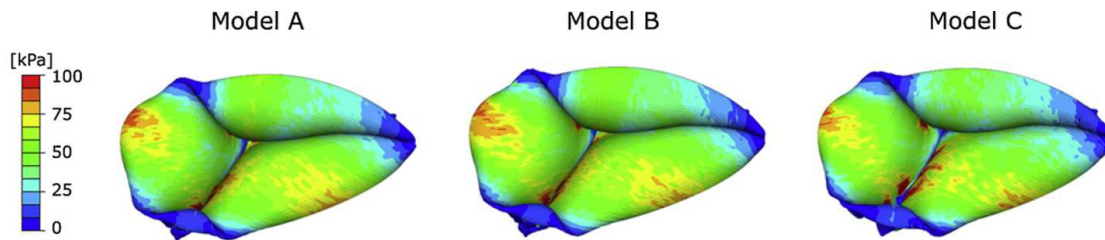
Figure 2.11: Maximum principal stresses in the three models at systolic peak value of 23.7 mmHg [40].

Concerning the longitudinal direction (from annulus to free margin), the leaflets underwent high levels of strain, up to 50% in model A and B, with peak values located generally at the mid-annular region, decreasing towards the commissures and the free-edge.
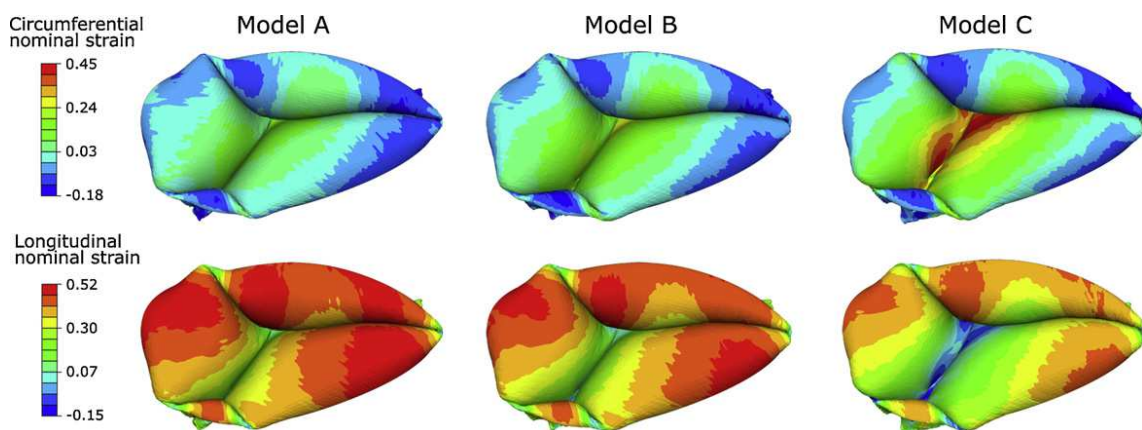
Figure 2.12: Nominal strains distributions at the systolic peak in the three models in circumferential and longitudinal direction [40].

Due to the lack of experimental data on the TV to validate the model, the numerical results were qualitatively compared to experimental and computational data from studies on the MV, finding that the model B is likely the one best resembling the real TV leaflets strain distribution.

Although this study is an important step forward for the development of FEM of the TV, the model designed by Stevanella et al. presents some critical aspects that should be improved, as described below:

- the geometrical model is parametric, obtained mixing *ex vivo* data from human and swine with *in vivo* data from sheep, leading to an idealised geometry of the valve;

- the material constants for the leaflets were determined from experimental data acquired on the MV, which may have a different microstructure with respect to the TV, even if the two valves share similar macrostructure;

- the real complexity of the collagenous structures created by chordal ramifications was not accounted for;

- the boundary conditions assigned to the annulus were derived from experimental data acquired on sheep;

- the pressure load was taken from literature, derived from experimental studies conducted *in vivo* on sheep;

- the leaflets experience extremely large longitudinal strains, which seem unrealistic in physiological conditions;

- a complete validation process need experimental data to compare computational results with.

Based on the considerations done so far, the aim of this thesis is to provide a reliable approach for the development of a FEM of the TV, integrating experimental and computational methods. To this end, we used the MCL to acquire experimental data, which were computationally elaborated to reproduce the valve geometry, the annulus kinematics and the pressure load acting on the valve. This information was taken as input to define a numerical model of the TV, overcoming some limitations of the FEM proposed by Stevanella, with the aim to provide a reliable geometrical framework and a more realistic characterization of the biomechanical response of the leaflets.

Chapter 3

Materials and methods

The aim of this thesis is to develop the first complete finite element (FE) model of a tricuspid valve deriving from 3D echocardiographic image data. This model may serve as a basis for computational simulations to obtain a deeper understanding of TV mechanics, associated to diseased conditions ora to surgical repair.

In this chapter, the workflow and the tools used in the project are described, divided in the following phases:

- acquisition of echocardiographic images of the TV from the mock circulation loop (MCL), developed by the ForCardioLab (Luigi Sacco Hospital, Milan, Italy);

- experimental campaign performed to collect morphometric parameters and provide an anatomical framework of the geometrical modelling of the TV;

- reconstruction and discretization of the TV 3D geometry derived from the images, using custom software developed in MATLAB (The MathWorks Inc, Natick, MA, United States);

- modelling of leaflets mechanical properties;

- development of a computational model for finite elements analyses, performed through ABAQUS/Explicit 6.10 (Simulia, Providence, Rhode Island, USA).

3.1   Image acquisition

Data acquisitions from the MCL were performed using real-time 3-dimensional echocardiography (RT3DE) (iE33, Philips, shown in Figure 3.1) and a TEE probe (CX7-2t).

Figure 3.1: Philips iE33 ultrasound machine.

The MCL was previously designed at Department of Electronics, Information and Bioengineering (DEIB) of Politecnico di Milano [34] to simulate physiological and pathological hemodynamic conditions of the cardiopulmonary circulation. As described in Chapter 2, the central element was represented by a right swine heart, actuated by a pulsatile pumping system through a PMMA cylindrical connector placed on the trans-septal wall. The pulmonary artery was connected to the pulmonary impedance simulator, while the right atrium was connected to the pre-load reservoir (Figure 3.2).

The biological samples, provided by a local abattoir (Salumificio Venegoni, Boffalora Ticino, Italy), were frozen for at least 24 hours at -20 °C and then defrosted for 24 hours at a temperature between 2 and 4 °C. The following procedures were performed on the swine hearts to allow for their positioning on the MCL:

- washing to remove blood clots;

- dissection of the aorta and isolation of the pulmonary artery;

- isolation of both superior and inferior venae cavae: the inferior one was sutured with the tobacco-pouch technique for the fiberscope camera insertion; the superior one was left free to insert the atrial connector;
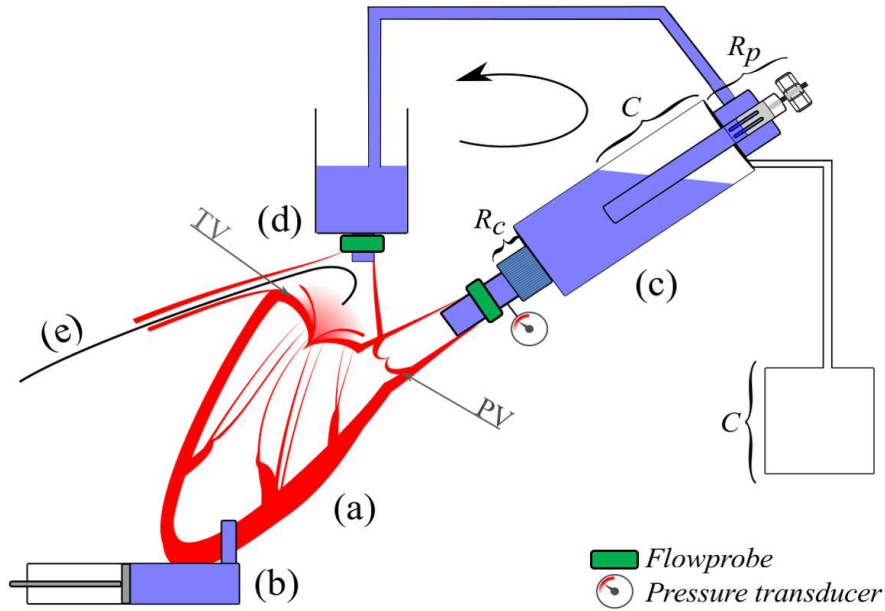
Figure 3.2: MCL sketch, adapted from [35]. TV: tricuspid valve; PV: pulmonary valve; (a): right porcine heart; (b): pumping system; (c): pulmonary impedance system; (d): pre-load; (e): fiberscope; Rc: characteristic resistance; C: compliance chamber (divided in two compartments); Rp: peripheral resistance with adjustment mechanism. The arrow indicates direction of fluid flow.

- removal of the left atrium and ventricle;

- perforation of the intra-ventricular wall using a surgical puncher to insert the pump connector (Figure 3.3(a));

- placing of the circuital connectors: the atrial connector consisted in a corrugate tube; the pulmonary connector, made in PMMA, was sutured on the pulmonary artery and provided with an access to measure pressure; the pump connector was a PMMA cylinder placed in the septal wall (Figure 3.3(b)).

Two methods were devised to control the tendency of the right ventricle (RV) to dilate under pressure in the experimental setup. The dilation resulted in a displacement of the papillary muscles (PMs) anchored to the free wall of the RV, and in the TV annulus enlargement in the antero-posterior direction, causing the anterior and posterior leaflets to move away from septal one, thus introducing TV regurgitation [35]. The first method consisted of two adjustable bands placed at both valvular and PMs levels (Figure 3.4(a)); the second method consisted in creating a stitch, inserted from the inter-ventricular septum to the outer ventricular wall. An external tuning system, connected to the stitch, was used to adjust its tension (Figure 3.4(b)).
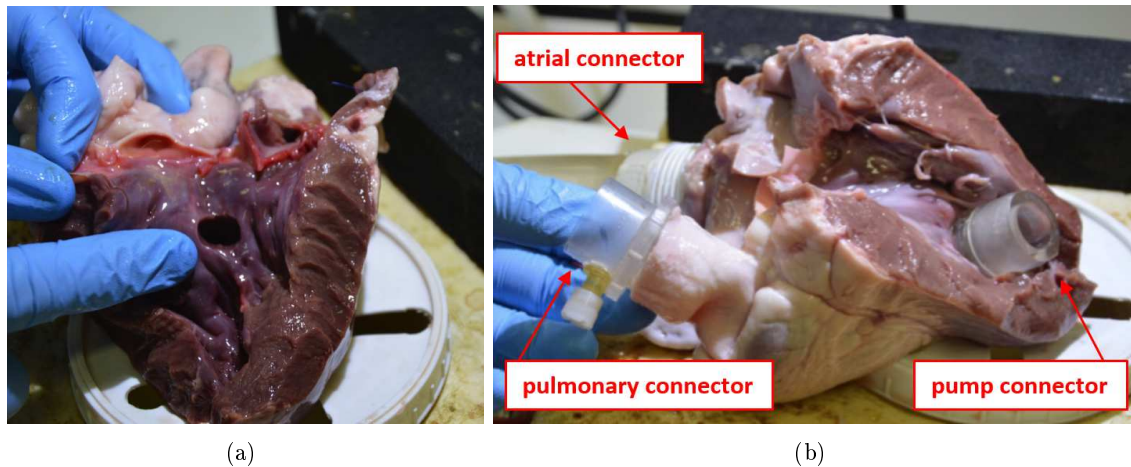
Figure 3.3: Heart sample preparation: (a) perforation of the intra-ventricular wall; (b) placing of the circuital connectors.
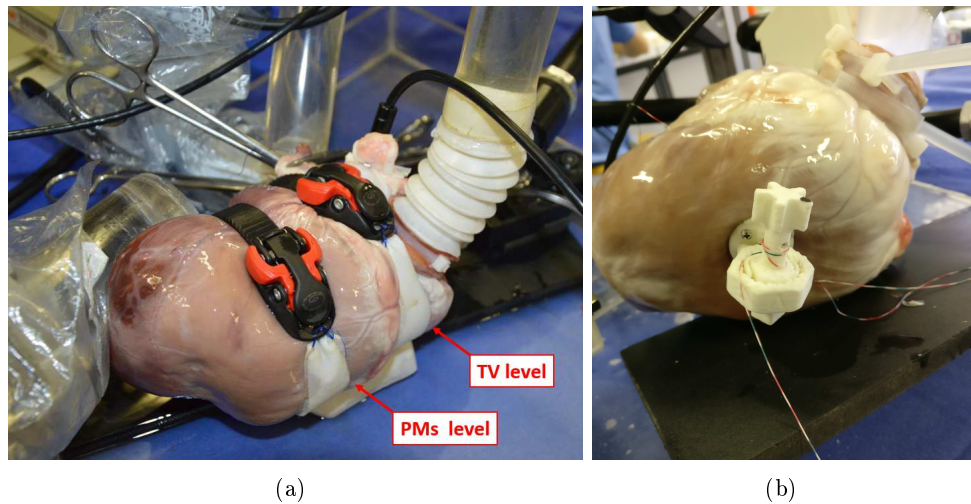
Figure 3.4: Systems to control the RV dilation, adapted from [35]: (a) adjustable bands at the TV annulus and at the PMs level; (b) external regulation system used to adjust the tension of the stitch inserted from the septal to the ventricular wall.

A protocol for the echocardiographic acquisitions from the MCL was defined, acting both on probe positioning and on echo machine settings.

Concerning the first aspect, the best probe positioning was identified in order to acquire the entire ventricle without artifacts shadowing the leaflets. To this aim, we adjusted the experimental set-up, introducing a box filled of physiologic saline solution to house the heart (Figure 3.5) which allows for the positioning of the probe at various distances from the epicardium. The acquisitions were performed testing two configurations: i) with the probe at a fixed distance from the heart (Figure 3.6(a)); ii) with the probe in contact with the epicardium (Figure 3.6(b)). In most cases, the images acquired with the first modality were characterised

by artifacts and shadowing effects due to the presence of the pulmonary and atrial connectors, resulting in a hard and sometimes erroneous identification of the TV annulus and leaflets from the images. For this reason, the best positioning was found placing the probe directly on the epicardium between the two connectors.
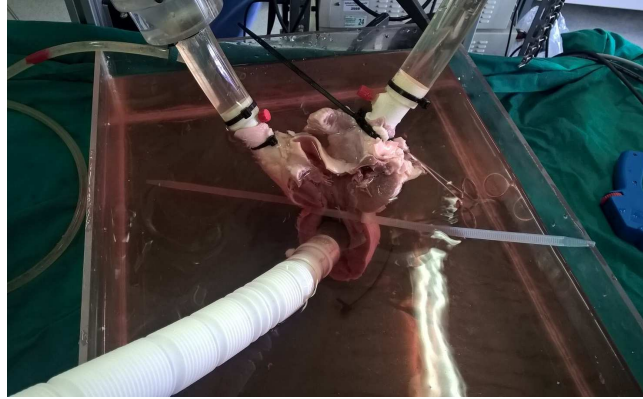
Figure 3.5: Chamber with physiologic saline solution to allow for the positioning of the probe at various distances from the heart.

(a)   (b)
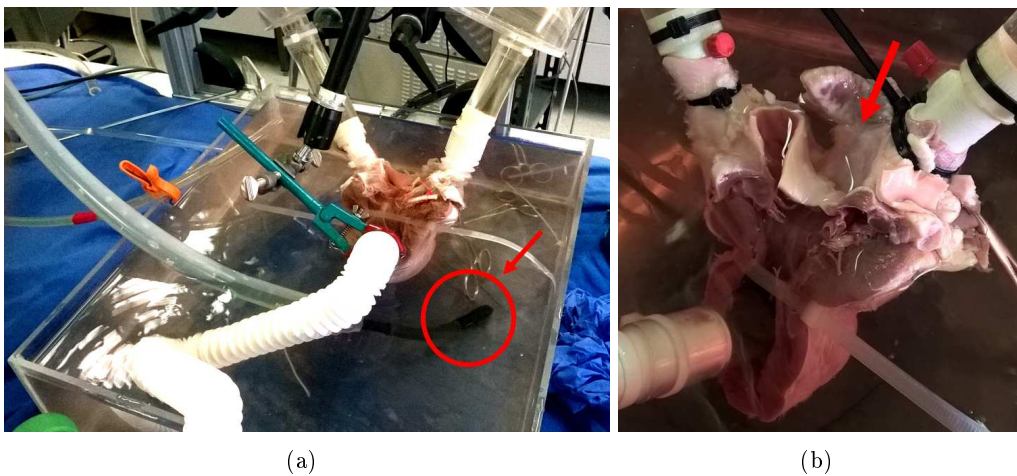
Figure 3.6: Two experimental configurations tested: (a) probe at a fixed distance from the heart; (b) probe in contact with the epicardium between the pre/after-load connectors.

Regarding the echo machine settings, the key aspect consisted in identifying the trade-off between volume rate (i.e., temporal resolution) and spatial resolution. As explained in Section 1.3, to improve temporal resolution the images were acquired with a four-beats 3D method, owing to the fact that, with a stable heart position, no stitch artifacts are visible when the subvolumes are merged. The mean spatial and temporal resolution were respectively 0.696 x 0.688 x 0.538 mm and 30 frames/cycle.

Altogether, these improvements allowed to obtain good quality images to observe both the entire tricuspid valve and the right ventricle.

With the described protocol, the echocardiographic acquisition campaign was run on four porcine hearts, setting the stroke volume to 70 ml and the heart rate to 60 bpm to replicate physiological working conditions.

3.2 Experimental measurements

Experimental measurements were performed on the four tested hearts to quantitatively describe the morphological features of the tricuspid valve.

The valves were excised and cut-open by cutting at the posteroseptal commissure and the following quantities were estimated:

- Annular perimeter;

- Leaflet length;

- Leaflet height, measured from the annulus to the free margin (FM) at the midpoint of each leaflet;

- Commissural height, measured from the annulus to FM at the commissural position;

- Leaflet thickness.

A marking of the annulus was made using a thread to measure perimeter and leaflet lengths (Figure 3.7(a)). Thickness was evaluated using a micrometer with a resolution of 0.01 mm (Figure 3.7(b)); the other dimensions were obtained with a vernier calliper (resolution of 0.01 mm). All data were compared to analytical measurements resulting from images processing.

(a)   (b)
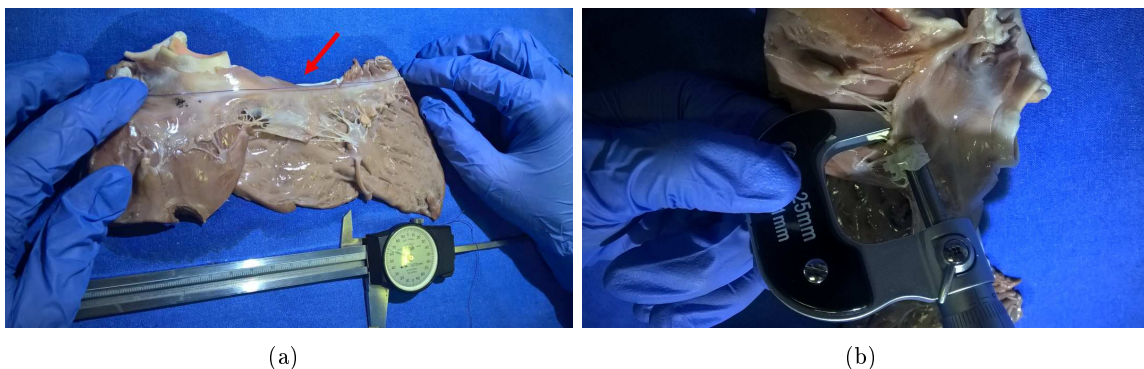
Figure 3.7: Experimental measurements: (a) annulus perimeter, evaluated through a thread and a vernier calliper; (b) leaflet thickness, measured with a micrometer.

3.3 Image processing

The modelling approach defined in this work to process echocardiographic images can be summarized in the following steps, described in detail in this section and depicted in Figure 3.8:

- a reference system was positioned within the acquired raw data (VolDICOM): the origin of the reference frame was located on the centre of the tricuspid orifice; the z-axis was set as the axis approximately orthogonal to the tricuspid orifice plane;

- 18 planes evenly rotated by 10 degrees around the z-axis were generated;

- the TV structures were manually traced on each plane and the valve reconstruction was automatically performed.
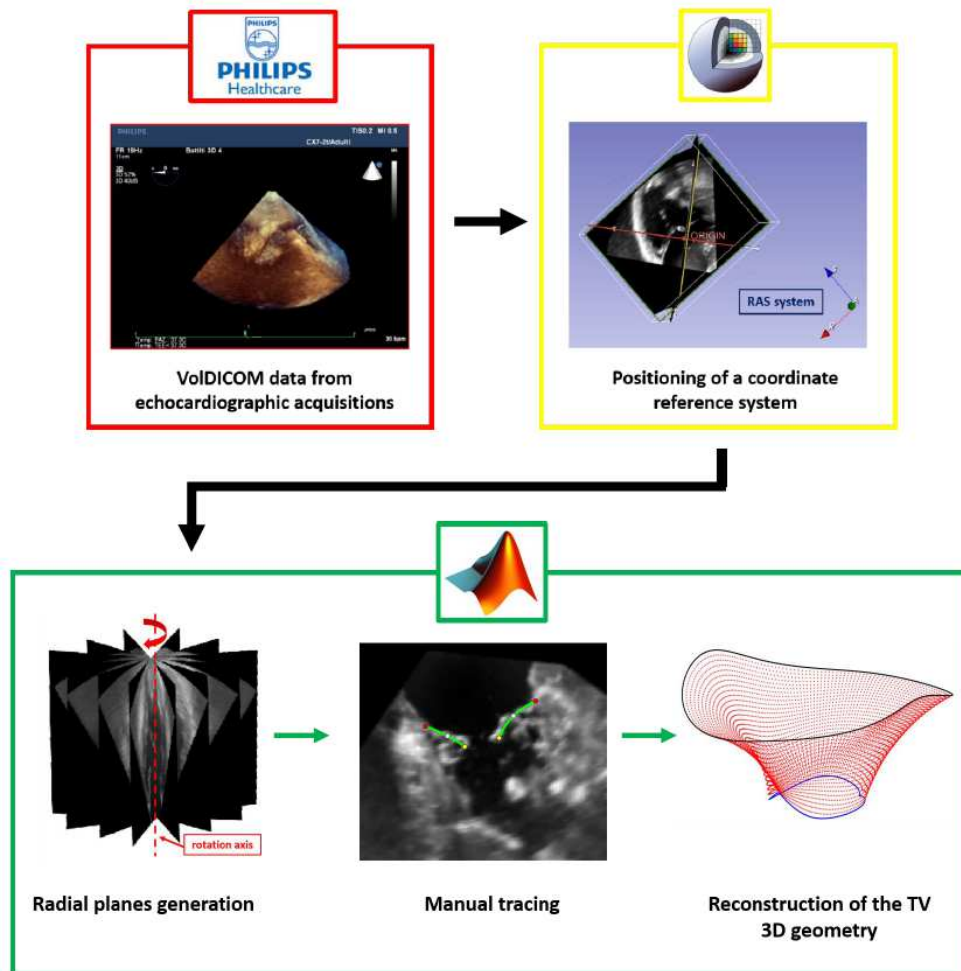
Figure 3.8: Workflow of the image processing: the acquired VolDICOM datum was investigated and a coordinate reference system was positioned; 18 radial planes were generated, and the TV structures were manually traced, so to automatically perform the 3D reconstruction of the valve.

In order to define the reference frame, the VolDICOM datum was investigated with 3D SLICER 4.6 (Brigham and Women's Hospital, Harvard University, NIH), a free open-source software application for medical image computing, which can be used to explore the volume slice-by-slice. An intrinsic right-hand coordinate system (RAS) was positioned and the three main planes (i.e., two long-axis and one short-axis planes) were displayed. 3D SLICER allowed for the roto-translation of these planes so to position the origin in the TV centre, parallel to the annular plane (Figure 3.9). This operation was performed at the end-diastole (ED) frame, chosen as the last frame before the TV starts closing, and provided the RAS coordinates of the origin and the normal directions of each plane.
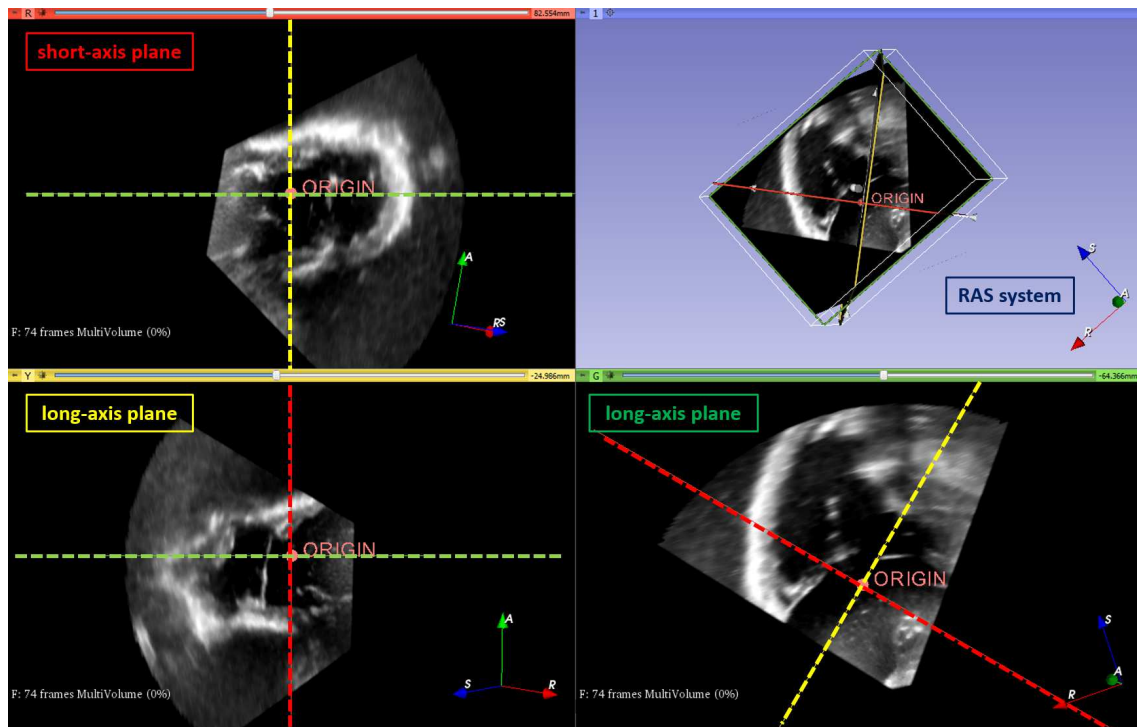
Figure 3.9: VolDICOM investigation with 3D SLICER: exploring the volume slice-by-slice, a coordinate system origin was positioned in the TV centre. The dashed cross-hairs represent the two planes orthogonal to each view.

The outputs were processed by means of dedicated software, developed in MATLAB, with the following approach:

- the RAS coordinates were converted in XYZ coordinates;

- 18 radial planes were generated by rotating a long-axis plane by 10 degrees relative to the axis passing through the origin previously defined (Figure 3.10);

- these planes were oriented taking into account the normal direction of the short-axis plane (parallel to the annular plane);

- values were assigned to each 2D pixel of the plane by interpolating brightness values of the 3D voxels of the volume data intersected by the plane, so to obtain reformatted images.
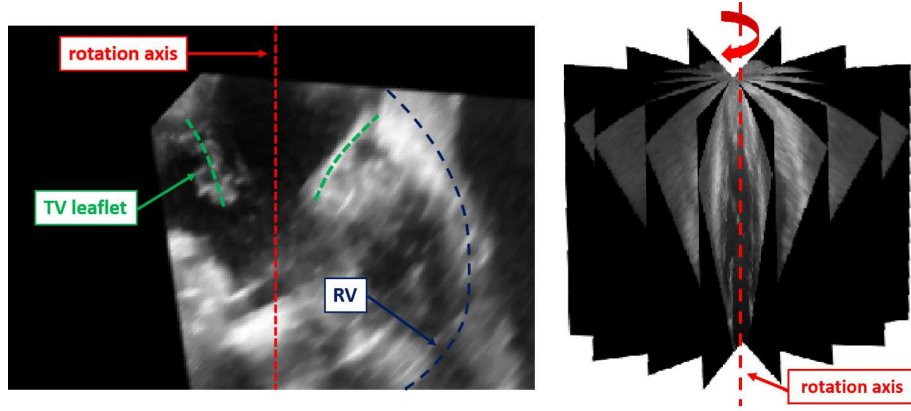
Figure 3.10: Radial planes generation. Left: long-axis plane used as reference plane for the radial rotation. Right: 18 equally spaced radial planes.

As for previous studies on mitral valve reconstruction [43], on each radial plane the TV was segmented at ED, when the valve was hypothesized approximately unloaded.

Two points were manually identified both for the annulus and FM; for each leaflet, traced points were automatically interpolated with cubic splines, which were sampled in 63 points running from the annulus to FM and uniformly distributed along the leaflet length (Figure 3.11).
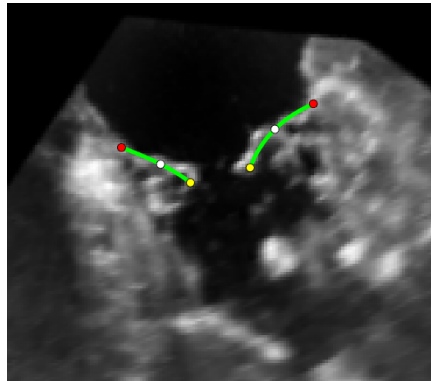
Figure 3.11: Segmentation of a radial plane at ED frame. The red points indicate the TV annulus; the yellow points the FM and the green lines identify the leaflets.

A cylindrical reference system was set with the origin in the centre of mass of the points on TV annulus, and the z-axis normal to the least-square plane of the annular points. In this local reference frame, the radial (ρ) and axial (z) positions of the ith point of every leaflet spline were then approximated through 4th order Fourier functions of the angular position (θ)

in the form:

$$\rho(\theta) = a_0 + \sum_{i=1}^{4}[a_i\cos(i\theta) + b_i\sin(i\theta)] \tag{3.1}$$

$$z(\theta) = c_0 + \sum_{i=1}^{4}[c_i\cos(i\theta) + d_i\sin(i\theta)] \tag{3.2}$$

Every Fourier function was upsampled at n points (in this work 400, with a mean spatial resolution of 0.366 mm), so to reconstruct the TV geometry as a 3D point cloud described by m levels (in this work 63) from the annulus to FM, each with n points uniformly circumferentially distributed (Figure 3.12(a)).

Sampled points were connected, to discretize leaflets surfaces, into a mapped mesh of 3-node triangular plane-stress shell elements, with one integration point in the shell surface and five integration points through the thickness (ABAQUS User's Manual, Chapter 25.6) (Figure 3.12(b)).

Leaflet thickness was assumed uniform and equal to 0.46 mm, averaged from the experimental measurements performed on the four TVs considered in this study.

(a)   (b)
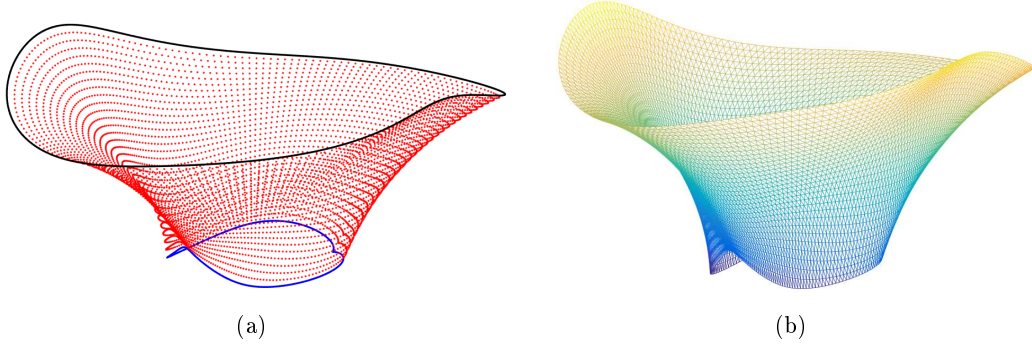
Figure 3.12: (a) 3D point cloud obtained by sampling the Fourier functions approximating leaflets profile; (b) leaflets triangulated mesh.

3.4 Commissures positioning

As discussed in Section 1.2.2 the position of the three commissures on the annular plane has not been described in literature yet. In this work, we implemented two strategies to find the three commissures and to position them on the reconstructed annular profile:

- "analytical" method;

- direct segmentation.

3.4.1   Analytical method

The analytical approach was based on the assumption that the free edge of the TV was characterized by numerous indentations (clefts), the most prominent ones being located at the three commissures [13] (Figure 3.13).
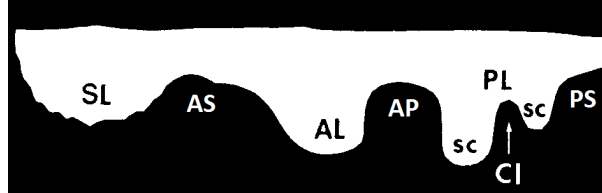
Figure 3.13: Schematic diagram of typical tricuspid valve showing clefts (Cl), commissures (AS, AP, PS), leaflets (SL, AL, PL) and scallops (sc) [13].

Hence, in this work the three major indentations were automatically identified on the valve profile using the following procedure:

- for each leaflet spline, the length was evaluated as the sum of the tracts obtained connecting the 63 points interpolating the splines;

- the position of the first commissure was set at the absolute minimum length (C1 in Figure 3.14);

- based on the location of C1, the annular tract corresponding to the angular position in the range of 120±30 degrees from C1 was investigated, and the second local minimum was identified as the minimum length in that tract (C2 in Figure 3.14);

- the third commissure (C3) was placed starting from C2 with the procedure illustrated at the previous step (Figure 3.14).
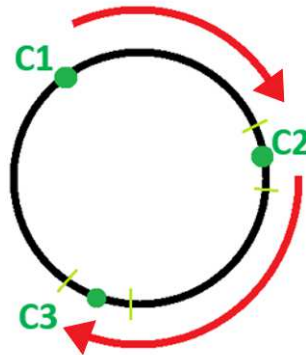
Figure 3.14: Commissural points along the annulus profile, identified with the analytical method.

3.4.2   Direct segmentation

Manual segmentation was performed on the TV short-axis plane in 3D SLICER.

The motion of the TV leaflets during the cardiac cycle was observed to identify the three hinge points of the leaflets on the annulus, corresponding to the commissures. Three markers were then positioned at the systolic peak frame (SP), chosen as the frame in the middle of the systole (Figure 3.15).
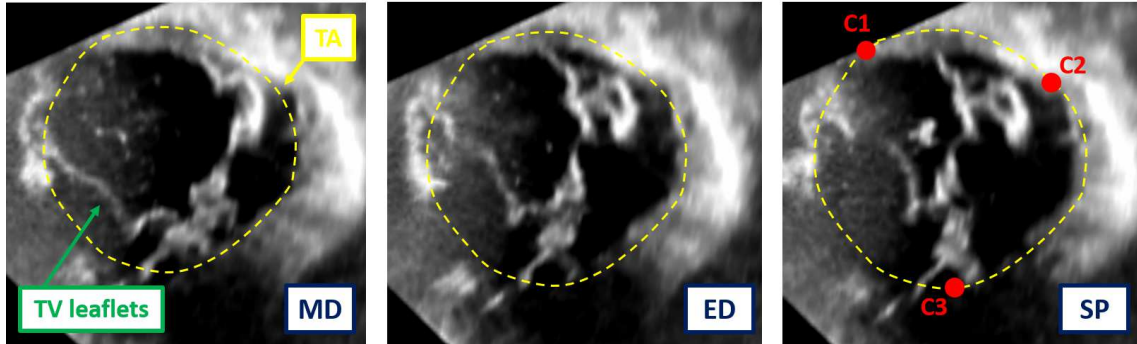
Figure 3.15: Direct segmentation of the three commissures (C1, C2, C3) on the TV short-axis plane in 3D Slicer. MD: mid-diastole; ED: end-diastole; SP: systolic peak; TA: tricuspid annulus.

The RAS coordinates were exported and processed in MATLAB: applying a roto-translation, the points were placed with respect to the origin previously defined, and converted in cylindrical coordinates. The three resulting angular positions were detected on the annular profile (Figure 3.16).
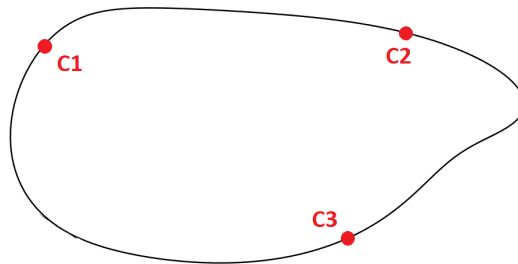
Figure 3.16: Positioning of the three commissures on the reconstructed annular profile.

3.5   Commissures identification

Independently from the adopted method, the identification of the commissures provided three points, but their position with respect to the heart is unknown. This information is crucial to correctly identify the leaflets inserted between the commissures. To this aim, an external anatomical landmark was selected.

We chose the inter-ventricular septum as anatomical reference area for two reasons: i) the position of the commissures with respect to the septum is known [14]; ii) the septum was simply detected on the images, due to the presence of the pump connector, inserted in the septal wall as described in Section 3.1 (Figure 3.17).
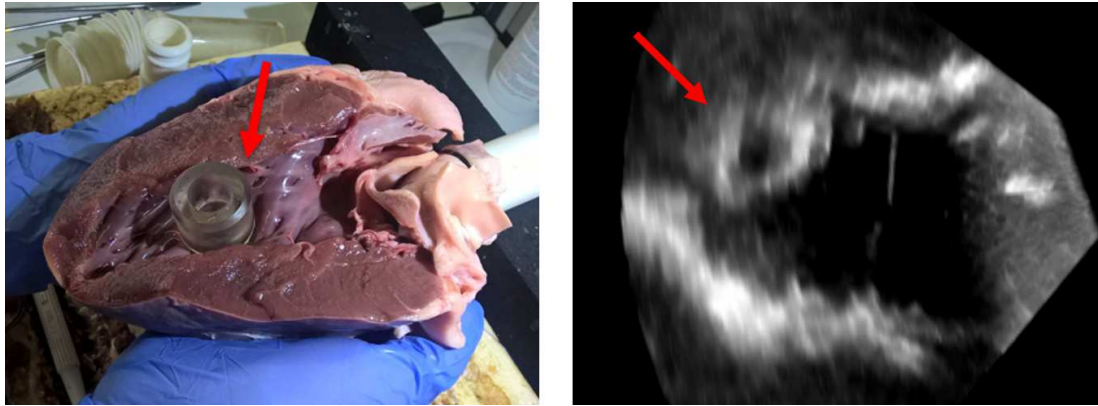
Figure 3.17: Pump connector inserted in the inter-ventricular septum (left) and displayed in the long-axis plane of an acquired image (right)

Investigating slice-by-slice the acquired volume in 3D SLICER, the position of the connector was identified in a long-axis plane and four markers were put to trace the area of interest (Figure 3.18(a)). Reproducing the same procedure performed for the direct segmentation of the commissures, described in Section 3.4.2, the points were located with respect to the reconstructed annulus (Figure 3.18(b)).

(a)　　　　　　　　　　　　　　　　(b)
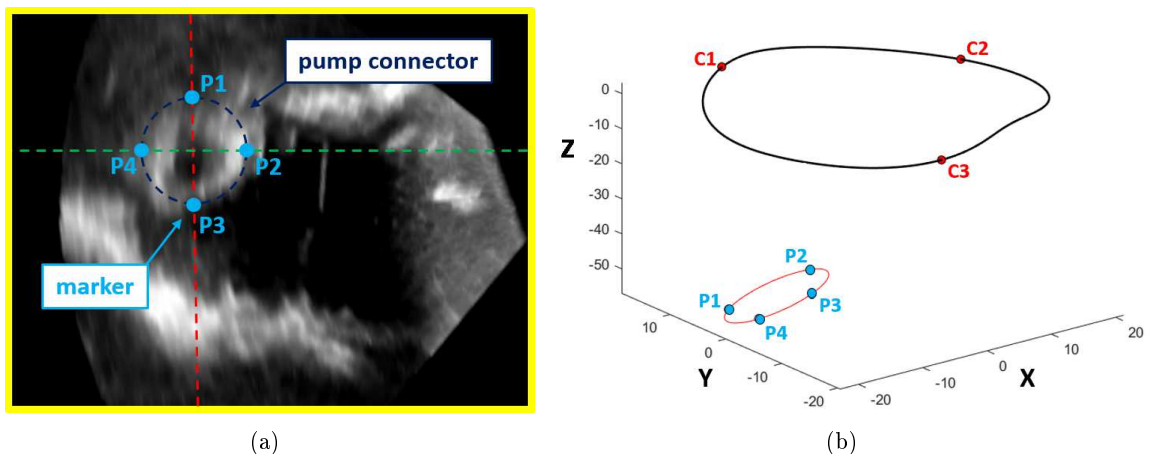
Figure 3.18: Identification of the reference area: (a) positioning of 4 markers in a long-axis plane to trace the pump connector; (b) points of the pump connector located in the coordinate reference system of the TV reconstructed annulus

The projection of the connector on the short-axis plane was used to find the septal leaflet on the annulus. Consequently, the other two leaflets were identified, so to assign at each commissural point the equivalent anatomical one (Figure 3.19).
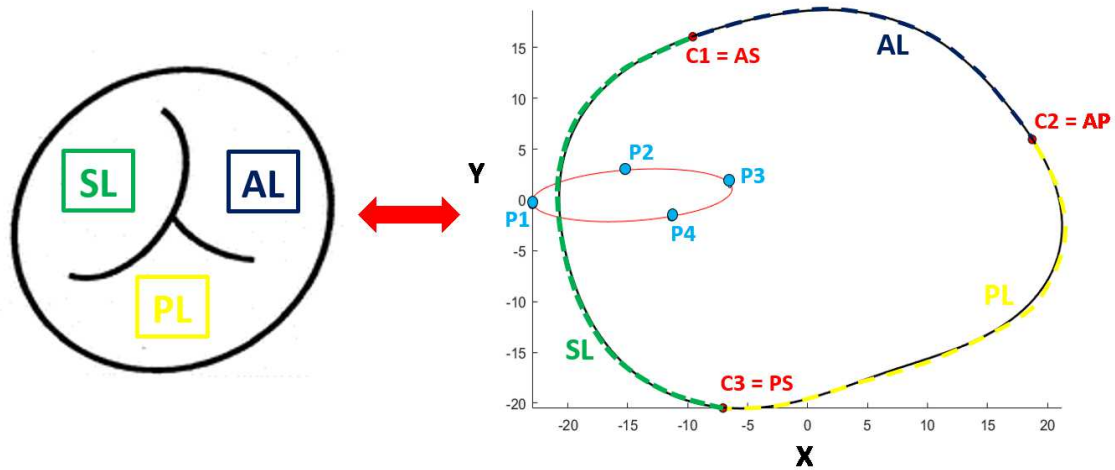
Figure 3.19: Commissures identification. Left: scheme of the TV (SL=septal leaflet; AL=anterior leaflet; PL=posterior leaflet); right: definition of the three anatomical commissures taking the SL as the reference area.

3.6 Sub-valvular apparatus

3.6.1 Papillary muscles

Although the RV was clearly displayed, the identification of the papillary muscles (PMs) on the acquired images resulted very difficult. Therefore, the PMs were placed in agreement with the sonomicrometric data reported by Hiro et al [41] on ovine TVs. In this study, the annulus was reconstructed by means of six ultrasonic crystals placed at the commissures and at the midpoints of the base of each leaflets, while the position of the PMs was detected from three crystals placed in the right ventricle. The three dimensional coordinates of the crystals were provided with respect to a reference system set in the centre of mass of the annular points with the x-axis passing through the PS-crystal (Figure 3.20). To position the PMs in our models, the same reference system described by Hiro et al. was considered and the PMs were placed consistently with the ventricular crystals. Since the position of PMs found in the study was referred to ovine TVs, the ratio between the average perimeter of these valves and the one of our reconstructed TVs was used as scale factor, to take into account possible interspecies morphological differences. In ABAQUS, the PMs were modelled as single nodes, neglecting the presence of multiple heads in the same PM.
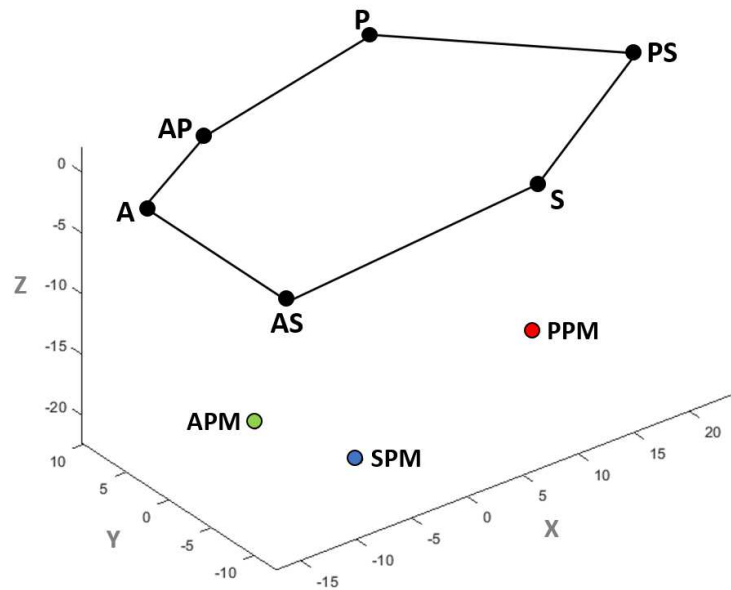
Figure 3.20: Reconstruction of the TV ovine annulus and PMs obtained by Hiro et al. A=base midpoint of the anterior leaflet; P=base midpoint of the posterior leaflet; S=base midpoint of the septal leaflet; AP=antero-posterior commissure; AS=antero-septal commissure; PS=postero-septal commissure; APM=anterior papillary muscle; PPM=posterior papillary muscle; SPM=septal papillary muscle.

3.6.2 Chordae tendineae

Chordae tendineae were modelled following the anatomical classification provided in Section 1.2.3, considering commissural, rough and basal chordae departing from each PM.

Since no solid information about chordae tendineae of the TV is available in literature, the corresponding branched structure, the origin from PMs and insertion sites on the leaflets were defined in this thesis in accordance to *ex vivo* findings provided by Stevanella et al [40] and to the anatomical description presented by Silver et al [12]. The resulting pattern of chordae for one PM is depicted in Figure 3.21.

The chordae were discretized into truss elements to make their resistance to axial compressive loads negligible. A constant cross-sectional area of 0.171 mm^2 was hypothesized, based on experimental measurements performed on human chordae tendineae by Lim et al [22].
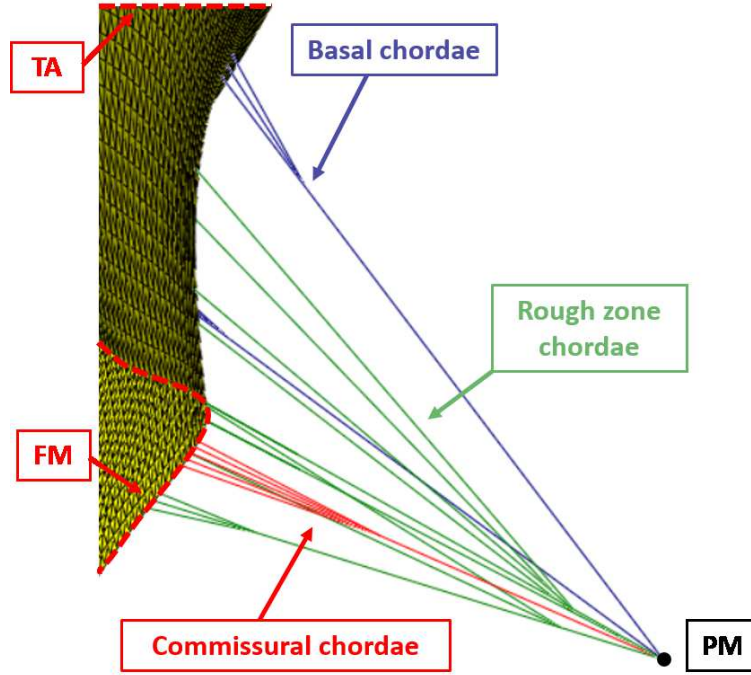
Figure 3.21: Pattern of the chordae tendineae defined in this thesis for each papillary muscle (PM), comprising commissural, rough and basal chordae (TA=tricuspid annulus; FM=free-margin).

3.7 Mechanical properties

The mechanical behaviour of leaflets and chordae tendineae was assumed hyperelastic and described through large deformation theory. The density of all tissues was assumed equal to 1 g/cm^3.

3.7.1 Valve leaflets

In this work, the mechanical properties of TV leaflets were described through the model proposed by Lee et al [44], with the following invariant-based strain energy function Ψ:

$$\Psi = c_0(I_1 - 3) + c_1[(1 - \beta)e^{c_2(I_1-3)^2} + \beta e^{c_3(I_4-3)^2} - 1], \tag{3.3}$$

where $I_1 = trace(\mathbf{C})$, $I_4 = \mathbf{N} \cdot \mathbf{C} \cdot \mathbf{N}$ are respectively the first and fourth invariants of the Cauchy-Green strain tensor $\mathbf{C}$ and $\mathbf{N}$ is the direction of the fibres in the unloaded configuration, assumed circumferentially oriented, according to the cylindrical reference system described in Section 3.3. The constitutive parameters of the model are c_0, c_1, c_2, c_3, β. In particular, β is related to the level of material anisotropy, with $\beta \in [0, 1]$. The two exponential terms in (3.3) account for the responses of the isotropic matrix and collagen fibres respectively.

To identify the constitutive parameters of the model (3.3), the experimental data acquired by Pham et al. [19] from equibiaxial testing on human tricuspid valve leaflets were considered, owing to the reasons discussed in Section 1.2.2. Homogeneous mechanical properties were assumed for the three leaflets. The experimental stress-strain curve, obtained from the average biaxial tensile testing response of each TV leaflet, was fitted by the analytical solution of the equi-biaxial loading condition yielded by the Lee strain energy function (Figure 3.22). The parameters of the model were identified using the Solver tool in Excel to minimize the mean square error between experimental and analytical data (Table 3.1).
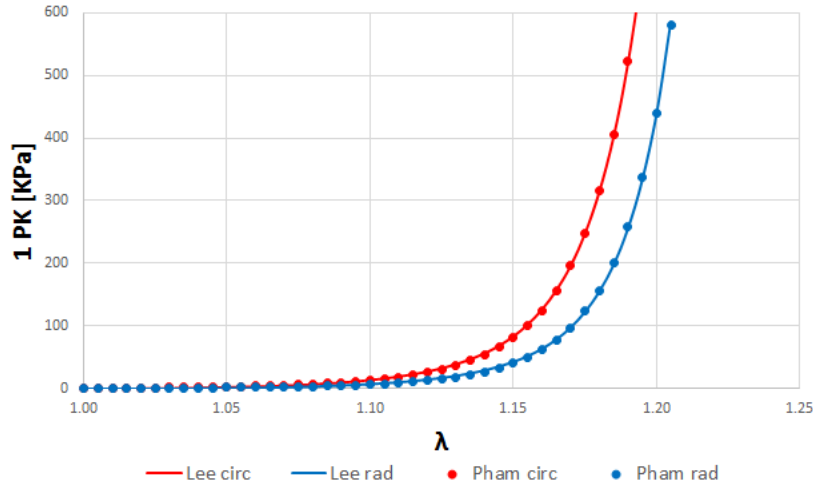
Figure 3.22: Experimental data (dots) from Pham in radial (rad) and circumferential (circ) direction, fitted with Lee model (continuos line).

c_0 [MPa]	c_1 [MPa]	c_2	c_3	β
0.0004	0.0017	19.14	22.79	0.06

Table 3.1: Values of the identified parameters of Lee model.

The constitutive relation (3.3) was implemented in a user-defined VUMAT subroutine within ABAQUS/Explicit, in which the derivatives of Ψ with respect to the invariants are evaluated and the components of the Cauchy stress tensor are returned as output.

Preliminary studies

In order to evaluate the effect of the new material response described in Section 3.7.1, the model proposed by Stevanella was exactly reproduced, in terms of geometry of the valve and subvalvular apparatus, but implementing the Lee constitutive relation for the leaflets (3.3) from Pham data with the material parameters reported in Table 3.1.

The results were compared to those from original model in literature, as described in Table 3.2. The two mechanical behaviours were simulated with the same applied load and boundary conditions to annulus and PMs.

	Stevanella, 2010	Thesis
Strain Energy Function	May-Newman	Lee
Experimental data	Mitral valve	Tricuspid valve

Table 3.2: Comparison of the leaflets mechanical properties implemented by Stevanella and in this thesis.

Considering the numerical results obtained for the two models, the most remarkable differences were observed for the radial deformations. Peak leaflet radial deformations were close to 50% in the model published by Stevanella, and about 30% in our model, whose behaviour was hence considered more reliable. Since no other components of the model proposed by Stevanella were changed to perform this preliminary study, the differences in the mechanical behaviour obtained from the simulations are due to the different material properties implemented for the leaflets. In particular, in the constitutive relation proposed by Lee, the β parameter plays a key role in modulating the stiffness of the material along the cross-fibre direction, while in the strain energy function defined by May-Newman none of the material parameters directly controls the response of the tissue in cross-fibre direction. For this reason, the mechanical response resulting from the May-Newman model is intrinsically more compliant in radial direction, leading to high values of deformation which are likely not physiologic, as already reported in Chapter 2. All these considerations justify the choice of implementing in this thesis the strain energy function proposed by Lee to model the mechanical response of the leaflets.

In order to evaluate the influence of the β parameter on the material behaviour, several fitting were performed on Pham data, constraining β to a different value in the range [0,1] for each fitting. A strip biaxial test was then analytically performed on a patch of the leaflets for each set of material parameters identified, in both radial and circumferential directions.

The stress-strain curves obtained for the radial direction showed a more compliant behaviour increasing the value of β, while quite the opposite trend was found for the circumferential direction. To verify if this behaviour is preserved also in the model, the biomechanical response of the TV was simulated using the Stevanella model for each set of material parameters. Differently from the results of the strip biaxial, no remarkable differences were found in the leaflets behaviour in radial and circumferential directions varying β. For this reason, to simulate the leaflets biomechanics, in this thesis we chose the material parameters already reported

in Table 3.1, deriving from the best fitting, evaluated considering the minimum square error between the constitutive model and the experimental data.

3.7.2   Papillary muscles and chordae tendineae

In this work, papillary muscles were modelled as nodes without physical properties.

The mechanical response of chordae tendineae was assumed non linear isotropic and was modelled through a second order polynomial function available in the ABAQUS material library, described in Appendix A. The constitutive parameters were identified by fitting the experimental data on human chordae obtained by Lim, presented in Section 1.2.3. A lower state of stress was considered for the basal chordae, keeping the same deformation, based on the results for the mitral valve obtained by Jimenez et al [45], who found larger tension acting on marginal chordae as compared to basal ones.

3.8   Boundary conditions and interactions

3.8.1   External loads

A time-dependent physiologic transvalvular pressure curve (Figure 3.23), measured during the experimental tests on the MCL, was applied to the ventricular surface of valve leaflets until the systolic peak (SP), when the pressure difference was equal to 31.1 mmHg.
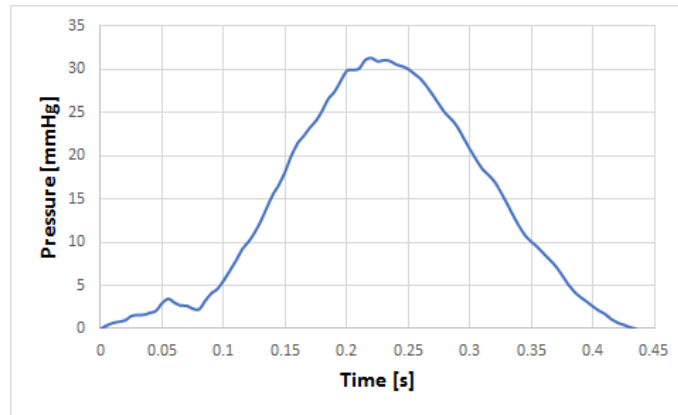
Figure 3.23: Experimental transvalvular pressure curve

3.8.2   Kinematic boundary conditions

Annular contraction was modelled by means of nodal displacements applied to the nodes belonging to the annulus, moving from ED to SP frame. To this aim two annular points were traced on each plane and in each frame of interest and the new profiles were obtained using

the same sampling of ED annulus, to have a one-to-one correspondence between the nodes (Figure 3.24).
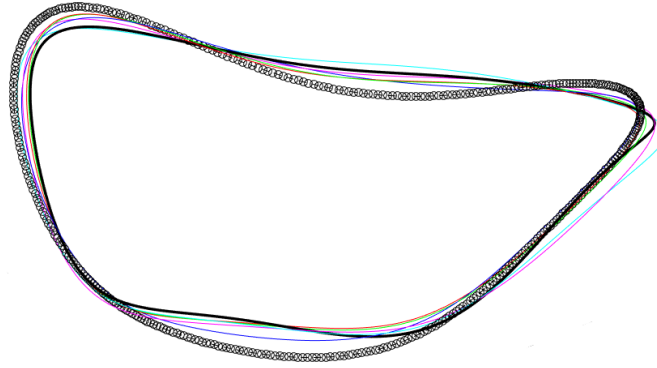
Figure 3.24: Reconstructed annular profiles from ED (dotted black line) to SP frame (continuous black line)

All the reconstructed profiles were translated and rotated with respect to the centre of mass of the ED annulus. Owing to the fact that there is no anatomical reference area in the images, the rotations were performed defining a fixed external point, next to the ED annulus. In this way, changes in annular shape were accounted for, without considering rigid motions and do-nothing use strains no stresses. On the other hand, the use of the fixed external point prevented from identifying a nodal deformation due to twisting.

Papillary muscles motion was neglected.

3.8.3 Leaflets coaptation

Leaflets coaptation was modelled using a general contact algorithm, available in ABAQUS/Explicit, with scale penalty method. The friction coefficient between the leaflets was assumed equal to 0.05 [40].

3.9 3DE-based measurements of the TV morphology and annular dynamics

The four TV reconstructed geometries were analysed to describe the valve morphology and the annular dynamics. All the variables measured on the excised valves (Section 3.2) were evaluated also on the 3DE-based TV, to assess the possible effects of the approximations introduced by the reconstruction procedure. Moreover, since the annular profile was traced in each frame from ED to SP, the temporal evolution of TV annulus (TA), was estimated.

For every reconstructed TAs the following measurements were calculated:

- the 3D area;

- the 2D area, as the TA area projected on the x-y plane;

- TA perimeter.

3.10   Analysis of the sensitivity to the interobserver variability

3.10.1   Manual tracing and TV reconstruction procedure

The repeatability of the TV modelling procedure was assessed by focusing on both manual tracing and automated reconstruction. Accordingly, two independent observers traced TV substructures on the four echocardiographic data sets and the corresponding TV model was then reconstructed.

As regards manual tracing, the Cartesian coordinates obtained from the tracings of the two observers were compared for one of the four studied valves, depicting a nonparametric Bland-Altman plot of the differences vs mean values of the two results. The average bias was evaluated as the median of the differences, and the limits of agreement using the 5th and 95th percentiles.

Concerning the interobserver variability of the automated reconstruction, the meshes obtained from the tracings of the two operators (mesh 1 and mesh 2) were compared for each of the four valves. For each node of mesh 1, the distance from the triangulated surface defined by mesh 2 was evaluated and the minimum value was considered to describe the mesh mismatch between the two operators. The obtained distances for the four valves were analysed through descriptive statistics and colour maps.

3.10.2   Commissures identification procedure

As explained in Section 3.4, we implemented two strategies to find the three commissures and to position them on the reconstructed annular profile, that are the analytical method and the direct segmentation.

The interobserver variability of both procedures was estimated. For the four studied valves, two independent observers (Operator 1 and Operator 2) applied both methods and the resulting three inter-commissural angular distances were identified. In particular, the differences were estimated through the percentage differences of the second observer's results with respect to the corresponding ones of the first observer.

Chapter 4

Results and discussions

4.1 Comparison between direct and 3DE-based measurements of the TV geometry

All the measurements performed on the four excised tricuspid valves were compared with the 3DE-based values, deriving from the geometrical reconstruction procedure explained in Section 3.3. In particular, the percentage differences of the 3DE-based measurements with respect to the direct ones were evaluated. The results are reported in Table 4.1.

The 3DE-based annular perimeter differs from the direct one by 1 to 15 mm (percentage difference from -0.6% to -9.2%); the leaflet lengths mismatches vary from 2 to 32 mm (percentage difference from -6.6% to -43.8%); the leaflet heights variations are from 1 to 11 mm (percentage difference from 3.3% to 64.7%); the differences in commissural heights range between 6 and 22 mm (percentage difference from 66.7% to 314.3%).

These results show that the 3DE-based measurements of the annular perimeter and leaflets lengths are not notably affected by the approximations introduced with the TV reconstruction process. On the contrary, the leaflets and commissural heights considerably exceed the direct measurements.

The overestimation is probably due to the following reasons:

- the free-edge portions of the leaflets are not as clearly visible as the annulus in 3DE images, therefore the resulting measurements are strongly affected by the manual tracing's procedure;

- the VolDICOM datum was sampled in 18 equally spaced radial planes, hence the actual position of the commissures could be between two sampled points;

Variable [mm]		TV 1	TV 2	TV 3	TV 4
Perimeter	direct	145	164	155	140
	3DE-based	153 (+5.5%)	149 (-9.2%)	154 (-0.6%)	129 (-7.6%)
AL length	direct	34	55	50	45
	3DE-based	63 (+85.3%)	59 (+7.9%)	38 (-24.0%)	49 (+8.5%)
PL length	direct	38	45	47	37
	3DE-based	50 (+31.6%)	37 (-17.2%)	66 (+40.4%)	35 (-6.6%)
SL length	direct	73	75	55	57
	3DE-based	41 (-43.8%)	52 (-30.3%)	49 (-10.9%)	46 (-19.3%)
AL height	direct	26	23	22	14
	3DE-based	29 (+11.5%)	19 (-16.9%)	24 (+9.1%)	18 (+31.5%)
PL height	direct	14	25	17	12
	3DE-based	20 (+42.9%)	22 (-11.7%)	28 (+64.7%)	18 (+46.8%)
SL height	direct	28	25	18	11
	3DE-based	21 (-25.0%)	26 (+3.3%)	20 (+8.8%)	19 (+73.9%)
AS-c height	direct	7	7	7	4
	3DE-based	29 (+314.3%)	25 (+250.5%)	27 (+281.4%)	21 (+419.4%)
PS-c height	direct	9	8	10	4
	3DE-based	15 (+66.7%)	24 (+206.1%)	23 (+128.4%)	16 (+306.2%)
AP-c height	direct	9	7	10	5
	3DE-based	20 (+122.2%)	23 (+225.3%)	27 (+168.7%)	21 (+327.2%)

Table 4.1: Comparison between direct and 3DE-based measurements of the TV geometry. The magnitude of the percentage differences is reported in brackets. Abbreviations: TV, tricuspid valve; 3DE, three-dimensional echocardiography; AL, anterior leaflet; PL, posterior leaflet; SL, septal leaflet; AS-c, antero-septal commissural; PS-c, postero-septal commissural; AP-c, antero-posterior commissural.

- even if the three commissural portions were visible on the radial planes, the reconstructed TV leaflets were derived from approximations with 4th order Fourier functions, that tone down local steep changes in leaflet height.

4.2 Annular dynamics evaluation

The time-dependency of the extent of the TV orifice is depicted in Figure 4.1 for each TV studied.

Three of the four valves show the same pattern: the tricuspid annulus (TA) get larger during the cardiac cycle phases analysed, namely from end-diastole (ED) to systolic peak (SP). For one valve (TV1) the behaviour is different, showing an irregular trend, probably due to the lower frame rate of the acquired image (i.e., 18 frames/cycle for TV1 and 33 frames/cycle for the other 3 valves), that results in a lower sampling frequency. Therefore, the frame identified on the image as SP could actually correspond to a next phase of the cardiac cycle, when the transvalvular pressure is lower and the orifice area shrinks.
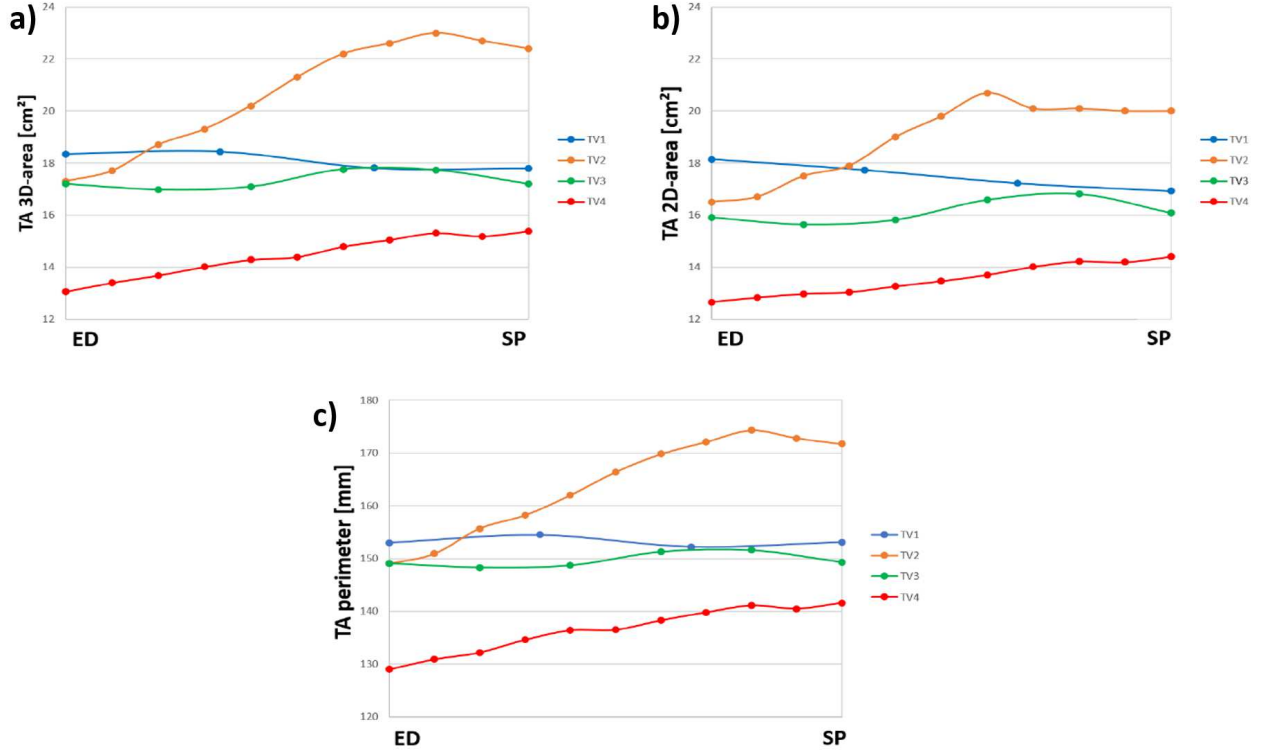
Figure 4.1: Temporal evolution of TA position during the traced cardiac cycle phases, from end-diastole (ED) to systolic peak (SP): a-b) changes in annular 3D and projected 2D areas; c) changes in TA perimeter.

The extent in TA from ED to SP is in contrast with what was reported in literature [9] but it is consisted with the experimental set-up: the heart housed on the MCL is passive and lacks of the in vivo muscle contraction. Indeed, the pumping system induces paradoxical motion of the right ventricle, that results in the ventricular volume increase during systole, and decrease in diastole [35].

4.3   Analysis of the sensitivity to the interobserver variability

4.3.1   Manual tracing and TV reconstruction procedure

The results of nonparametric Bland-Altman analyses, performed to quantify the interobserver mismatch between the position of the traced points are summarized in Figure 4.2.

The plots show a comparable interobserver level of agreement for the manual tracings of the annulus (Figure 4.2 a) and the leaflets (Figure 4.2 c). Biases and the amplitudes of the 90% limit of agreement are, respectively, 0.15 mm and 5.86 mm for the annulus, and 0.65 mm and 5.94 mm for the leaflets. A higher variability emerges for the tracing of the TV free-edge
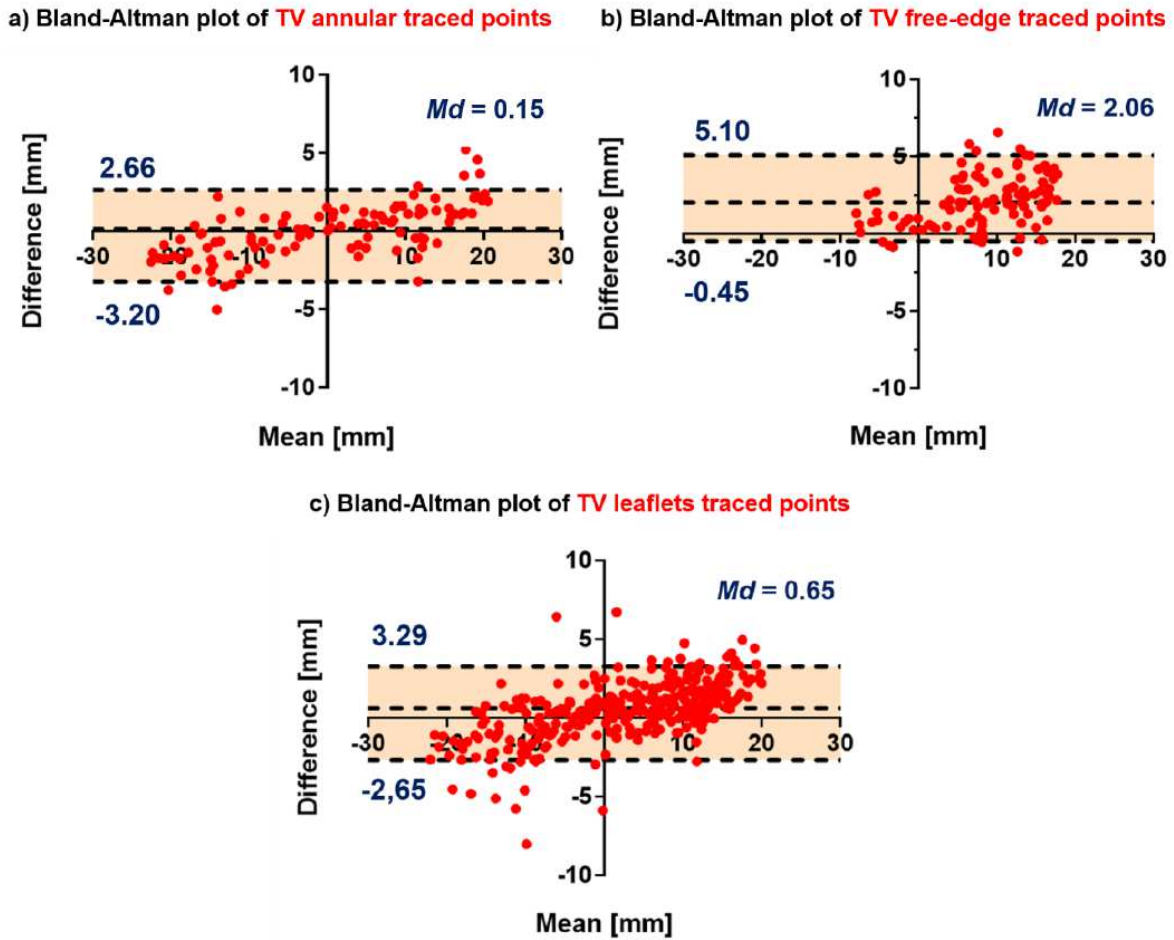
Figure 4.2: Bland-Altman plots comparing the results of manual tracings of TV annulus (a), free-edge (b) and leaflets (c) obtained by two independent observers. Horizontal dotted lines indicate the limits of agreement; Md = median, is reported as measure of bias.

(Figure 4.2 b), with median difference of 2.06 mm and 90% limit of agreement range of 5.55 mm. These results are consistent with the fact that free-edge portions of the leaflets are not as clearly visible as the annulus in 3DE images.

Concerning the interobserver variability of the automated reconstruction, the distributions of the mesh mismatch for each valve were analysed through histograms (Figure 4.3) and the results of the descriptive statistics are reported in Table 4.2.

The median values of the mismatch are quite consistent for all the valves, ranging from 1.11 to 2.30 mm. As shown in Figure 4.3, the mismatch distributions have a single tail, with the largest percentage of occurrences located below 4 mm, given that the points were sampled with a mean spatial resolution of 0.366 mm. The minimum distances tend to zero, while the maximum distances vary from 4.70 to 9.77 mm. This variability can be explained considering
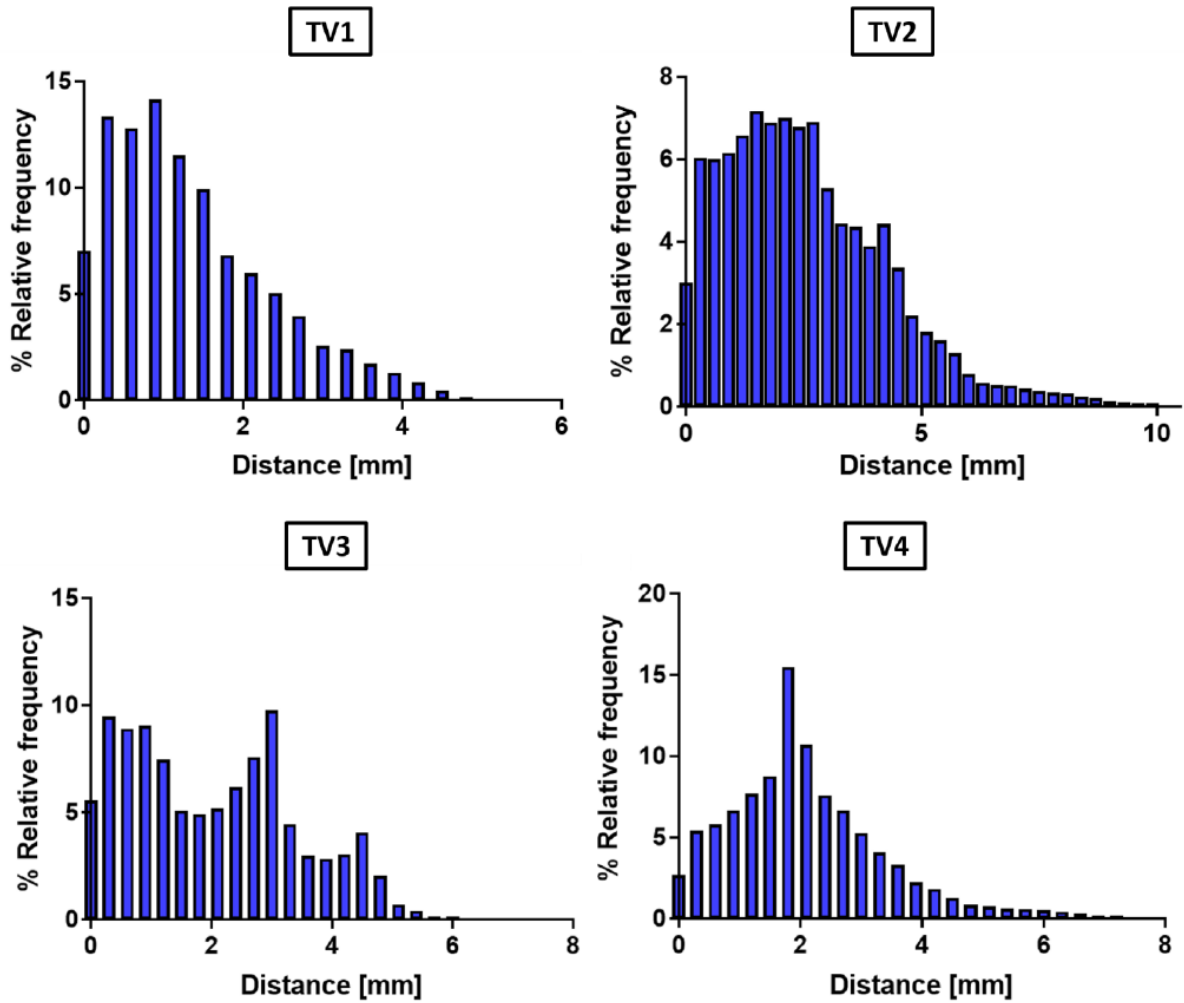
Figure 4.3: Histograms of the distribution of the interobserver mesh mismatch for the four valves analysed. Class width=0.3 mm. The occurrences in each class are evaluated as relative frequency percentage.

	Median	Min	Max	25th p	75th p
TV1	1.11	3e-05	4.70	0.56	1.92
TV2	2.30	4e-05	9.77	1.22	3.63
TV3	1.92	2e-05	5.86	0.79	3.00
TV4	1.89	4e-05	6.96	1.21	2.73

Table 4.2: Analysis of the distribution of the mesh mismatch between the two operators. The median, maximum and minimum value, 25th and 75th percentiles were evaluated. All the values are expressed in mm

the quality of the echocardiographic acquisitions from which the four valves were reconstructed. In particular, for valve TV2 the presence of residual artefacts may have induced an erroneous

identification of the annulus and free margin in some radial planes, resulting in a higher interobserver mesh mismatch compared to the other valves.

The spatial distribution of the mismatch in each valve was displayed through colour maps (Figure 4.4). The highest mismatch was generally found at FM, consistently with the fact that the latter is less visible than the other parts of the valve from the acquired images. Indeed, the positioning of the traced points at the TV free-margin is particularly dependent on a skilled operator.
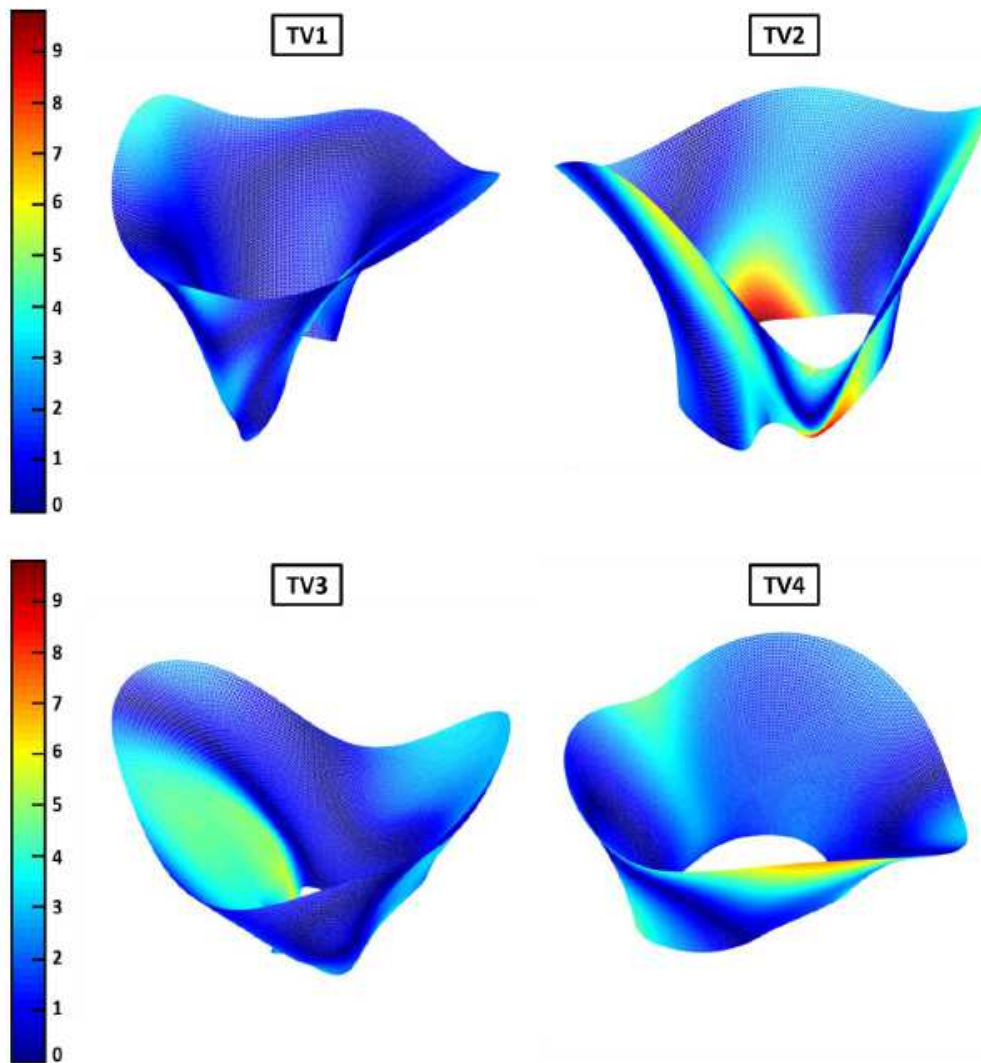

Figure 4.4: Colour maps showing the spatial distribution of the mesh mismatch for the four valves analysed. Values in the colorbar are reported in mm.

4.3.2 Commissures identification procedure

The following tables summarize the results of the analysis of the interobserver variability of the two strategies implemented to find the three commissures and to position them on the reconstructed annular profile: the "analytical" method (Table 4.3) and the direct segmentation (Table 4.4).

The analytical-based angular distances obtained by Operator 2 differ from the ones of Operator 1 by 0.17 to 41.50 degrees (percentage difference from 0.2% to 31.5%), while the interobserver mismatch associated to the direct segmentation procedure ranges between 1.07 and 27 degrees (percentage difference from -0.8% to 33.4%).

These results are in accordance with the fact that the analytical method is strongly connected with the 3D-reconstruction procedure: since the three angular positions were derived evaluating the three minimum leaflets lengths, the values obtained are affected by all the approximations discussed in Section 4.1. A lower variability emerges for the direct segmentation method, only depending on the quality of the acquired images and on the skills of the operator. Hence, the simulations of the valve closure were performed dividing the three leaflets in accordance to the angular distances obtained with the direct segmentation.

Analytical method		Operator 1	Operator 2
PS-AS angular distance [deg]	TV 1	90.23	90.40 (+0.2%)
	TV 2	120	149.78 (+24.8%)
	TV 3	131.73	90.23 (-31.5%)
	TV 4	103.76	94.74 (-8.7%)
AS-AP angular distance [deg]	TV 1	166.02	135.34 (-18.5%)
	TV 2	90.24	101.05 (+12.0%)
	TV 3	88.42	125.41 (+41.8%)
	TV 4	110.08	150.68 (+36.9%)
AP-PS angular distance [deg]	TV 1	103.64	134.44 (+29.4%)
	TV 2	149.76	109.17 (-27.1%)
	TV 3	139.85	144.36 (+3.2%)
	TV 4	146.17	114.59 (-21.6%)

Table 4.3: Comparison between the commissural angular distances obtained by two independent operators, performing the analytical method for each TV. The magnitude of the percentage differences is reported in brackets. Abbreviations: PS, postero-septal; AS, antero-septal; AP, antero-posterior.

4.3.3 Simulation of valve closure

The biomechanical behaviour of the four analysed valves was simulated from ED to SP. The results show a non complete coaptation of the leaflets, that was quantified as the percentage ratio between the regurgitant area at SP and the orifice area, i.e., the annulaer area, at ED

Direct segmentation		Operator 1	Operator 2
PS-AS angular distance [deg]	TV 1	94.05	95.80 (+1.9%)
	TV 2	126.21	125.15 (-0.8%)
	TV 3	110.46	127.21 (+15.2%)
	TV 4	127.51	111.30 (-12.7%)
AS-AP angular distance [deg]	TV 1	132.26	143.40 (+8.4%)
	TV 2	152.87	126.93 (-17.0%)
	TV 3	97.06	94.47 (-2.7%)
	TV 4	129.55	133.92 (+3.4%)
AP-PS angular distance [deg]	TV 1	133.69	120.81 (-9.6%)
	TV 2	80.92	107.92 (+33.4%)
	TV 3	152.48	138.32 (-9.3%)
	TV 4	102.94	114.8 (+11.5%)

Table 4.4: Comparison between the commissural angular distances obtained by two independent operators, performing the direct segmentation method for each TV. The magnitude of the percentage differences is reported in brackets. Abbreviations: PS, postero-septal; AS, antero-septal; AP, antero-posterior.

(Table 4.5). Such percentage ratio ranges from 0.89% to 2.41%, thus indicating the rather small extent of the residual regurgitant area.

	Orifice area ratio [%]
TV1	1.87
TV2	2.04
TV3	0.89
TV4	2.41

Table 4.5: Percentage ratio of the orefice area at SP with respect to the one evaluated at ED for the four valves simulated.

The analyses of leaflets motion throughout transient closure, of the strain distribution over the leaflets and of leaflet stresses suggested that the incomplete coaptation of the leaflets is likely due to an excessive tethering effect exerted by the chordae tendineae, owing to the shape of the leaflets free margin next to chordal insertions. Indeed, ideally the chordae tendineae should insert at the three commissural regions, which should be characterized by the three indentations that separate the profile of the three leaflets of the valve. Instead, in the modeled anatomies free margin indentations are not located at the commissures: at least one of them looks "out of place" (Figure 4.5). The consequence, in terms of leaflet geometry and distribution of chrdal insertions over the free margin, is that the radial extent of the corresponding

leaflet is i) too wide in the commissural region, and the chordae tendineae therein inserted are hence shorter than expected, and ii) too short in the adjacent tract, which is free from chordal insertions. In terms of leaflet motion, this effect results in a tethering effect exerted by excessively short, and hence excessively stiff, chordae tendineae on the region of the leaflet that is characterized by a wide surface is tethered, whereas the region of the leaflet characterized by a much smaller surface is free to move, but its small extent prevents from full coaptation.
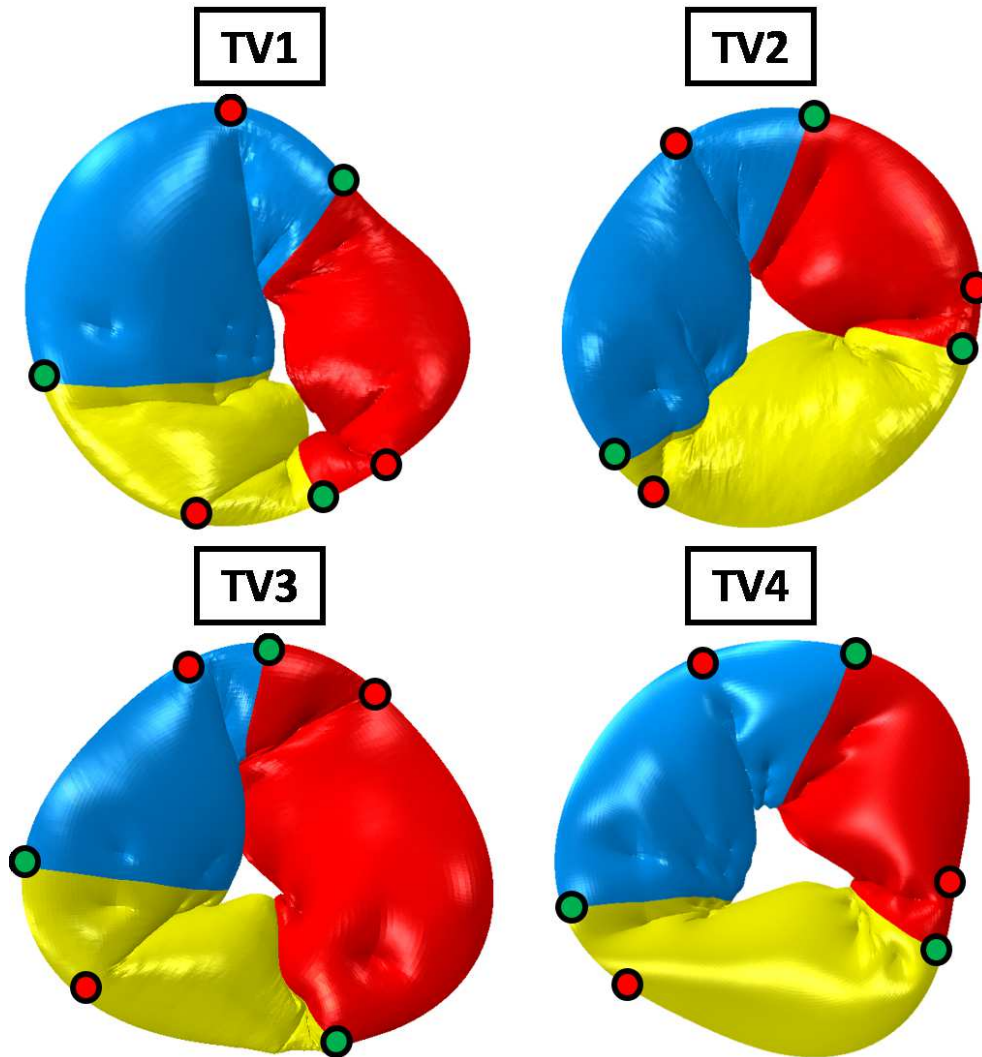
Figure 4.5: Configurations of the four valves simulated, at SP, showing anterior (blue), posterior (red) and septal (yellow) leaflets. The position of the three most prominent indentations (red dots) and the location of the three commissures (green dots) with respect to the valve geometry are depicted.

Two sources of error may be identified in the modelling approach to explain these findings: i) the direct segmentation of the commissures in 3D SLICER; ii) the manual tracing of the leaflets on the radial planes. Since the results of the variability analysis on the direct segmen-

tation (Section 4.3.2) showed a good interobserver agreement, the problem is more likely to be related to the identification of the free-edge portion of the leaflets in the acquired images, as already discussed in Section 4.3.1. Moreover, this negative effect is superimposed to another one: because of the relative position of papillary muscles and chordal insertions, which determines the space orientation of chordae tendineae, in some cases the leaflet is pulled not only donwards and radially outwards, but also circumferentially, thus hampering the effectiveness of leaflet motion in terms of orifice occlusion. An example of this behaviour is depicted, for one of the four valves, in Figure 4.6: the nodal displacement is shown both through colour map of the magnitudes and with arrows indicating the resultant directions of the displacement. Focusing on the orifice area at SP, the movement of one of the three leaflets in the circumferential direction is highlighted (red arrows in Figure 4.6), with respect to the motion of the other two leaflets, towards the orifice.
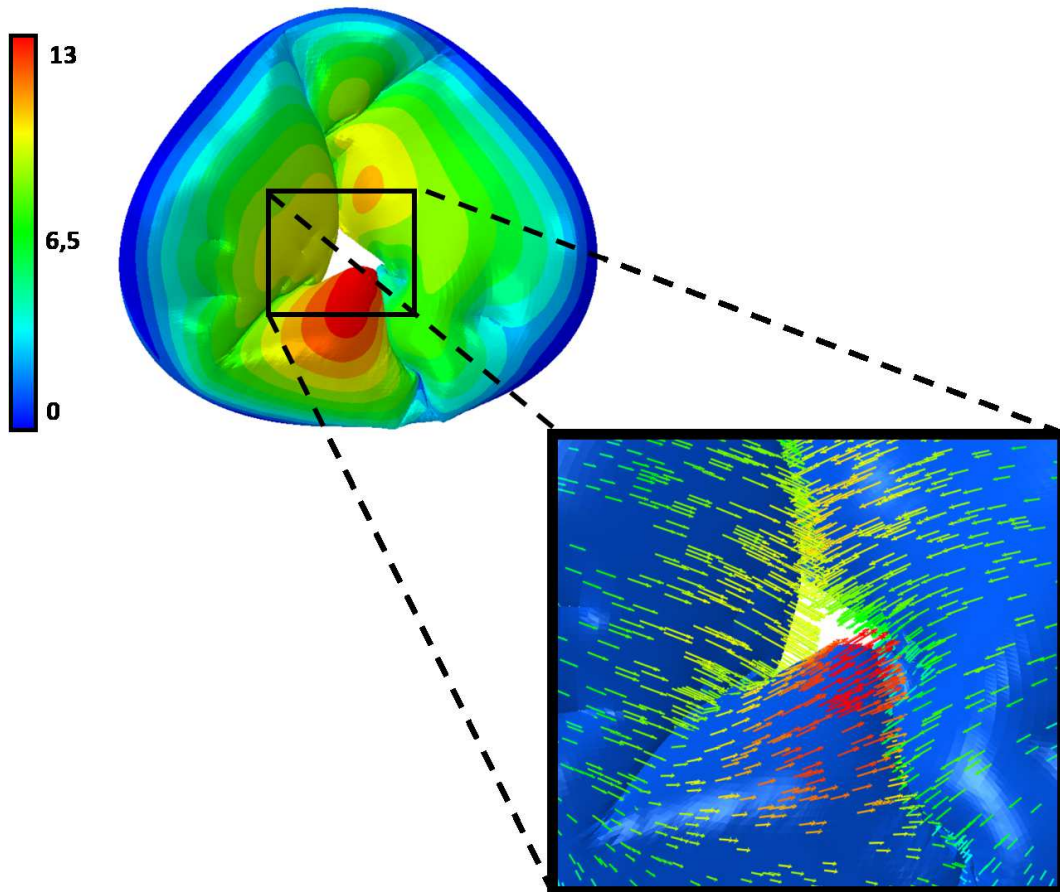

Figure 4.6: Color map of the magnitude of the resultant nodal displacements (top); directions of displacements indicated with arrows (bottom). The values on the colorbar are reported in mm.

This interpretation of the causes of leaflet incomplete coaptation is further supported by the analysis of space distribution of the radial strains over the leaflets (Figure 4.7) and the maximum principal in-plane stress field (Figure 4.8).
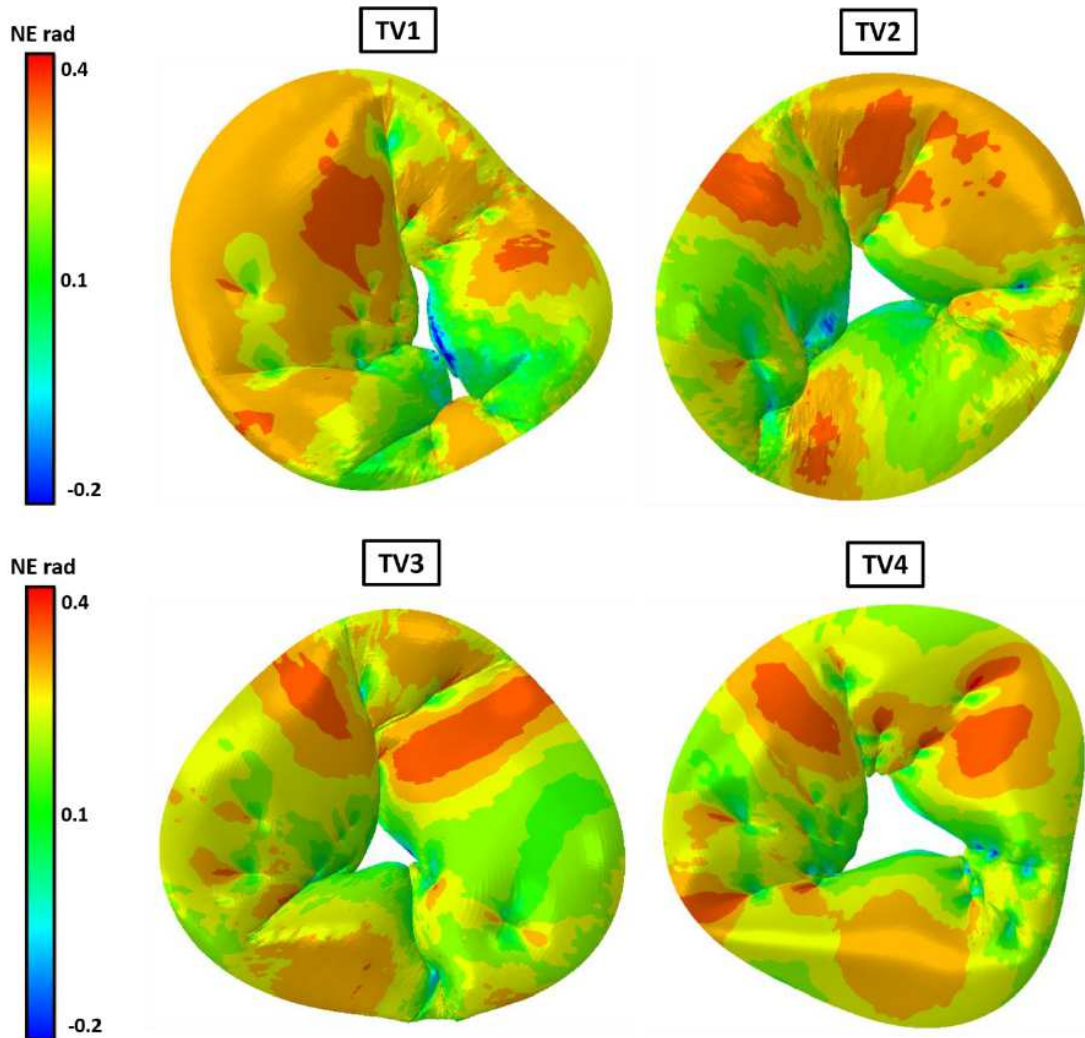
Figure 4.7: Radial nominal strain distributions at SP for the four valves simulated.

The distribution of the radial strains is similar in all models the models: peak nominal strain values are smaller than 40% and are located next to the chordal insertions, indicating that the tethering effect induced by chordae tendineae, and the associated hypomobility of the leaflet free margin, induce a radial strain of leaflet tissue under the effect of the pressure load acting on them. This behaviour is preserved in the stress fields, in which the peak values are observed at the chordal insertions, in agreement with the location of the radial strain peaks. Of note, the described features are likely exacerbated by the combination of applied kinematic boundary conditions: enlargement of the annulus from ED to SP due to the paradoxical movement

Figure 4.8: Maximum in-plane principal stress fields at SP for the four valves simulated.

induced by the MCL (Section 4.2), which was accounted for in the simulations to reproduce the in vitro conditions, and fixed position of the papillary muscles throughout the simulation, whose in vitro movement was neglected.
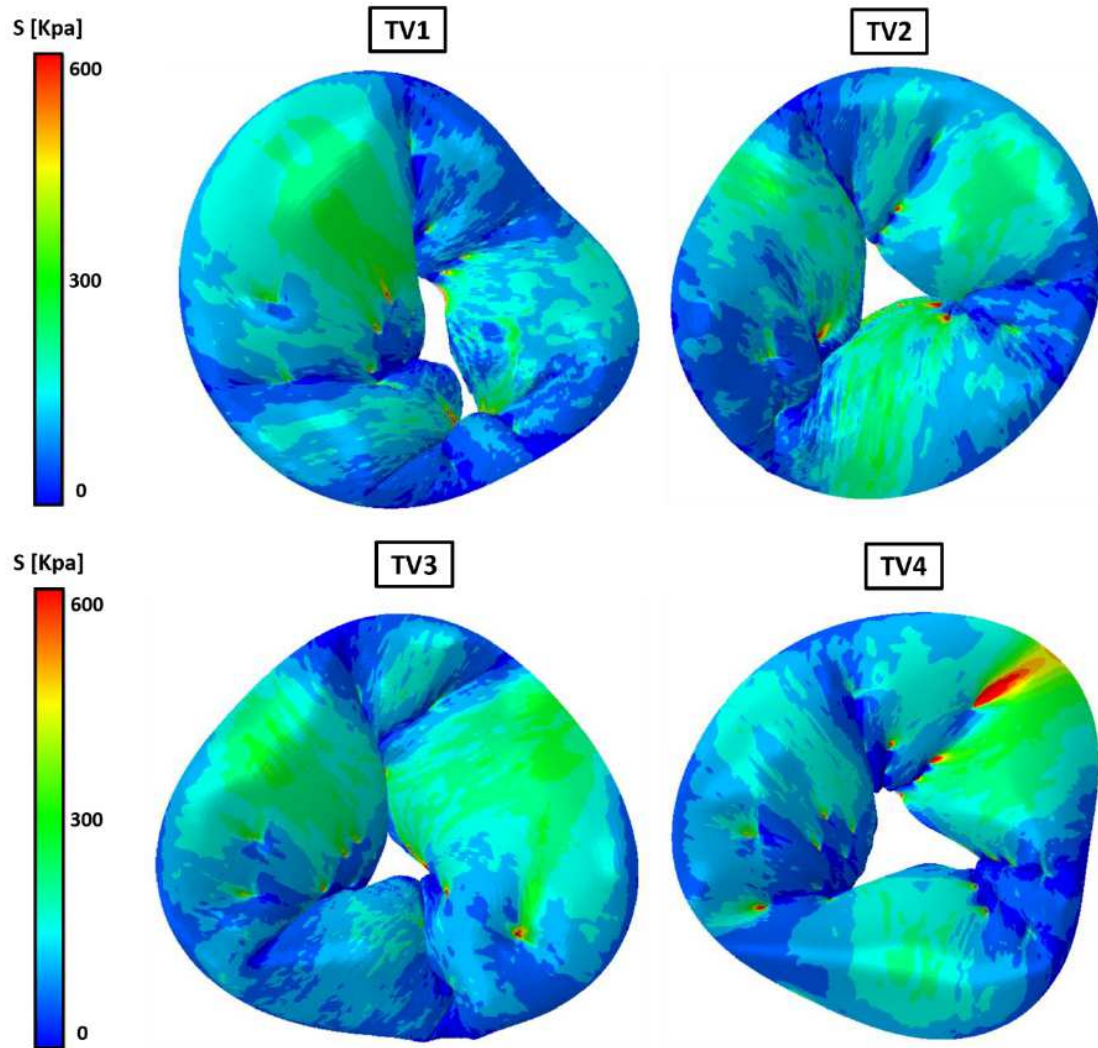
Chapter 5

Conclusions and future developments

In this thesis we presented a novel approach for the study of the tricuspid valve (TV) biomechanics, integrating experimental in vitro data and computational elaborations towards the development of the first image-based complete finite element model (FEM) of the valve. The new designed method would allow to carry out in vitro tests on a right porcine heart housed in a mock circulation loop (MCL) and to perform imaging of the TV structures.

The acquired images are used to reconstruct the leaflets profile at end diastole and to define the time-dependent geometry of the annulus and the motion of the papillary muscles (PMs). Altogether, this information could be taken as input to define the FEM of the valve, implementing material mechanical properties specifically derived for the TV.

Our work showed that the MCL presented in 3.1 was a suitable environment to perform experimental campaigns on the TV, allowing to replicate physiologic-like working conditions of the valve, in terms of pulsatile flow rate, frequency and pressure acting on the system. The acquisition protocol and the computational processing of the echocardiographic images resulted in a reconstructed TV geometry that was globally more accurate as compared to the paradigmatic one defined in the only FEM of the TV currently available in literature [40]. Besides, the experimental measurements performed on the biological samples were used to have a feedback of the reliability of the geometrical model. In particular, the definition of the annular geometry was reliable and repeatable, showing a high level of the interobserver agreement. The reconstruction of the leaflets was achieved, although it was affected by a non negligible interobserver variability, due to the difficulties encountered in the segmentation of the free margin. This variability led to uncertainty in the extent of the leaflets along the annulus-free edge direction, in particular at the commisural regions. Moreover, the approximation of the free margin with a Fourier function systematically emphasized this issue, making the annulus-to-free margin extent of the commissural region further too large and resulting in a reconstructed profile with minimal indentations as compared to the natural one.

The final part of our project focused on the simulation of the TV biomechanics, showing that the limitations just described were responsible for the incomplete systolic closure of the valve. Indeed, the error affecting the annulus-free margin extent of the valve profile resulted in a systematic tethering and unexpected motion of the leaflets, reducing their mobility and hampering coaptation.

In terms of future developments of this project, the focus should hence be on solving the issues related to the uncertainty in the manual tracing of the laflets, and more specifically in the identification of the leaflet free margin, in particular at the commissural regions. To this end, a possible solution may be to perform the segmentation of the valve in the radial planes after the identification of the commissures, so to take advantage of the priori information on the commissural position to guide the segmentation of the leaflets, namely, for example, by setting a flag on the image planes adjacent to a commissure. This could be a simple, but effective method to enhance the accuracy of the segmentation.

The quality of the image acquisition process may be further improved, so to allow for the identification of the papillary muscles, that were not easily detected on the images acquired in this thesis.

Finally, the number and the pattern of the chordae tendineae set in our models is likely to be reviewed, since it leaves the central portion of the leaflets completely free from chordal insertions; as a result, the central tract of each leaflet is allowed for potentially uncontrolled motion. To this aim, a detailed experimental analysis of the TV subvalvular apparatus needs to be performed.

Appendix A

Polynomial strain energy potential in Abaqus/Explicit

The mechanical behaviour of a hyperelastic material is described through the strain energy potential, representing the strain energy per unit volume stored in he material during the deformation process. In the Abaqus/Explicit library, different forms of the strain energy potential are available. In this thesis, the following polynomial strain energy function Ψ was used to model the biomechanics of the chordae tendineae:

$$\Psi = \sum_{i+j=1}^{N} C_{ij}(\overline{I}_1 - 3)^i(\overline{I}_2 - 3)^j + \sum_{i=1}^{N} \frac{1}{D_i}(J^{el} - 1)^{2i}, \tag{A.1}$$

where N is a material parameter, C_{ij} and D_i are temperature-dependent parameters. $\overline{I}_1$ and $\overline{I}_2$ are the first and second deviatoric invariants, defined as

$$\overline{I}_1 = \overline{\lambda}_1^2 + \overline{\lambda}_2^2 + \overline{\lambda}_3^2 \qquad \text{and} \qquad \overline{I}_2 = \overline{\lambda}_1^{(-2)} + \overline{\lambda}_2^{(-2)} + \overline{\lambda}_3^{(-2)},$$

where $\overline{\lambda}_i$ is the deviatoric stretch, expressed as $\overline{\lambda}_i = J^{-\frac{1}{3}}\lambda_i$, with λ_i is the principal stretch and J is the total volume ratio. The parameter J^{el} in Equation A.1 is the elastic volume ratio, which relates the total volume ratio J and the thermal volume ratio J^{th}, as follows:

$$J^{el} = \frac{J}{J^{th}}.$$

J^{th} is given by $J^{th} = (1 + \epsilon^{th})^3$, where ϵ^{th} is the linear thermal expansion strain that is obtained from the temperature and the isotropic thermal expansion coefficient.

In this thesis, the material parameters C_{ij} and D_i are automatically computed by Abaqus from the experimetal data taken from the tensile test on the chordae [22].

Bibliography

[1] Saladin K. *Anatomy and Physiology: The Unity of Form and Function, Third Edition.* 2003.

[2] J.G. Betts, P. Desaix, J.E. Johnson, O. Korol, D. Kruse, B. Poe, J. Wise, M.D. Womble, K.A. Young, OpenStax College, et al. *Anatomy and Physiology.* 2013.

[3] Guyton and Hall. *Textbook of Medical Physiology.*

[4] Barrett K. E., Boitano S., Barman S. M., and Brooks H. L. *Ganong's Review of Medical Physiology.* 2012.

[5] Huttin O., Voilliot D., Mandryb D., Vennera C., Juillière Y., and Selton-Sutya C. All you need to know about the tricuspid valve: Tricuspid valve imaging and tricuspid regurgitation analysis. *Archives of Cardiovascular Disease*, 2016.

[6] Kevin Marron, Magdi H. Yacoub, Julia M. Polak, Mary N. Sheppard, David Fagan, Bruce F. Whitehead, Marc R. de Leval, Robert H. Anderson, and John Wharton. Innervation of human atrioventricular and arterial valves. *Circulation*, 94(3):368–375, 1996.

[7] Robert H. Anderson, Siew Yen Ho, and Anton E. Becker. Anatomy of the human atrioventricular junctions revisited. *The Anatomical Record*, 260(1):81–91, 2000.

[8] Maffesanti F., Gripari P., Pontone G., and Andreini D. Three-dimensional dynamic assessment of tricuspid and mitral annuli using cardiovascular magnetic resonance. *European Heart Journal*, 2013.

[9] Fukuda S., Saracino G., Matsumura Y, Daimon M., Tran H., Greenberg N.L., Hozumi T., Yoshikawa J., Thomas J.D., and Shiota T. Three-dimensional geometry of the tricuspid annulus in healthy subjects and in patients with functional tricuspid regurgitation. a real-time, 3-dimensional echocardiographic study. *Circulation*, 2006.

[10] Spinner E. M., Buice D., Yap C. H., and Yoganathan A. P. The effects of a three-dimensional, saddle-shaped annulus on anterior and posterior leaflet stretch and regurgitation of the tricuspid valve. *Annals of Biomedical Engineering*, 2012.

[11] Meluzin J, Spinarova L., Bakala J., Toman J., Krejci J, Hude P., Kara T., and Soucek M. Pulsed doppler tissue imaging of the velocity of tricuspid annular systolic motion. a new, rapid, and non-invasive method of evaluating right ventricular systolic function. *European Heart Journal*, 2001.

[12] Silver M. D., Lam J. H. C., Ranganathan N., and Wigle E. D. Morphology of the human tricuspid valve. *Circulation*, 1971.

[13] Seccombe J. F., Cahill D. R., and Edwards W. D. Quantitative morphology of the normal human tricuspid valve: Autopsy study of 24 cases. *Clinical Anatomy*, 1993.

[14] Taramasso M., Vanermen H., Maisano F., Guidotti A., La Canna G., and Alfieri O. The growing clinical importance of secondary tricuspid regurgitation. *Journal of the American College of Cardiology*, 2012.

[15] Stefanie Heyden, Andreas Nagler, Cristóbal Bertoglio, Jonas Biehler, Michael W. Gee, Wolfgang A. Wall, and Michael Ortiz. Material modeling of cardiac valve tissue: Experiments, constitutive analysis and numerical investigation. *Journal of Biomechanics*, 48(16):4287 – 4296, 2015.

[16] Dr Matthews R. J. Cardiology. http://www.rjmatthewsmd.com/Definitions/anatomyoftheheart.htm.

[17] Alavi S. H., Sinha A., Steward E., Milliken J. C., and Kheradvar A. Load-dependent extracellular matrix organization in atrioventricular heart valves: differences and similarities. *Am J Physiol Heart Circ Physiol*, 2015.

[18] Misfeld M. and Sievers H. Heart valve macro- and microstructure. *The Royal Society*, 2007.

[19] Thuy Pham, Fatiesa Sulejmani, Erica Shin, Di Wang, and Wei Sun. Quantification and comparison of the mechanical properties of four human cardiac valves. *Acta Biomaterialia*, 54:345 – 355, 2017.

[20] Nigri G.R., Di Dio L. J. A., and Baptista C.A.C. Papillary muscles and tendinous cords of the right ventricle of the human heart morphological characteristics. *Surgical and Radiologic Anatomy*, 2001.

[21] Saremi F., Hassani C., Millan-Nunez V., and Sánchez-Quintana D. Imaging evaluation of tricuspid valve: Analysis of morphology and function with ct and mri. *American Journal of Roentgenology*, 2015.

[22] Lim K. O. Mechanical properties and utrastructure of normal human tricuspid valve chordae tendineae. *Japanese Journal of Physiology*, 1980.

[23] Chambers J.B., Myerson S.G., and Rajani R. et al. Multimodality imaging in heart valve disease. *Open Heart*, 2016.

[24] Badano L. P., Agricola E., Gianfagna P., and Zamorano J. L. Evaluation of the tricuspid valve morphology and function by transthoracic real-time three-dimensional echocardiography. *European Journal of Echocardiography*, 2009.

[25] Lisa Qia Rong. An update on intraoperative three-dimensional transesophageal echocardiography. *Journal of Thoracic Disease*, 9(Suppl 4):S271–S282, March 2017.

[26] Roberto M. Lang, Luigi P. Badano, Wendy Tsang, David H. Adams, Eustachio Agricola, Thomas Buck, Francesco F. Faletra, Andreas Franke, Judy Hung, Leopoldo Perez de Isla, Otto Kamp, Jaroslaw D. Kasprzak, Patrizio Lancellotti, Thomas H. Marwick, Marti L. McCulloch, Mark J. Monaghan, Petros Nihoyannopoulos, Natesa G. Pandian, Patricia A. Pellikka, Mauro Pepi, David A. Roberson, Stanton K. Shernan, Girish S. Shirali, Lissa Sugeng, Folkert J. Ten Cate, and Mani A. Vannan. Recommendations for image acquisition and display using three-dimensional echocardiography. *Journal of the American Society of Echocardiography*, 2012.

[27] Xie M., Wang X., Cheng T., and Lu Q. Real-time 3-dimensional echocardiography: A review of the development of the technology and its clinical application. *Progress in Cardiovascular Diseases*, 2005.

[28] Leda Galiuto, Luigi Badano, Kevin Fox, Rosa Sicari, and Jose Luis Zamorano. *The EAE Textbook of Echocardiography*. Oxford University Press, 2011.

[29] Maurizio Taramasso, Alberto Pozzoli, Andrea Guidotti, Fabian Nietlispach, Devdas T. Inderbitzin, Stefano Benussi, Ottavio Alfieri, and Francesco Maisano. Percutaneous tricuspid valve therapies: the new frontier. *European Heart Journal*, 38(9):639, 2017.

[30] Tang G. H. L., David T. E., Singh S. H., Maganti M. D., Armstrong S., and Borger M. A. B. Tricuspid valve repair with an annuloplasty ring results in improved long-term outcomes. *Circulation*, 2006.

[31] Rogers J. H. and Bolling S. F. Current perspective and evolving management of tricuspid regurgitation. 2009.

[32] Joachim Schofer, Klaudija Bijuklic, Claudia Tiburtius, Lorenz Hansen, Adam Groothuis, and Rebecca T. Hahn. First-in-human transcatheter tricuspid valve repair in a patient with severely regurgitant tricuspid valve. *Journal of the American College of Cardiology*, 65(12):1190 – 1195, 2015.

[33] Pravin M. Shah and Aidan A. Raney. Tricuspid valve disease. *Current Problems in Cardiology*, 33(2):47 – 84, 2008. Tricuspid Valve Disease.

[34] Castagna M. and Lentini G. A mock circulation loop for the right heart. Master's thesis, Poltecnico di Milano, 2016.

[35] Michal Jaworek, Marco Piola, Federico Lucherini, Guido Gelpi, Marco Castagna, Giuliana Lentini, Carlo Antona, Gianfranco B Fiore, and Riccardo Vismara. Functional tricuspid regurgitation model in a beating heart platform. *ASAIO journal (American Society for Artificial Internal Organs : 1992)*, January 2017.

[36] Jan-Willem Lankhaar, Nico Westerhof, Theo J. C. Faes, Koen M. J. Marques, J. Tim Marcus, Piet E. Postmus, and Anton Vonk-Noordegraaf. Quantification of right ventricular afterload in patients with and without pulmonary hypertension. *American Journal of Physiology - Heart and Circulatory Physiology*, 291(4):H1731–H1737, 2006.

[37] Jean-Pierre Rabbah, Neelakantan Saikrishnan, and Ajit P. Yoganathan. A novel left heart simulator for the multi-modality characterization of native mitral valve geometry and fluid mechanics. *Annals of biomedical engineering*, 41(2):305–315, September 2012.

[38] A. M. Leopaldi, R. Vismara, M. Lemma, L. Valerio, M. Cervo, A. Mangini, M. Contino, A. Redaelli, C. Antona, and G. B. Fiore. In vitro hemodynamics and valve imaging in passive beating hearts. *Journal of Biomechanics*, 45(7):1133–1139, 2012.

[39] Ashraf M. Anwar, Marcel L. Geleijnse, Folkert J. ten Cate, and Folkert J. Meijboom. Assessment of tricuspid valve annulus size, shape and function using real-time three-dimensional echocardiography. *Interactive CardioVascular and Thoracic Surgery*, 5(6):683, 2006.

[40] Marco Stevanella, Emiliano Votta, Massimo Lemma, Carlo Antona, and Alberto Redaelli. Finite element modelling of the tricuspid valve: A preliminary study. *Medical Engineering & Physics*, 32(10):1213 – 1223, 2010.

[41] Matthew E. Hiro, Jerome Jouan, Matthew R. Pagel, Emmanuel Lansac, Khee Hiang Lim, Hou Sen Lim, and Carlos M. G. Duran. Sonometric study of the normal tricuspid valve annulus in sheep. *J Heart Valve Dis*, 2004.

[42] K. May-Newman and F. C. P. Yin. A constitutive law for mitral valve tissue. *Journal of Biomechanical Engineering*, 120(1):38–47, February 1998.

[43] Francesco Sturla, Alberto Redaelli, Giovanni Puppini, Francesco Onorati, Giuseppe Faggian, and Emiliano Votta. Functional and biomechanical effects of the edge-to-edge repair in the setting of mitral regurgitation: Consolidated knowledge and novel tools to gain insight into its percutaneous implementation. *Cardiovascular Engineering and Technology*, 6(2):117–140, 2015.

[44] Chung-Hao Lee, Pim J. A. Oomen, Jean Pierre Rabbah, Ajit Yoganathan, Robert C. Gorman, Joseph H. Gorman, Rouzbeh Amini, and Michael S. Sacks. *A High-Fidelity and Micro-anatomically Accurate 3D Finite Element Model for Simulations of Functional Mitral Valve*, pages 416–424. Springer Berlin Heidelberg, Berlin, Heidelberg, 2013.

[45] Jorge Hernan Jimenez, Dennis Dam Soerensen, Zhaoming He, Jennifer Ritchie, and Ajit P. Yoganathan. Mitral valve function and chordal force distribution using a flexible annulus model: An in vitro study. *Annals of Biomedical Engineering*, 33(5):557–566, 2005.